

2008

Characterization and recovery of shape memory polymers filled with carbon nanofibers

Daniel Stephen Powers
University of Dayton

Follow this and additional works at: https://ecommons.udayton.edu/graduate_theses

Recommended Citation

Powers, Daniel Stephen, "Characterization and recovery of shape memory polymers filled with carbon nanofibers" (2008). *Graduate Theses and Dissertations*. 4997.
https://ecommons.udayton.edu/graduate_theses/4997

This Dissertation is brought to you for free and open access by the Theses and Dissertations at eCommons. It has been accepted for inclusion in Graduate Theses and Dissertations by an authorized administrator of eCommons. For more information, please contact mschlange1@udayton.edu, ecommons@udayton.edu.

CHARACTERIZATION AND RECOVERY OF SHAPE MEMORY POLYMERS
FILLED WITH CARBON NANOFIBERS

Dissertation

Submitted to

The School of Engineering of the
UNIVERSITY OF DAYTON

in Partial Fulfillment of the Requirement for

The Degree

Doctor of Philosophy in Materials Engineering

by

Daniel Stephen Powers


UNIVERSITY OF DAYTON

Dayton, Ohio


May, 2008

CHARACTERIZATION AND RECOVERY OF SHAPE MEMORY POLYMERS
FILLED WITH CARBON NANOFIBERS

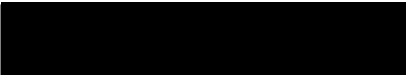
APPROVED BY:




Daniel Eylon, D.Sc.
Committee Chairman
Professor and Director,
Materials Engineering



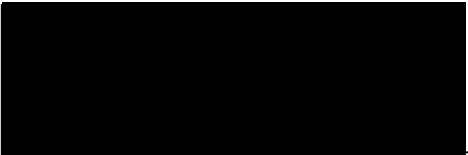
Donald A. Klosterman, Ph.D.
Committee Member
Assistant Professor,
Chemical & Materials Engineering



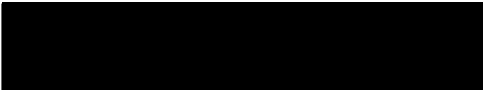
Andrey A. Voevodin, Ph.D.
Committee Member
Professor, Materials Engineering



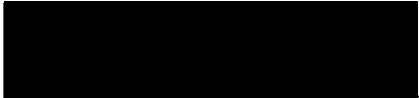
Gerald J. Shaughnessy, M.S.
Committee Member
Associate Professor, Mathematics



Richard A. Vaia, Ph.D.
Committee Member
Technology Advisor, Air Force
Research Laboratory



Malcolm W. Daniels, Ph.D.
Associate Dean
School of Engineering



Joseph E. Saliba, Ph.D., P.E.
Dean, School of Engineering

ABSTRACT

CHARACTERIZATION AND RECOVERY OF SHAPE MEMORY POLYMERS FILLED WITH CARBON NANOFIBERS

Powers, Daniel Stephen
University of Dayton

Advisor: Dr. Daniel Eylon

The microstructure and shape memory properties of polymers utilizing two different shape memory processes reinforced with vapor grown carbon nanofibers (CNFs) were investigated by thermal and thermomechanical techniques. The first shape memory polymer (SMP) was a thermoplastic polyurethane elastomer (Irogran) that used strain-induced crystallization for locking in the deformation. Shape recovery occurred though the melting temperature of the crystallites and demonstrated relatively good shape memory properties. Both shape fixity (ability to lock in the deformation) and recovery time (how fast the material recovered back to its original shape) improved with carbon nanofiber loading; however, the percent recovery (ability to return back to its original shape) decreased with CNF loading.

Initial studies verified the role of strain-induced crystallization. Solid-state proton nuclear magnetic resonance (NMR) was used to investigate the impact of CNFs on the structure and dynamics of the crystallites in this thermoplastic polyurethane elastomer (TPE). The introduction of CNFs led to a shifting and broadening of the spectra, where

the magnitude of the induced shifts and line broadening increased with CNF concentration. The spin-lattice and spin-spin relaxation times were not significantly changed with the introduction of CNFs. This demonstrated that the line broadening was inhomogeneous and a consequence of the magnetic susceptibility of the CNFs and not a reduction in segment mobility due to the proximity of the CNF surface. Spin diffusion experiments provided additional insight into the strain induced structure of the TPE/CNF composites.

The second SMP was a thermoset epoxy (TEMBO DP5.1) reinforced with CNFs. This SMP used vitrification through the glass transition temperature for locking in the deformation and demonstrated excellent shape memory properties. The morphology of the CNFs throughout the epoxy polymer matrix, along with the recovery times of the nanocomposites was investigated. The incorporation of CNFs throughout the polymer matrix did not show an improvement in the shape fixity, shape recovery, or recovery times. Since the CNFs did not interact with the polymer matrix, there was no enhancement of the shape memory properties.

ACKNOWLEDGEMENTS

Many special thanks are in order to Dr. Daniel Eylon, my academic advisor, for providing the time and guidance for the work contained herein, and for directing this dissertation and bringing it to its conclusion with patience and expertise. I would also like to thank my research advisor, Dr. Richard A. Vaia, for giving me the opportunity to join his research group and for his constant support and guidance throughout my research program. His expertise and knowledge in polymer physical science and nanotechnology will prove to be invaluable throughout the rest of my scientific career. To my committee members, Dr. Donald A. Klosterman, Dr. Andrey A. Voevodin, and Dr. Gerald J. Shaughnessy for providing guidance and instruction. A special acknowledgment is in order for the University of Dayton, the Air Force Research Laboratory – Materials & Manufacturing Directorate, the Air Force Office of Scientific Research, and Composite Technology Development Inc. for support of my research.

I would also like to express my thanks and appreciation to everyone that has helped with this research effort. Especially Dr. Hilmar Koerner, who offered his expertise in material characterization and painstakingly guided me in the right direction; Dr. Peter A. Mirau who gave his expert advice on nuclear magnetic characterization of polymers; Dr. Barney Taylor who provided not only advice as a physicist, but also helped me experience the true life of a graduate student; Ms. Marlene D. Houtz who taught me

how to use and understand all of the thermal and thermomechanical characterization equipment; Mr. Max D. Alexander who offered guidance in sample preparation and material characterization techniques; and Ms. Heather J. Dowty who provided encouragement and support as a friend.

Special thanks to my coworkers Dr. Lawrence F. Drummy, Dr. David M. Phillips, Dr. Daniel T. Welna and Dr. Tai-Sik Kang whose friendship and in-depth scientific discussions has helped me throughout this research effort. I cherish our friendships and look forward to sharing many more experiences during our lifetimes.

On a personal note, I want to thank my parents, Joseph and Margie Powers, for their encouragement, love, and support. To my father-in-law, Vincent R. Jacobucci, for his positive words of encouragement and support. And to the rest of my family for their support and believing that I could complete this endeavor. I hope to make them all proud of my accomplishments.

And finally I wish to thank my loving wife, Margaret M. Powers, for her unending love, encouragement, and support are directly responsible for my incessant desire to succeed and my refusal to give up on my dreams. I will never be able to repay her for all that she has done for me and my career.

PREFACE

A variety of studies are currently being performed on shape memory polymers filled with nanoparticles to provide a greater understanding of the recovery properties of these nanocomposites. The need for reliable, affordable, and enhanced nanocomposite systems has placed renewed demands for new and improved high performance, low cost, lightweight, multi-functional material systems. Specifically, there is a need for large improvements in mechanical properties such as strength and stiffness, along with thermal and electrical transport management in the next generation of lightweight hybrid material systems. Significant enhancements in performance and functionality may be achieved by reinforcing polymers with nanoscale fillers (i.e., spheres, rods, carbon nanotubes, carbon nanofibers, etc.) to form polymer nanocomposites. These polymer nanocomposites offer the possibility to perform multifunctional tasks, where the reinforcement particles can impart properties such as enhanced mechanical strength and customized thermal and electrical transport characteristics. In this research effort we will demonstrate how the addition of carbon nanofibers to a shape memory polymer influenced the strain-induced crystallization recovery process, new tools for characterizing this recovery process by understanding the carbon nanofiber interface and the crystallites that form during strain-induced crystallization, and finally understanding how these carbon nanofibers influence the recovery in a shape memory polymer that uses vitrification through the glass transition temperature to lock in deformation.

TABLE OF CONTENTS

ABSTRACT	iii
ACKNOWLEDGEMENTS	v
PREFACE	vii
LIST OF FIGURES	xi
LIST OF TABLES	xiv
LIST OF ABBREVIATIONS	xv
CHAPTER	
I. INTRODUCTION	1
II. SHAPE MEMORY MATERIALS	9
Shape Memory Alloys (SMAs)	10
History	10
Shape Memory Effect and Superelasticity	11
Mechanism	12
Transformation Temperatures	15
Different Alloy Types	16
Copper-based Alloys	17
Nickel-based Alloys	18
Applications	19
Shape Memory Ceramics (SMCs)	21
History	22
Piezoelectricity	24
Mechanism	25
Dipole Effect and Polarization	27
Domain Switching	29
Applications	30

Shape Memory Polymers (SMPs)	32
History	34
Mechanism	35
Chemical and Physical Crosslinks	38
External Stimulus	39
Thermally-responsive	39
Chemically-responsive	40
Photo-responsive	40
Applications	41
III. NANOPARTICLE FILLERS IN SHAPE MEMORY POLYMERS	44
IV. IMPACT OF CARBON NANOFIBERS ON THE LOCKING MECHANISM FOR A SHAPE MEMORY THERMOPLASTIC POLYURETHANE ELASTOMER	49
Experimental	52
Materials	52
Processing	53
Morphology	54
Thermal Characterization	55
Thermomechanical Characterization	55
Thermal Histories	56
Setting Deformation and Crystallite Formation	56
Method 1 – Temperature Quench Crystallization	56
Method 2 – Strain-induced Crystallization	57
Results and Discussion	61
Conclusions	74
V. NMR CHARACTERIZATION OF LOW HARD SEGMENT THERMOPLASTIC POLYURETHANE/CARBON NANOFIBER COMPOSITES	77
Experimental	79
Materials	79
Polymer Nanocomposite Fabrication	80
Deformation and Setting	81
Solid State Proton NMR Experiments	81
Results and Discussion	82
Conclusions	92
VI. IMPACT OF CARBON NANOFIBERS ON THE LOCKING MECHANISM FOR A SHAPE MEMORY THERMOSET EPOXY	95
Experimental	98
Materials and Specimen Preparation	98

	Morphology	100
	Thermal Characterization	100
	Thermomechanical Characterization	101
	Shape Recovery and Recovery Time Characterization	101
	Results and Discussion	105
	Conclusions	113
VII.	CONCLUSIONS	116
VIII.	FUTURE WORK	122
IX.	REFERENCES	129

LIST OF FIGURES AND ILLUSTRATIONS

Figure 2.1: Temperature dependent phase transformations for shape memory effect	14
Figure 2.2: Phase transformation temperatures	16
Figure 2.3: Phase transformations for (a) paraelectric, (b) antiferroelectric, and (c) ferroelectric shape memory ceramic materials	26
Figure 2.4: Modified illustration of Barium titanate (a) with cubic crystal and (b) tetragonal crystal structure	28
Figure 2.5: Random orientation with (a) adjacent domains polarized in opposite directions and (b) domains aligned with an electric field showing a net polar effect	29
Figure 2.6: Shape memory effect in polymers (a) original or parent phase, (b) deformation to temporary shape, (c) force removed to reveal new strain set, (d) temperature increased to recover original shape	36
Figure 2.7: Polymer with amorphous and crystalline regions	37
Figure 4.1: 3D plot of stress vs. strain vs. temperature for shape recovery using high temperature quench crystallization method	57
Figure 4.2: 3D plot of stress vs. strain vs. temperature for shape recovery using room temperature strain-induced crystallization method	58
Figure 4.3: Typical DMA scan of a shape recovery experiment	59
Figure 4.4: SEM image of a 2.90 vol% CNF in Irogran	61
Figure 4.5: Effect of CNF loading on glass transition temperature (T_g)	63

Figure 4.6: DSC enthalpy data showing the effect of crystallite formation for (a) as-cast (unstrained) samples (Δ), (b) thermally annealed samples (\circ), and (c) the formation of crystallites through a temperature quench (\square)	64
Figure 4.7: Wide angle x-ray scattering (WAXS) of neat Irogran (dashed line) and Irogran filled with 5.92 vol% carbon nanofibers (solid line)	65
Figure 4.8: Normalized storage modulus (E/E_0) vs. volume fraction (%) of carbon nanofibers	66
Figure 4.10: Effect of CNF loading on % shape fixity for a high temperature (HT) quench and room temperature (RT) strain-induced (with and without initial crystallites)	69
Figure 4.11: Effect of CNF loading on % shape recovery for a high temperature (HT) quench and room temperature (RT) strain-induced (with and without initial crystallites)	70
Figure 4.12: Recovery time calculated from set strain (ϵ_{set}) to the recovered strain (ϵ_{rec}) using NLSF analysis software	71
Figure 4.13: Effect of CNF loading on recovery time for a high temperature (HT) quench and room temperature (RT) strain-induced (with and without initial crystallites)	72
Figure 4.14: Schematic of nominal stress versus nominal strain curve for a thermoplastic elastomer	74
Figure 5.1: 500 MHz proton NMR spectra of (a) Irogran dissolved in THF- d_8 and (b) the as-cast film (See Scheme 1 for proton assignments)	83
Figure 5.2: NMR line broadening spectra of the as-cast (a) neat Irogran, with (b) 1 wt% CNF, (c) 10 wt% CNF, and (d) 15 wt% CNF	84
Figure 5.3: Comparison of the stretched and as-cast films (a) without and (b) with 10 wt% CNF	85
Figure 5.4: Magnetization exchange curves for as-cast (filled symbols) and stretched to $\lambda=1.6$ (open symbols) samples of (a) TPE films and (b) 10% TPE/CNF composites	89
Figure 5.5: A spin diffusion plot for the as-cast TPE film sample	90
Figure 6.1: Amino hydrogen atom added across an epoxy ring	97

Figure 6.2: 3D plot of stress vs. strain vs. temperature for a shape recovery experiment via vitrification through T_g	102
Figure 6.3: DMA plot of a shape recovery experiment for a neat epoxy	103
Figure 6.4: SEM scan of a 1 vol% Epoxy/CNF showing good dispersion of CNFs but poor adhesion of CNFs to polymer matrix	105
Figure 6.5: Closer magnification shows a gap around the CNF	106
Figure 6.6: Effects of CNF loading on glass transition temperature (T_g)	107
Figure 6.7: Effects of temperature on storage modulus (E')	108
Figure 6.8: Effects of CNF loading on normalized storage modulus (E/E_0)	109
Figure 6.9: Effect of CNF loading on shape fixity	110
Figure 6.10: Effect of CNF loading on percent shape recovery	111
Figure 6.11: Non-linear least square fit used to calculate shape recovery time	112
Figure 6.12: Effect of CNF loading on shape recovery time	113
 Scheme 5.1: The structure and proton assignments for Irogran	 80

LIST OF TABLES

Table 5.1: Effect of CNF on the proton chemical shift (δ_H) and linewidths ($\Delta\nu_{1/2}$) for Irogran composites	84
Table 5.2: Spin-lattice relaxation times (T_1), spin-spin relaxation times (T_2), chemical shifts (δ_H), and linewidths (observed and calculated) for stretched and as-cast Irogran and the 10 wt% CNF composite	87
Table 5.3: Spin diffusion times and domain sizes for Irogran films and the 10 wt% CNF composites	92

LIST OF ABBREVIATIONS

A_f	Austenite finish temperature
A_s	Austenite start temperature
ASI	Applied Sciences Incorporated
AuCd	Gold-cadmium alloys
Ba^{2+}	Barium cations
$BaTiO_3$	Barium titanate
CB	Carbon black
$CDCl_3$	Deuterated chloroform
cm^3	Cubic centimeter
CNFs	Carbon nanofibers
CNTs	Carbon nanotubes
CuAlNi	Copper-aluminum-nickel alloys
CuZn	Copper-zinc brass alloys
CuZnAl	Copper-zinc-aluminum alloys
CpPOSS	Cyclopentyl polyhedral oligomeric silsesquioxane
CyPOSS	Cyclohexyl polyhedral oligomeric silsesquioxane
CTD	Composite Technology Development
d	Domain size
d_{lp}	Long period of domain or distance between domains

D_A	Spin diffusion coefficient for mobile phase
D_B	Spin diffusion coefficient for immobile phase
DMA	Dynamic mechanical analyzer
DSC	Differential scanning calorimeter
E	Young's modulus or modulus of elasticity
E'	Storage modulus
E''	Loss modulus
E_0	Modulus of neat polymer
E/E_0	Normalized storage modulus
f_A	Volume fraction mobile phase
f_B	Volume fraction immobile phase
F	Force
FWHM	Full-width at half-maximum
g	Grams
G_f	Effective aspect ratio
ΔH_C	Change in enthalpy datum of crystallization
HT	High temperature
Hz	Hertz
InTl	Indium thallium
kHz	Kilohertz
l	Length
L	Length scale of spin diffusion
M_0	Initial intensities

ΔM	Change in intensity
M_f	Martensite start temperature
M_s	Martensite finish temperature
MHz	Megahertz
m_{ch}	Char mass percentage
min	Minutes
mm	Millimeter
ms	Milliseconds
MDSC	Modulated differential scanning calorimeter
MPa	Megapascals
MWNTs	Multi-walled carbon nanotubes
N	Newtons
NiTi	Nickel-titanium alloys
nm	Nanometer
NLSF	Non-linear least square fit
NMR	Nuclear magnetic resonance
O^{2-}	Oxygen anions
PCL	Polycaprolactone
PN	Polynorbornene
POSS	Polyhedral oligomeric silsesquioxane
ppm	Parts per million
PSLD	Pyrolytically stripped low density
PZT	Lead zirconate titanate

rpm	Revolutions per minute
RT	Room temperature
S_d	Orientation parameter
s	Seconds
SEM	Scanning electron microscope
SiC	Silicon carbide
SMA _s	Shape memory alloys
SMC _s	Shape memory ceramics
SMP _s	Shape memory polymers
SWNT	Single-wall carbon nanotubes
t	Thickness
t_1	Relaxation time
T_1	Spin-lattice relaxation time
T_2	Spin-spin relaxation time
T	Temperature
T_C	Curie temperature
T_d	Deformation temperature
T_{dec}	Decomposition temperature
T_g	Glass transition temperature
T_{hsm}	Hard segment melting temperature
T_m	Melting temperature
T_s	Setting temperature
T_{ssm}	Soft segment melting temperature

T_{trans}	Transition temperature
TGA	Thermal gravimetric analyzer
THF	Tetrahydrofuran
Ti^{4+}	Titanium cation
TMA	Thermal mechanical analyzer
TPE	Thermoplastic polyurethane elastomer
UV	Ultraviolet
VGCFs	Vapor grown carbon nanofibers
vol%	Volume percent
w	Width
WAXS	Wide angle x-ray spectrophotometry
wt%	Weight percent
XRD	X-ray diffraction
ZrO_2	Zirconia
δ_{H}	Chemical shift
ε	Strain
ε_{max}	Maximum strain
ε_{set}	Set strain
$\varepsilon_{\text{recov}}$	Recovered strain
λ	Elongation
μs	Microseconds
ρ_{A}	Proton density of mobile fraction
ρ_{B}	Proton density of immobile fraction

τ	Recovery time
τ_0	Delay time
τ_m	Spin diffusion period
$\Delta\nu_{1/2}$	Change in line width
Φ	Volume fraction

CHAPTER I

INTRODUCTION

Within the last decade, shape memory polymers (SMPs) have attracted significant attention in the scientific and academic communities due to their ability to “remember” different shapes under varying conditions. These new SMPs can provide great potential for sensors, actuators, smart devices, and medical applications [1-7]. Advantages of these new SMPs include high elastic deformation (strains from 100-1000%), light weight, low cost, biocompatibility, and biodegradability. In addition, SMPs can be tailored to meet a specific application or need. By adjusting the chemical composition during processing the glass transition temperature can be modified to an appropriate temperature range or more than one type of external stimulus can be used to trigger the recovery process [8-14].

Unfortunately, those same properties which are listed as advantages can also be listed as disadvantages (low storage modulus, low density, poor thermal and electrical conductivity, etc.). To help resolve the issue of low storage modulus and strength, traditional fillers (i.e., talc, sawdust, mica, etc.) were added as reinforcements to the polymer matrix [9]. This allowed tailoring of the materials stiffness and helped reduced the overall processing costs. The disadvantage of this approach was that composite samples required 30-50 wt% of these fillers to help improve the strength. Within the last

few decades, there has been a growing interest in using nanoparticles as fillers. With relatively high aspect ratios (length to width ratio), the same results could be obtained with only 3-5 wt% loadings [9, 15]. This recent interest in nanocomposite technology has led to a broad availability of different nanosized particles (i.e., bucky balls, silicon carbide, carbon black, carbon nanotubes, carbon nanofibers, etc.), some with relatively large aspect ratios (>100). These new nano materials have led to a resurgence of applied and fundamental investigations of filled polymer systems. The nanoscopic dimensions and high aspect ratios inherent in these polymer nanocomposites have provided the properties of traditional filled systems, but at lower loadings and enhanced processing capabilities.

Recent advancements in manufacturing technology have resulted in large scale production of carbon nanoparticles (i.e., carbon black, carbon nanotubes, carbon nanofibers, etc.) [16-17]. When dispersed as fillers in polymers, these nanocomposite materials can provide not only improvements in the storage modulus, but additional properties such as thermal conductivity, electrical conductivity, change in dielectric storage capacity, radiation shielding, sensing, actuation, enhanced mechanical properties, scratch-resistance, and improved fracture toughness. These properties are regulated by the distribution and dispersion of the nanoparticles. By coupling the excellent insulating properties of polymers with conductive nanomaterials, an array of engineering materials can be developed. An understanding of the processing-structure-property relationship for these nanoparticle reinforced polymers is essential for developing new nanocomposite materials.

The major focus of this research effort is to understand how the addition of nanoparticles will impact the locking mechanism or set strain for two different SMP systems. Each of these polymer systems use a different mechanism for locking in the deformation. The first SMP system is a thermoplastic polyurethane elastomer (TPE) called Irogran that uses strain-induced crystallization to help lock in the deformation. The second SMP system is a thermoset epoxy called TEMBO DP5.1 that uses vitrification through the glass transition temperature to help lock in the strain. Both of these SMP systems have demonstrated very good shape memory properties such as the ability to lock in deformation and return back to its original shape. If the addition of nanoparticles does play a key role in the locking mechanism, then they should be added to help improve the performance of the material. However, if they do not improve the mechanical performance (i.e., storage modulus) or play a major role in the locking mechanism and do not show improvement, then they should be considered for improvement of secondary properties such as barrier or electrical conductivity. The carbon nanoparticles used in this study were carbon nanofibers because they were readily available at a low cost and provided good thermal and electrical conductivity. Carbon nanofibers (CNFs) are simply graphene sheets of carbon atoms rolled into nanometer size multi-walled fibers [15-17]. They are ideal reinforcing fillers in SMP nanocomposites because of their high aspect ratio, nanosize diameter, very low density, high mechanical strength, and high electrical and thermal conductivity.

Even though there has been extensive research conducted on various types of SMPs and the incorporation of nanoparticles in different polymer systems, there has been

very little information published on incorporating nanoparticles into SMP systems. As a result, we have focused our attention on three main objectives. The first is to determine if the addition of CNFs to a SMP that uses strain-induced crystallization will actually improve, hinder or show no change to the shape memory properties and recovery process. Second, can we use alternative methods such as nuclear magnetic resonance (NMR) to help characterize the interaction between the CNFs and the formation of crystallites that help lock in this deformation? And the third objective is to determine the impact that CNFs will have on a SMP that uses vitrification through a glass transition temperature to help lock in the deformation. Primarily we want to know if the addition of nanoparticle fillers will have the similar or different results compared to a SMP that uses strain-induced crystallization.

For the first objective, we will incorporate CNFs into a SMP that uses strain-induced crystallization to lock in the deformation. The formation of crystallites is critical to forming physical crosslinks that can temporarily lock in the deformation. There were several questions that would help us understand how these CNFs impact the set strain: (a) what was the impact of initial crystallites on the shape memory process, (b) did forming crystallites by different techniques influence the setting process, (c) what was the impact of both of these processes on the shape memory properties and recovery rate, and (d) what was the effect at low strain? The results from this study will help us better understand the interaction between the CNFs and the polymer, leading to better crystallite formation and strain set.

Process history is an important issue to understanding the formation of initial crystallites during the fabrication of these SMP nanocomposite samples. We wanted to know if these initial crystallites had an impact on the recovery process or not. Secondly, there were two different ways of forming crystallites during shape memory experiments to help lock in the deformation: strain-induced crystallization and crystallization through a temperature quench. We wanted to know if there was a difference between these two methods. This would lead to further questions about the impact of these different mechanisms for forming crystallites on the ability to lock in the deformation, shape recovery and recovery times. Some of the literature reported that the addition of nanoparticles decreased the formation of crystallites resulting in slower recovery times [8-9]. If the addition of CNFs increased the crystallite content, we might be able to show an improvement in how fast these SMP nanocomposites recover. The final question involved experiments performed at lower strains. We were interested in determining if there was a substantial difference in the shape memory properties and formation of crystallites at the lower strain set (60%), which is at the onset of strain-induced crystallization for the SMP.

For the second objective we wanted to understand how the CNFs affected the process of locking in the deformation through strain-induced crystallization. There are numerous ways of characterizing the interaction between the CNF and polymer matrix and we will use nuclear magnetic resonance. NMR is a powerful tool to study the structure and dynamics of complex and heterogeneous systems because the spectroscopy properties (chemical shifts, relaxation times and line widths) all depend on the local

structure and dynamics [18]. The challenge in understanding nanocomposites is to isolate the signal from the interfaces so that the structure and dynamics of interfacial materials can be studied. If we can do this we should be able to show what happened at the surface of the CNF versus what happened away in the bulk of the material.

This will be the first time that NMR has been used to understand heterogeneity in a SMP system filled with CNFs. From this data we hope to show how CNFs impact the formation of crystallites and how they influence changes in the chemical shifts and line broadening. By studying the spin-lattice (T_1) and spin-spin (T_2) relaxation times, we should be able to determine if inhomogeneous line broadening are due to a differences in magnetic susceptibilities between the CNFs and the polymer, dipolar couplings or paramagnetic interactions. To overcome poor signal-to-noise and lack of carbon signals (cross polarization and magic-angle sample spinning) arising from the CNFs, proton signals from the mobile fraction of the thermoplastic elastomer will be used as an indirect measure of the interfacial structure. Using this approach, we hope to determine the proximity of the CNFs to the mobile fraction, the effect of CNFs on the chain dynamics, and the size of rigid domains (crystallites or hard segment domains) as a function of CNF concentration and external strain.

For the last objective, we will incorporate CNFs into a SMP that uses vitrification through the glass transition temperature to help lock in the deformation. If the addition of nanoparticle fillers do not impact the mechanical properties (i.e., T_g , E , etc.), then we would not expect to see improvements in the strength and stiffness of the material. This

would also impact the shape recovery properties such as ability to lock in the deformation and return back to its original shape. This last objective focused on a shape memory epoxy that uses vitrification through the glass transition temperature to help lock in the deformation. By incorporating CNFs into this new SMP system we were able to show that CNFs had very little impact on the locking mechanism, shape fixity, shape recovery or recovery time.

Overall, this research effort should demonstrate how the addition of CNFs to a SMP influenced the strain-induced crystallization recovery process, new tools for characterizing this recovery process by understanding the CNF interface and the crystallites that form during strain-induced crystallization, and finally understanding how these CNFs influence the recovery in a SMP that uses vitrification through the glass transition temperature to lock in deformation. What we hope to accomplish with this research is to further our understanding of how to intelligently add nanoparticles to SMPs to improve the performance in a systematic manner.

In the next chapter we will provide some background about shape memory properties, different types of shape memory materials that are available and the mechanisms that are used to recover the deformation. Chapter 3 will summarize what has been accomplished in nanocomposite SMPs. Chapter 4 will talk about a TPE that uses strain-induced crystallization to help lock in the deformation and how the addition of CNFs helped improve that process. This has helped extend our understanding of prior work in this area. Chapter 5 will talk about how we can use NMR to better understand

how the CNFs play an important role in the locking mechanism by helping in the formation of crystallites. Chapter 6 will extrapolate the idea that the key to improving shape memory performance is the nano coupling with the locking mechanism. Here we can test the hypothesis of what we would expect to happen in a SMP system that uses vitrification though the glass transition temperature (T_g) to help set the strain. Chapter 7 will provide conclusions that were made about the impact of nanoparticle fillers on different SMPs and compare the differences for locking in the deformation. And finally the last chapter will address additional questions and how one may accomplish this in future work.

Even though nanocomposite SMPs are state of the art technology, there are some misconceptions about how and when to incorporate nanoparticles into these systems. At the start of this research effort, there was wide-spread hype that nanoparticles could resolve a lot of our problems. We now understand what these experiments have shown is that CNFs can improve the modulus, and modulus relates to the mechanical energy stored for a given strain. However, what we have discovered is that by really focusing on understanding how the nanoparticles couple to the strain set of the polymer, we can now understand why the different types of polymer systems behave differently when nanoparticles are added.

CHAPTER II

SHAPE MEMORY MATERIALS

The term “shape memory” refers to those materials that have the unique ability to temporarily change their shape and then return back to their original shape [1]. An external stimulus (i.e., temperature, pressure, electricity, etc.) is used to elicit a response in these materials. The response can be a change in the atomic configuration or a change in the dipolar interactions or a change in rigidity of the material. Once this response has occurred, the material can now be deformed into a new temporary shape. When the force used to deform the material is removed, it will maintain this new temporary shape. This new temporary shape can be maintained almost indefinitely as long as the external stimulus is maintained. By reversing or applying a different external stimulus, the original shape can now be recovered. These changes result in a complete or nearly complete relaxed state that resembles the original or stress-free state. It is this ability of “remembering” two shapes at different conditions that makes shape memory materials attractive to scientists and engineers. This chapter will summarize details of three major classes of shape memory materials: alloys, ceramics and polymers. Background information on the history, mechanisms, transformation temperatures, and different applications will be discussed for all three materials.

Shape Memory Alloys

The most recognized and widely used shape memory materials are shape memory alloys (SMAs) [19]. These are a group of metallic alloys that have the ability to be deformed into a new temporary shape and then return to their original shape when subjected to a temperature change. This ability to change shape is due to a transformation in the crystalline structure at a specific temperature. The temperature at which this change occurs is commonly referred to as a reverse transformation temperature [20-21]. Above this temperature the alloy will have one crystalline structure and below it will have a completely different crystalline structure. When the SMA is in this lower temperature structure, it can be easily deformed or changed. If the temperature is increased back above the transformation temperature, the material will return back to its original shape and crystalline structure. This ability of “remembering” its original shape is how the term shape memory came about.

History

The first reported shape memory transformation was observed by Chang and Read in 1932 [1]. Using a gold-cadmium (AuCd) alloy, they were able to show a reversible transformation by utilizing metallographic techniques and resistivity changes. Then in 1938, Greninger & Mooradian [22] observed a similar transformation in a copper-zinc (CuZn) brass alloy. By increasing and decreasing the temperature, they noticed the formation and disappearance of a martensitic crystalline phase. This led to further testing and in 1951, Chang and Read [23] reported on a gold-cadmium (AuCd) alloy bar that was bent. The transformation temperature was used to return the bent bar

back to its original shape. Although these events were significant, it was not until the early 1960's that a major discovery was made at the U.S. Naval Ordnance Laboratory. Buehler and coworkers [24] were working on a nickel-titanium (NiTi) alloy called Nitinol. By varying the temperature through a specific region, they were able to demonstrate the shape memory effect with substantial changes in shape. The results of this discovery lead to new research into manufacturing and commercial applications due to the combination of a desirable transition temperature, superelasticity, and biocompatibility.

Shape Memory Effect and Superelasticity

SMA's have demonstrated the unique properties of shape memory effect and superelasticity. The shape memory effect takes place at a lower temperature where the material changes into a new crystalline structure. If a load or stress is applied to this new structure it can be easily deformed into a new shape [25-26]. The material can maintain this new deformed shape almost indefinitely, even when the load is removed. To change back to its original shape, the temperature of the material is raised back above the transformation temperature. Once above the transformation temperature, the material will revert back to its original crystalline structure and the deformation is lost.

The other unique property is superelasticity or pseudoelasticity [27] and this refers to the ability of a material to change its shape with loading and unloading. Unlike the shape memory effect which is both thermally and mechanically activated, superelasticity is only mechanically activated. The effect is similar to stretching a rubber

band and releasing it. Once the stress is released, the rubber band snaps back to its original shape. For SMAs the process takes place when the material is in its higher temperature parent phase. If a load is applied while in the parent phase, the alloy will temporarily transform into a different crystalline structure even without a temperature change. However, when the stress is removed the material reverts back to its original parent phase and recovers its original shape. This effect gives the appearance of extreme elasticity and is called superelasticity or pseudoelasticity.

Mechanism

One of the key features of a SMA is that it can switch between two different crystalline structures at a specific transformation temperature. Above this temperature the alloy exists as an austenitic phase, which has a simple cubic structure with a long range order. Below this temperature the alloy transforms into a martensitic phase, which has a more complex rhombic or monoclinic structure. This unique crystalline structure was first discovered by Adolph Martens in 1890 [28-29]. Using an optical microscope, he observed an unusual pattern in the microstructure of certain metallic alloys. The pattern consisted of stripped or banded regions of a microcrystalline structure that later became known as martensite.

Unlike austenite which has only one orientation, martensite can have several different orientations called variants. The reason for these different variants is due to the fact that the martensitic phase has a lower symmetry than the parent austenitic phase. When viewed under a microscope these variants appear as alternately stacked platelets

that have a herringbone pattern. The platelets can deform by a twinning mechanism [30] that allows the structure to have the same volume as the austenitic phase.

While most metals deform by slip or dislocation, SMAs respond to stress by simply changing the orientation of its crystal structure through the movement of twin boundaries. Slip deformation is a permanent process because atomic bonds are broken, whereas twinning is a reversible process because bonds are not broken. This twinning process plays a key role in the shape memory effect. A twin boundary is simply a mirror image of atoms above and below the plane that are lower in energy and are mobile. When stress is applied to the lower energy martensitic phase, the region between the platelets can shift and the material can now be easily deformed. At this point a detwinning process takes place which forces the twins into a single aligned variant [31]. Those variants aligned with the deformation strain will begin to increase in size. When the stress is removed, the SMA will maintain this new “temporary” shape almost indefinitely. If the temperature is heated back above the transformation temperature, the material will return back to its original shape. Figure 2.1 is a modified two-dimensional illustration of this cyclic shape memory effect showing the austenitic, martensitic, and the deformed martensitic phases.

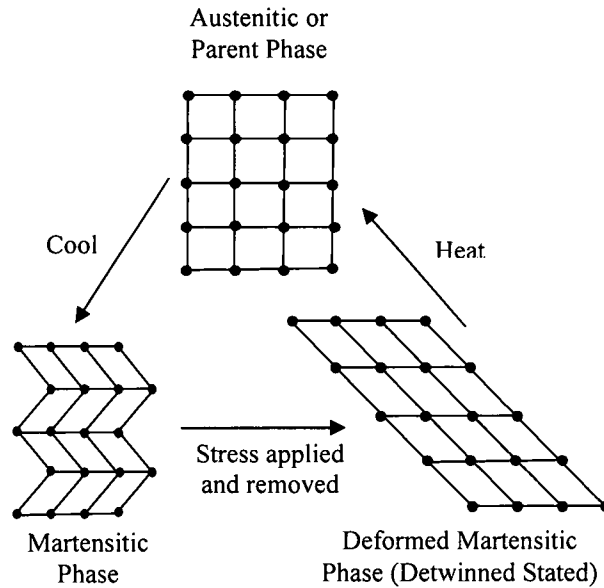


Figure 2.1: Temperature dependent phase transformations for shape memory effect [1, 32]

Most phase changes are usually characterized as going from solid to liquid or liquid to gas, but for SMAs the phase change is from solid to solid. The movement of atoms can be characterized as either diffusional or displacive types of transformations [32]. For the diffusional transformation, a new phase can only be formed by moving atoms over relatively long distances. In contrast, displacive transformations do not require long range movement of atoms. Instead, the atoms can shift or rearrange together into a new crystalline structure that is more stable. This same molecular rearrangement occurs in SMAs resulting in a solid state phase change. Because the molecules remain closely packed during the transformation, the substance remains a solid. Since this phase change does not require atomic diffusion, there is very little change in volume during the transformation from austenite to martensite. However, during the detwinning process

there can be as much as an 8-10% change in size [2, 4, 32] and this is quite substantial for metallic alloys.

Transformation Temperatures

For SMAs, the phase transformation from austenite to martensitic is the key to the shape memory effect. During this phase change there are four characteristic temperatures used to describe the transformation process [1, 21]. Above the transformation temperature the parent phase exists as austenite. As the temperature is rapidly cooled, the austenitic phase begins to change into the martensitic phase. The temperature at which this transformation starts is called the martensite start temperature (M_s). As the temperature cools down further, the alloy changes completely to martensite and this is referred to as the martensite finish temperature (M_f). To reverse this transformation process, the martensite is heated up and it begins to change into austenite. The temperature at which this transformation starts is called the austenite start temperature (A_s). With further heating the alloy changes completely to austenite and this is referred to as the austenite finish temperature (A_f). Figure 2.2 is a modified illustration showing all four transformation temperatures and the relative percentages of each crystallite present.

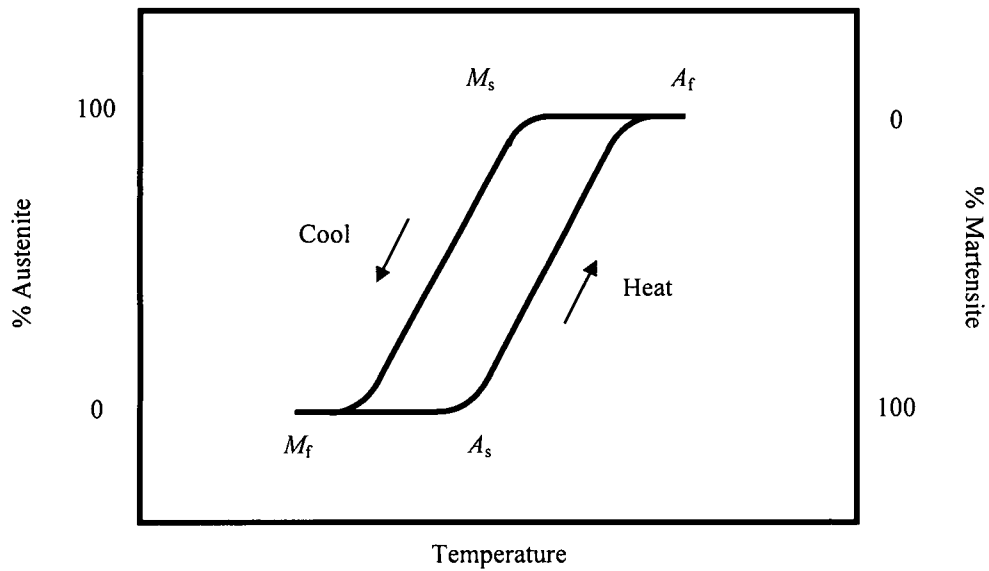


Figure 2.2: Phase transformation temperatures [33]

From this illustration we can see that the temperature range for the austenite to martensite transformation is somewhat higher than that for the martensite to austenite transformation upon cooling. The difference between these two temperature ranges is commonly referred to as hysteresis [33-34]. Another way of defining this hysteresis effect is the difference between the temperatures when the material is 50% transformed to austenite upon heating and 50% transformed to martensite upon cooling. These transformation temperatures can be influenced by heat treatment, material composition, and amount of cold work. By making small changes in either of these processes, the transition temperature can be adjusted up or down to meet the desired application.

Different Alloy Types

As stated earlier, the shape memory effect was first observed in a gold-cadmium (AuCd) alloy. Since then it has been observed in numerous other alloy systems such as

InTi [35-36], CuZn [37], CuAlNi [38]. The most effective and widely used commercial alloys are the copper-based (i.e., CuZnAl and CuAlNi) and nickel-based (NiTi) alloys [32, 39-40]. Even though the copper-based alloys have lower processing and manufacturing costs than the nickel-based alloys, their shape memory performance is not as advanced as the nickel-based alloys. A brief description of these most prominently used SMAs is listed below.

Copper-based Alloys. The first SMA to be commercially developed was a Copper-Zinc-Aluminum (CuZnAl) alloy because of its low cost and easy processing. This intermetallic alloy typically contained 15-30 wt% zinc and 3-7 wt% aluminum [32, 41]. Simply by changing the processing techniques and alloy composition, the transformation temperature could be modified or adjusted to a range of -100°C to 100°C. Two major problems in controlling this alloy composition were oxidation of the zinc and segregation of the aluminum. A low-frequency induction furnace was used to create a large mixing effect to help control this problem. Compared to ceramics, this copper-based alloy had modest shape memory properties with a maximum recoverable strain of about 5%. A major disadvantage was the fact that the martensitic phase could be effected by long term aging. So over a period of time the transformation temperature would slowly start to increase. In addition, when exposed to temperatures above 100°C the alloy structure would start to decompose. This system is rarely used today because the disadvantages outweigh the cost and processing advantage.

The next copper-based alloy was Copper-Aluminum-Nickel (CuAlNi) and it typically contained 11-14 wt% aluminum and 3-5 wt% nickel [32, 41]. Just like the first copper-based alloy, the transformation temperature could also be adjusted from 80°C to 200°C just by changing the alloy composition. Originally it was just composed of copper and aluminum, but the transformation temperature was too high for commercial use. So nickel was added to help lower the transformation temperature. Some major advantages of this particular SMA included a wide range of favorable transformation temperatures, stability at high temperature (especially above 100°C), small hysteresis, and low cost. As a result, this particular alloy has undergone extensive development and is preferred over other copper-based systems. A major disadvantage is that processing costs are a lot higher because the alloy can only be hot worked. In addition, the final heat treatment has to be closely monitored to produce an alloy with the desired transformation temperature. Both of these processing challenges have made the alloy more expensive than the CuZnAl system, but it is still far less expensive than the nickel-based systems.

Nickel-based Alloys. For the nickel-based alloys, the Nickel-Titanium (NiTi) alloys have made huge advancements within the last few years. This alloy is composed of nearly equal amounts of nickel and titanium [42]. Just like the copper-based systems, the transformation temperature is very sensitive to chemical changes and composition. Very small changes in the nickel content can cause large changes in the transformation temperature. This nickel-based alloy also has the advantage of showing a large transformation temperature hysteresis of about 50°C [1, 32, 41]. Despite these advantages, it has the highest manufacturing costs because titanium is extremely reactive

to oxygen. All melting must be done in vacuum or in an inert gas atmosphere [32]. In addition, the workability of the NiTi alloy is usually performed at very high temperatures. If the alloy is cold worked it work hardens very quickly and this affects machining techniques. Both of these factors result in an alloy system that is very expensive to fabricate. One of the major advantages of this nickel-based alloy is that it can withstand large amounts of strain (approximately 8-10%) which makes it very attractive even with higher manufacturing costs. Other advantages include excellent corrosion resistance, good stability and fatigue life, along with electrical and mechanical properties. Thermal stability is another advantage because the copper-based systems start to decompose at about 120°C, whereas the NiTi alloys are stable up to 400°C [41-42].

Applications

The first industrial application of SMAs occurred in the late 1960's. During the Vietnam conflict, military fighter aircraft (F-14s) experienced long maintenance delays while repairing hydraulic lines [42]. SMA couplings were developed to assist in joining these pipes together. Cryogenic temperatures were used to convert the material to the martensitic phase. The couplings were then enlarged so that they could easily slide over the pipes. Heat was then used to convert the material back to its parent form. This transformation caused the couplings to contract, creating a joint that was better than welding the pipes together.

SMAs are also used for actuators because of their unique ability to sense and respond to temperature [43-45]. This ability is not normally found in conventional

actuators such as pneumatic or hydraulic devices, electromagnetic solenoids, or electric motors. These SMA actuators are capable of delivering a much larger force and motion compared to conventional actuators. Examples of commercial thermal sensing SMA actuators include air conditioning controllers, water filtration systems, thermal switches and steam traps.

Over the past several decades, SMAs have been thoroughly studied and found their way into the commercialization sector in a variety of fields [44-46]. The shape memory effect and superelasticity have enhanced metallic alloys for use in pipe couplings, joining systems, springs, temperature controllers, automotive applications, antenna for cellular phones, and eyeglass frames. Recent breakthroughs have occurred in the medical and dental fields. Catheters and guide wires are being made with SMAs so that they can easily maneuver in the blood vessels [43, 45]. Stents are made with SMAs to open and enlarge blocked blood vessels that feed the heart. Nitinol is currently being used for prosthetics because of its mechanical stability, corrosion resistance, and biocompatibility with the human body. In the dental area, arch wires for orthodontic correction are made with NiTi to aid in the movement of crooked teeth [43]. SMAs have also been used as dental implants and attachments for partial dentures.

Even with the current advancements in SMAs, there are still some difficulties that must be overcome. One major problem is the costs associated with manufacturing and machining. Because steel and aluminum are considerably lower in costs than nickel-based alloys, they will continue to dominate in the commercial sector. Another problem

is that most SMAs have poor fatigue properties when it comes to twisting, bending and compression [46-48]. A steel component with the same loading may survive for more than one hundred times more cycles than a SMA component.

Shape Memory Ceramics

The shape memory effect and superelasticity has also been observed in ceramic materials such as partially stabilized zirconia (ZrO_2) and ferroelectric lead zirconate titanate ($\text{Pb}[\text{Zr}, \text{Ti}]\text{O}_3$) [1]. Shape memory ceramics (SMCs) also have the ability to change from one crystal structure to another through a phase transformation that is also temperature dependent. This phase transformation is very similar to the 'martensitic' transformation found in SMAs, but it is commonly referred to as the 'ferroelastic' phase transition because it occurs in ferroelectric materials [49]. The temperature at which this transformation occurs is referred to as the Curie temperature (T_C), after the two brothers that first discovered this phenomenon in ceramic materials [50].

At higher temperatures the ceramic material will have one crystalline structure often referred to as the parent phase. Below the T_C the material can have two different crystalline structures, depending on the type of external stimuli applied. It is at this lower temperature phase that SMCs can easily be deformed or changed. The main difference between SMAs and SMCs is that the deformation is associated with an electric field-induced phase transition instead of a stress-induced phase transition. This change in shape caused by an electric field is why most ceramic materials are referred to as 'ferroelectric' [49]. As the temperature is increased back above the transformation or

Curie temperature, these SMCs revert back to their original parent shape and crystalline structure.

There are two different phase transitions that take place below the T_C : (1) paraelectric to antiferroelectric and (2) antiferroelectric to ferroelectric [1]. The first transformation is caused by a thermally-induced phase transition and the second is caused by an electric field-induced phase transition. All of these phase transitions will be discussed in detail later on. For the purposes of simplicity, the main focus of this discussion will be on the lead zirconate titanate (PZT) based ceramics such as barium titanate (BaTiO_3) because all three phase transformations are observed.

History

The first shape memory effect in ceramics was accidentally discovered by Pierre and Jacques Curie in 1880 [50-51]. At the time, they were studying the effect of temperature on the electrical properties in Rochelle salt crystals (sodium potassium tartrate tetrahydrate). During these experiments they observed that when stress in the form of a weight was applied to these crystals they became electrically polarized.

A year later, Gabriel Lippmann [50] mathematically deduced from fundamental thermodynamic principles that this process should work in reverse. The idea was that if an electrical charge was applied to these Rochelle salts, the crystals would expand or contract based on the polarity of the applied field. The Curie brothers tested this concept and proved that it could indeed work both ways. Over the next 25 years, extensive work

was conducted to identify nearly 20 different natural crystal classes of piezoelectric materials.

It was not until World War I that Langevin and coworkers [51-52] effectively utilized these materials to produce an ultrasonic submarine detector called sonar. The transducer was composed of a series of thin quartz crystals glued between two steel plates. By emitting a high frequency “chirp” underwater, they could measure depth by figuring how long the echo would return. Because these ceramics demonstrated limited performance (i.e., small electrical discharge or deformation), it was not cost effective to try and commercialize them at the time. Then in 1921, Valasek [53] discovered ferroelectricity while investigating the dielectric properties in Rochelle salt crystals. Ferroelectricity is the ability to hold and maintain a spontaneous polarization even after the applied field has been removed.

Most ceramic materials are commonly used as electrical insulators because they do not conduct a current when an electrical field is applied. However, that does not mean that ceramics are unaffected by this electric field. For some ceramic materials this applied field can cause a slight shift in the balance of a charge within the crystalline structure to form an electric dipole [54]. This is where the term “dielectric” came about because a dipole was formed with the application of an electric current. The amount of polarization or charge storage capability of a material is often referred to as its dielectric constant. Materials with low dielectric constants are used as electrical insulators, while those with high dielectric constants are used in capacitors for charge storage.

Most of the dielectric materials made in the early 1900's had a dielectric constant below 10 [54]. It was not until the late 1930's that ceramic materials with dielectric constants of 80-100 were finally developed. A major breakthrough occurred during World War II when another substance was discovered to have this same charge storage capability. Wainer and Salomon [55] were the first to develop barium titanate with a dielectric constant of 1200 to 1500. This was several orders of magnitude higher than its predecessors and led to widespread applications. In 1947, the first commercial device to be made from this piezoelectric barium titanate was a phonograph pickup. Then in 1955, further research led to the discovery of another piezoelectric material called lead zirconate titanate (PZT). These PZT materials were eventually used as transducers and actuators in the late 1950's.

Piezoelectricity

Piezoelectric materials have two unique properties that are interrelated [50, 56]. When they are deformed (i.e., compressed, twisted or distorted), a small but measurable electrical discharge is emitted. Conversely, when an electric current is passed through these piezoelectric materials, they experience a significant change in size or shape. The charges on the surfaces of these crystals (either positive or negative) were proportional to the pressure exerted and disappeared when the pressure was withdrawn. If these same crystals were exposed to an electric field they would expand or contract according to the polarity of the applied field. Strain control that is activated by pressure or electricity is commonly referred to as a "piezoelectric" material [57] and originated from the Greek word piezin which means "to press or squeeze".

Ferroelectric quartz ceramics are also considered piezoelectric materials because they contain a perovskite structure. Other ceramic materials that contain this structure include lead titanates, lead zirconates, lead zirconate titanates, barium titanates, and barium tantalate. Details on why this structure is important will be discussed later on. What is important to note is that all of these materials produce an electrical charge when a load is applied resulting in deformation. This property makes piezoelectric materials very useful for pressure or load sensors. If the process is reversed and an electric field is applied, the piezoelectric material produces a force or deformation can occur which makes them useful for microactuators, nanoactuators or piezoelectric motors.

Mechanism

SMCs have different phases that can occur due to a change in temperature similar to SMAs. Typically there are three states that can exist for SMC materials: paraelectric, antiferroelectric and ferroelectric [1]. Above the T_C the ceramic material has a parent phase called the paraelectric phase which is a cubic crystalline structure with no well-defined polarization direction (Figure 2.3a). Without this polarization direction, these paraelectric crystals do not have an electric dipole moment. If the crystal is subjected to a small electric field, it will temporarily possess a net polarization aligned with the applied field. However, when the applied field is removed it will return back to its original zero state.

As the temperature is cooled below the T_C the material changes to the antiferroelectric phase (Figure 2.3b). The effect here is similar the martensitic

transformation that occurs in SMAs [58]. During this phase transformation the crystal changes from a cubic to a tetragonal crystalline structure with a well-defined anti-polarization state. Domains that are adjacent to each other will have opposite charges that cancel each other out resulting in an overall net zero effect. If an electric field is now applied, the material will transform from the antiferroelectric phase to the ferroelectric phase (Figure 2.3c). Domains that are aligned with the applied field will increase in size, while those opposite to the applied field will decrease in size. This phase transition can result in a distortion of the crystal lattice creating a net volume expansion or strain of nearly 1% within the material [59-60]. Even after the electric field is removed, the material will still maintain its polarized and deformed shape.

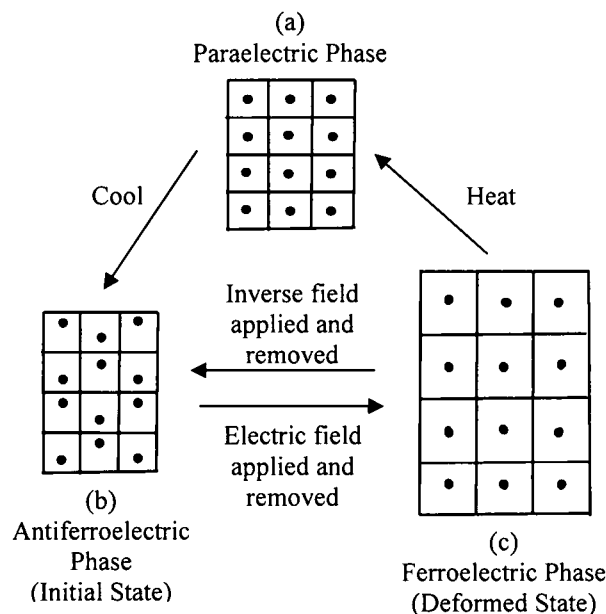


Figure 2.3: Modified phase transformations for (a) paraelectric, (b) antiferroelectric, and (c) ferroelectric shape memory ceramic materials [1]

There are several advantages that can be gained by utilizing the strain associated with this phase transition. The first is the large actuation capability that can be attained from these high strain levels. The second is that residual strains still exist even when the electric field is turned off. If the electric field is reversed in the opposite direction, the material will return back to the antiferroelectric state and the strain will be removed. The only way to go back to the paraelectric phase from the ferroelectric phase is to heat the material back above the T_C .

Dipole Effect and Polarization

To help illustrate the dipole effect and spontaneous polarization, the crystal structure of barium titanate (BaTiO_3) will be used as an example. Figure 2.4 shows barium titanate has a perovskite crystal with the ABO_3 type microstructure [55, 61-63]. When the temperature is raised above the T_C the parent phase has a cubic crystal structure (Figure 2.4a). The larger barium cations (Ba^{2+}) are situated at the corners of the cube (grey circles) and the oxygen anions (O^{2-}) are located at the face centers (blue circles). At the center of the cube is the smaller titanium cation (Ti^{4+}) shown as a black circle. Since the cations and anions are aligned with each other the structure does not have an overall polarization. If an electric field is now applied, the Ti^{4+} cation will shift its position resulting in polarization. However, if the applied field is removed the Ti^{4+} cation will return back to its original position. This is commonly referred to as the paraelectric phase and it does not exhibit the piezoelectric effect.

When the temperature drops below the T_C and an electric field is applied, there is a slight change in the crystal structure. Both the Ba^{2+} and Ti^{4+} ions shift their orientation relative to the O^{2-} ions. The net effect is a displacive transformation from a cubic structure to a tetragonal or rhombohedral structure [62-63]. Figure 2.4b is an exaggerated illustration of the electric dipole formed in each crystal by the separation of these cations and anions. The Ti^{4+} ion moves off center along with the O^{2-} ions creating a spontaneous increase in the positive charge in the same direction. In addition to a spontaneous polarization there is also a spontaneous strain that is generated from the separation of cations and anions. Dipoles that are next to each other will align to form regions called domains. The result is a net dipole moment within that domain with a net polarization. Since the direction of polarization in neighboring domains is random, the ceramic element has no overall polarization.

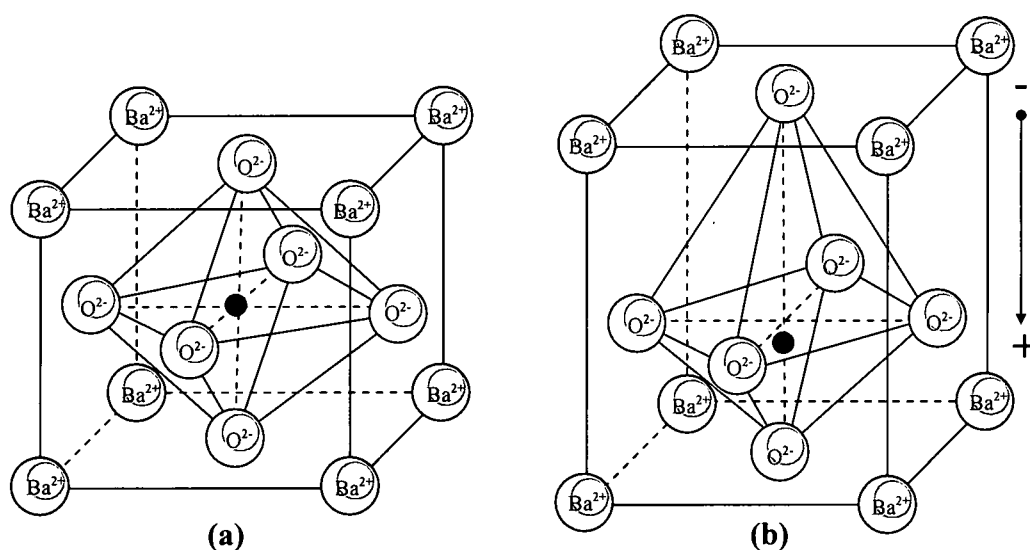


Figure 2.4: Modified illustration of barium titanate (a) with cubic crystal and (b) tetragonal crystal structure [61]

Domain Switching

Ferroelectric materials have the ability to deform and change polarization by the mechanism of domain switching [55, 61, 63-64]. Domains are regions inside the crystal with their dipole moments aligned in the same direction. Figure 2.5a is a modified illustration of an antiferroelectric crystal with domains that are polarized in different directions. Even though the domains are randomly oriented, domains that are adjacent to each other are polarized in opposite directions. The net polarization depends on the difference in size and direction of the domains, but as a whole the system appears to be unpolarized.

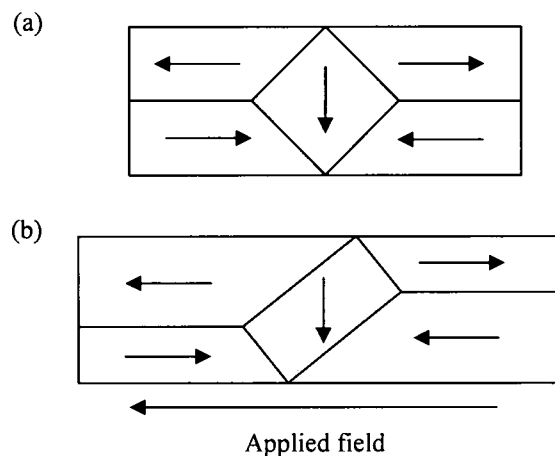


Figure 2.5: Random orientation with (a) adjacent domains polarized in opposite directions and (b) domains aligned with an electric field with a net polar effect [61]

If an electric field is now applied, the domain boundaries will change in size and shape proportional to the applied field. Figure 2.5b illustrates how domains aligned with the electric field will grow in size, while those aligned opposite to the electric field will decrease in size [65]. Two conditions necessary in a material to classify it as ferroelectric

are (1) the existence of spontaneous polarization and (2) a demonstrated reorienting of the polarization.

Applications

Most of the current commercially available SMC materials are ferroelectric polycrystalline ceramics (i.e., barium titanate, lead zirconate titanate, lead metaniobate and lead magnesium niobate) [55, 61-62]. These ceramic materials are easier to fabricate than single crystals, which is why they are relatively inexpensive to manufacture. Because they are ceramic materials, they are also physically strong and chemically inert. Some of the major applications include latching relays, mechanical clampers, ultrasonic transducers, speakers, measurement devices, filters, resonators, and high voltage devices [51].

Ferroelectric ceramic materials have also been widely used in a variety of applications including modulators, deflectors, optical memory imaging devices, and non-volatile data storage elements [66]. Another major area of influence is in their applications as actuators and sensors in smart materials and structures. The lead zirconate titanate ceramics are the most widely used in applications involving light shutters, micro-positioning devices, medical imaging processes and medical array transducers [67]. The lead metaniobate ceramics have provided excellent electrical characteristics for use in transducers for nondestructive testing, high temperature applications, and high resolution medical applications [68].

Since these crystals can acquire a charge when distorted, they can provide a convenient transducer effect between electrical and mechanical oscillations [69]. For example, the element keeping track of time inside a quartz watch is a small piece of vibrating quartz. These same quartz crystals are also being used for radio frequency transmitters. Piezoelectric ceramic materials that can produce motions on the order of nanometers have been used in the control of scanning tunneling microscopes. Within the past few years these ceramic piezoelectric materials have been used as buzzers inside pagers and cell phones, shakers inside ultrasonic cleaners, spark generators inside electronic igniters, and strain sensors inside pressure gages [50]. Rigid strains induced by an external field have enabled these piezoelectric ceramics to be used for ultraprecision cutting machines and dot matrix printer heads.

Thermally-induced SMAs that are used as actuators can show relatively large strains. Unfortunately they require large amounts of energy and can exhibit a slow response. SMCs such as field-induced piezoelectric and electrostrictive actuators have been developed because of their high efficiency, quick response, and compact size. Even though these materials have smaller induced strains than SMAs, there is no generation of heat or magnetic fields [70]. So the major advantages of using ceramics over alloys are quicker response times; good controllability to memorize and recover the shape without generating heat; and lower energy consumption.

Shape Memory Polymers

Even though SMAs are the most widely used shape memory material, there are some drawbacks (i.e., high stiffness, high costs, high density, small recoverable strains, inflexible transition temperature, toxicity issues, difficult processing conditions, etc.) that limit their applications [1-2, 4]. These limitations have lead to the development of alternative shape memory materials. Within the last few decades there has been a growing interest in a new class of materials called shape memory polymers (SMPs). Some of the advantages of these SMPs include light weight, low cost, large recoverable strains, adjustable transition temperatures, and easy to manufacture and process. One major drawback is they are limited in their practical use due to lack of recovery stress. Polymers can only store about 1/100 the amount of stress that SMAs can [71]. The main reasons why polymers are so flexible and can be easily deformed is because the storage modulus or stiffness is limited to several MPa, compared to 200 MPa for SMAs.

The morphology of most SMPs is semicrystalline [72] or amorphous compared to the completely crystalline structure of SMAs and SMCs. A semicrystalline polymer is composed of both amorphous and crystalline regions. The amorphous regions show no long range order and the chains are randomly entangled, whereas the crystalline regions have a high degree of order due to the folding and stacking of the polymer chains. Although there are some polymers that are completely amorphous, the vast majority of the SMPs are semicrystalline materials.

SMPs also possess superelasticity and shape memory effect that can be thermally activated by a transition temperature. What separates them from SMAs and SMCs is that the transition temperature (T_{trans}) can be either a glass transition temperature (T_g) or a melting temperature (T_m) [1-2, 4]. The temperature corresponding to a polymers transition from a glassy rigid state to a rubbery state is referred to as the glass transition temperature (T_g). When the temperature is above the T_g , the material exists in a rubbery state and below it exists in a glassy state. For the melting temperature (T_m) this is not the temperature at which the polymer melts, but the temperature at which crystals formed within the polymer melt. In addition to being thermally activated, SMPs can also be triggered by light (photons) [10] and chemical reactions [1]. A few of these triggering mechanisms will be briefly discussed, but the major focus of this discussion will be on the thermally activated mechanism since it produces the largest deformation change.

There are three criteria that a polymer should have to be considered a good shape memory material: a sharp transition temperature, a rubbery region or plateau, and recoverability [4]. A number of polymers (i.e., polyethers, polyacrylates, polyurethanes, polyamides, polynorbornene, styrene-butadiene copolymers, polyisoprene, and cross-linked polyethylene) have been found to have these characteristics [2-4, 73]. The vast majority are temperature sensitive functional polymers because they consist of two phases: a fixed phase and a thermally reversible phase. The fixed phase is composed of physical or chemical crosslinks, whereas the reversible phase is usually composed of flexible soft segments where crystallites can form.

History

Based on earlier definitions of what constitutes a true shape memory material, the first SMPs were probably discovered in the late 1960's [4, 74]. This was a covalently crosslinked polyethylene that was used as a heat shrinkable tubing and films. By the 1980's, Shirai and Hayashi [75] developed a crosslinked polyethylene that utilized the glass transition temperature (T_g) as the switching mechanism. The Mitsubishi Heavy Industries Company used these new shape memory materials as auto chokes and thermal sensitive switching valves. SMPs were first introduced in the United States in the mid 1980's and demonstrated a distinct shape memory effect when a thermal stimulus was applied. The result was a radical change from a rigid polymer to a very flexible elastic one and then back again to the rigid state. In its elastic state, the polymer could be deformed and then recover its original shape using a transition temperature. The recovery came from the stored mechanical energy attained during the deformation and cooling of the material.

By the mid 1990's, Lendlein and Langer [2, 7, 76] had developed polymers that utilized this same switching mechanism. However, instead of just one switching mechanism they used either the glass transition temperature (T_g) or the melting temperature (T_m) of the crystallites. As a result of their discovery, they formed a small company for the commercial exploitation of shape recovery materials. Their primary focus was in the biomedical field because these polymers could be tailored to react to body temperatures and they were biodegradable.

In contrast to SMAs and SMCs that have a rigid structure, SMPs can show a radical change from a normal rigid polymer to a very flexible elastic polymer and back on command. This change can be repeated over and over without significant degradation of the material. As a result of this radical change, the transition process for SMPs is more of a thermo-molecular relaxation rather than a thermally-induced crystalline phase transformation found in SMAs and SMCs. When compared to other shape memory materials, SMPs demonstrate a much broader range and versatility in shape configuration and manipulation.

Mechanism

A shape memory polymer is basically a super-elastic rubber. When heated above the glass transition temperature (T_g) to its rubbery state, it can be deformed under resistance. Figure 2.6 is a modified illustration of a SMP deformed under tension. As the polymer is stretched, the chains become elongated and ordered along the deformation direction (Figure 2.6b). As the temperature is decreased below either the T_g or T_m , the deformed shape is frozen by vitrification in the lower temperature glassy state or by the formation of crystallites (Figure 2.6c). Any mechanical energy exerted on the material during the deformation is now stored in the polymer chains [77]. These SMPs can maintain this new temporary shape almost indefinitely. As soon as the temperature is raised back above the transition temperature, the polymer will return back to its original shape (Figure 2.6d). This entire process is driven by the entropic energy of the polymer chains to return back to their original entangled state or conformation.

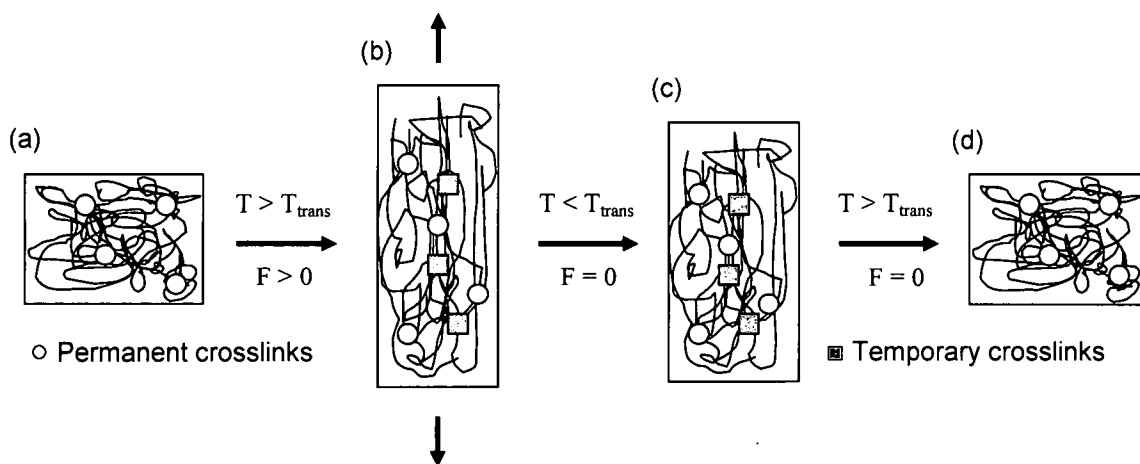


Figure 2.6: Shape memory effect in polymers (a) original or parent phase, (b) deformation to temporary shape, (c) force removed to reveal new strain set, (d) temperature increased to recover original shape [75]

Based on their response to heat, polymers can be classified as either thermosets or thermoplastics [78]. Thermosets are defined as highly crosslinked three dimensional network structures connected by strong covalent bonds. During the polymerization process, temperature and/or pressure can be used to cure the material and lock in the original shape. This reaction is irreversible, so once the polymer is set it cannot be reprocessed or formed into other shapes. Because thermosets are chemically crosslinked, they are considered amorphous materials with only a few regions that may be crystalline. In general, there are no chemical crosslinks in thermoplastics. Instead, they have more physical crosslinks such as chain entanglements, ionic bonds, hydrogen bonds, and microphase clusters to help maintain the three dimensional structure. When cooled below the T_g the polymer can retain its semicrystalline structure, but becomes hard, brittle, and glasslike.

Semicrystalline thermoplastic polymers have both amorphous and crystalline regions. The amorphous regions are composed of long polymer chains with no long range order and the crystalline regions have a regular, repeating three-dimensional arrangement of molecules. Figure 2.7 is a modified illustration of the amorphous and crystalline regions that may exist in thermoplastic polymers. The amount of crystallinity present depends on the method of preparation and thermal history. These crystallites have a melting temperature (T_m) that is associated with the upper use temperature. In contrast, the amorphous region has a glass transition temperature (T_g) that relates to the mechanical properties of the polymer [79].

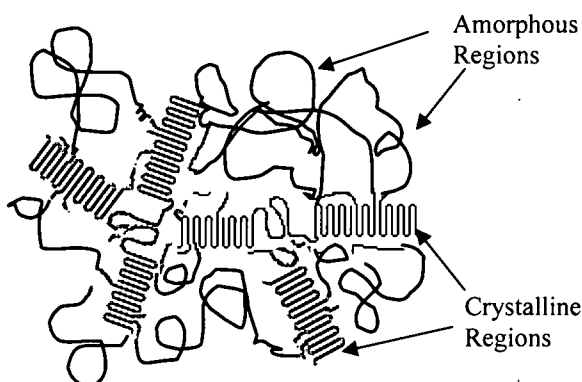


Figure 2.7: Semicrystalline polymer with amorphous and crystalline regions [80]

SMPs are composed of a “fixed” phase and a “reversible or switching” phase [81-82]. For the fixed phase, there are two types of crosslinks that are responsible for maintaining the original structure: physical crosslinks (usually associated with thermoplastics) and chemical crosslinks (usually associated with thermosets). As for the reversible or switching phase, this can be also subdivided into two different categories.

The first is a SMP with amorphous switching segments where the transition temperature is the glass transition temperature (T_g) and the second is a SMP with crystalline switching segments where the transition temperature is the melting temperature (T_m) of the crystallites.

Chemical and Physical Crosslinks

Liu and coworkers [4] have determined three characteristics for a polymer to be classified as having good shape memory properties: a sharp transition temperature, superelasticity above the transition temperature, and complete fixing of the temporary shape without creep taking place. They have classified SMPs into four categories based on their shape fixing and shape recovery mechanisms. Shape fixity is the ability of the polymer to lock-in a new temporary shape and maintain this shape until an external stimulus is applied. Shape recovery refers to the ability of the polymer to return back to its original shape. The four classes of SMPs are:

1. Chemically crosslinked glassy thermosets – these are polymers that have covalent crosslinks that are difficult to reshape after they have been formed. They feature a sharp T_g at the temperature of interest and the secondary fixing occurs through vitrification.
2. Chemically crosslinked semicrystalline rubbers – these polymers also have covalent crosslinks, but the secondary fixing occurs by crystallization rather than vitrification.
3. Physically crosslinked thermoplastics – because they are thermoplastics, they have the advantage of being reshaped. The formations of crystalline or rigid

amorphous domains are the physical crosslinks that maintain the secondary shape during deformation.

4. Physically crosslinked block copolymers – these polymers consist of hard and soft segments. The hard segments form physical crosslinks by polar interactions, hydrogen bonding, or crystallization. The soft segments can also form crystallites which are used for fixing the secondary shape.

External Stimulus

There are a number of external stimuli that can be used to deform the shape memory material and recover the deformation. For SMAs a transition temperature and force (i.e., tension, compression, torsional, etc.) was utilized. For SMCs, a transition temperature and an applied field (i.e., electric or magnetic) was needed. SMPs are more diverse since they can respond to a wide variety of external stimuli (e.g., temperature, pressure, chemical reactions, light, UV radiation, pH, electric fields, magnetic fields, etc.) [1-2, 8-14]. The resulting response can be changes in phases, shape, optics, mechanical strengths, electrical and thermal properties, reaction rates, and permeation rates. This discussion will briefly focus on the thermally-responsive, chemically-responsive, and photo-responsive types of stimuli.

Thermally-responsive. These SMPs are characterized by triggering segments and crosslinks [76-82]. The triggering segments usually have a thermal transition within the temperature range of interest and the crosslinks are used to lock in the permanent shape of the material. These triggering segments can be activated by a glass transition (T_g) or

melting temperature (T_m) to temporarily lock in a new shape and/or recover back to its original shape. For T_g , when the temperature is lowered to the glassy state the strain is frozen because the mobility of the polymer chains is decreased. For T_m , newly formed strain-induced crystallites act as crosslinking points in the polymer network. These newly formed crosslinks are responsible for locking in the deformation and the temporary shape is fixed. As the temperature is increased above the transition temperature (rubbery or melting state), the polymer chains are allowed to move and relax back to their original shape. The recovery from a thermally-responsive mechanism can be on the order of several hundred percent.

Chemically-responsive. Some SMPs contain pendant groups that can react to chemical changes and dissociate into ions [1]. With the addition of acidic or basic solutions, the polymer expands or contracts and the structure is temporarily fixed. The polymer shape is reversibly controlled by chemical reactions within the polymer structure. It should be noted that the recovery from this type of stimulus is relatively small compared to the thermally-responsive stimulus.

Photo-responsive. For these SMPs the structure is transformed under light or photo irradiation to other isomers. This transformation can be reversibly controlled by thermal or photo-chemical reactions (i.e., photons, electrons, or electrochemical reactions) within the polymer structure. There are four distinct ways for this response to occur: trans-cis isomerization, zwitter ion formation, ionic dissociation, and ring-formation/ring-cleavage [1]. Although the recovery from these four is relatively small,

recent developments with ultraviolet (UV) radiation have shown some promising results similar to the thermal-response. Lendlein et al. [11] have recently developed a new SMP that uses UV light to fix the temporary shape. Cinnamic acid groups have been incorporated into the polymer matrix that can react to different wavelengths of UV light. By stretching the polymer and then exposing it to wavelengths greater than 260 nm, these groups create physical crosslinks that lock the strain in place. To return back to its original shape, the polymer is then irradiated with a UV light wavelength less than 260 nm. Since the cinnamic groups are photosensitive, this lower wavelength will cleave the crosslinks formed.

Applications

Traditionally, SMAs and SMCs have played an important role in both actuation and mechanical coupling between actuators [5-6, 82]. However, SMPs are starting to gain interest in this area because they have a relatively large rubber elasticity which gives them the advantage of high strain (~ 100 - 1000%) when compared to SMA ($\sim 8\%$) and SMC ($\sim 1\%$). Another advantage is that the transition temperature can be tailored to the desired application requirements. This is done by varying the concentration of different polymers used in the fabrication of the shape memory material. The ability to tailor the polymer for a specific need is very important in the manufacturing world.

By varying the chemical composition, SMPs can be tailored to have both biocompatibility and biodegradability [7, 83]. This provides an excellent opportunity for SMPs to be used in the area of biomedicine. Synthetic implant materials have made

dramatic advancements for medical treatments such as minimally invasive surgery. Examples include medical devices such as self-triggering stents, catheters, splints, scaffolds for tissue engineering, contact lenses, and auxiliary devices [84-86]. These new devices can be deformed and then surgically implanted within the human body. Normal body temperature or other forms of energy can be used to trigger the material to spring back to its original shape.

Researchers are currently developing potential uses of shape memory polymers in textiles and clothing. Physical properties such as water vapor permeability and air permeability can be modified by increasing or decreasing the molecular chain lengths. The regulation of these physical properties in thin film SMPs can be used in sportswear and healthcare products [87]. Heat retaining properties of thin film SMPs at low temperatures along with gas permeability properties at high temperatures also provide excellent opportunities for sportswear. In other applications, a coat or jacket that has been treated with a SMP that can sense and respond to rain would be useful. The SMP could change its shape to keep the moisture out while still being comfortable to wear. If the weather becomes cooler, the polymer coating can change to keep the heat inside. Another example of using SMPs in textiles is by using humidity as the triggering mechanism. By adjusting the chemical structure of a SMP, it can be tailored to respond to a specific humidity level. This will allow SMPs to be used in disposable hygiene products such as diapers and moisture resistant products.

This shape memory effect in polymers is also gaining attention with the U.S. Department of Defense. The Air Force Research Laboratory has recently focused on a Morphing Aircraft Structures program [88]. By incorporating SMPs into the wing of an aircraft, they can change its shape while in flight. Two wings have been developed that can change their shape during flight.

CHAPTER III

NANOPARTICLE FILLERS IN SHAPE MEMORY POLYMERS

Within the last few years there has been an enormous interest in polymer nanocomposite materials because they offer the promise of substantial improvement in mechanical properties with very low filler loadings [73, 89-92]. A polymer nanocomposite is a two-phase system composed of a polymer matrix filled with nanosized reinforcing particles. Most recently the focus of attention has been on the carbon-based nanoparticles such as carbon black, carbon nanotubes, and carbon nanofibers because of their high aspect ratio and surface area. Carbon nanotubes (CNTs) and carbon nanofibers (CNFs) are simply graphene sheets rolled up into a cylindrical shape and linked along the length. The length scale of these two types of nanoparticles is usually in the size of micrometers with diameters up to 150 nm [15]. These particular carbon-based nano-structured materials can be divided into three categories based on their diameter: (i) single-wall carbon nanotubes (SWNTs) with diameters from 1 to 3 nm; (ii) multi-wall carbon nanotubes (MWNTs) with diameters ranging from 10 to 50 nm; and (iii) carbon nanofibers (CNFs) with diameters ranging from 50 to 150 nm [16-17]. Both SWNTs and MWNTs are usually produced in limited quantities whereas vapor grown CNFs can be produced in large quantities at low cost. The specific arrangement of the hexagon rings along the tubular surface will determine if they can be metallic or

semiconducting [16]. Because of their extraordinary properties, they are considered attractive candidates in number of applications such as fillers in polymer matrixes.

The main focus of this research effort is to try and understand how nanoparticles impact two SMP systems that use different mechanisms for locking in the deformation. An extensive literature search was conducted to find papers that showed the impact of nanoparticle fillers on the shape memory properties of these systems. Even though there were a limited number of published papers in this area, the general conclusions imply an improvement in the modulus and strength of the nanocomposite, but a reduction in some of the shape memory properties (i.e., shape fixity, percent recovery, etc.) when filled with different nanoparticles. This probably resulted from the varying degrees of dispersion throughout the polymer matrix (formation of agglomerates rather than uniform distribution of nanoparticles) and/or their impact on crystallite formation.

Li et al. [8] studied the effects of carbon black on a shape memory polyurethane containing polycaprolactone (PCL). They deduced that for strain-induced crystallization, a high degree of crystallinity of the soft segment regions was critical for the polymer to show good shape memory behavior. The main focus was on the effects of carbon black (CB) on the soft segment crystallization and melting behavior in this SMP. It was determined that an increase in CB resulted in a decrease in the degree of crystallinity and the melting temperature of the soft segment crystals. They concluded that these nanoparticles agglomerated into clumps preventing the crystallites from forming. In addition, the presence of these fillers increased the bulk viscosity of the material which

increased the relaxation time of the PCL segments in the polyurethane. This resulted in a slow strain recovery speed and low shape recovery. However, both the strain fixity and storage modulus improved with the addition of these nanoparticles.

Koerner et al. [9] discovered similar results in a different SMP called Morthane. This was a thermoplastic polyurethane elastomer (TPE) composed of both hard and soft segment regions. When carbon black (CB) and carbon nanotubes (CNTs) were incorporated into this polymer matrix, there was a distinct difference in the material properties of these two nanocomposite materials. Deformation above the glass transition temperature (rubbery state) resulted in strain-induced crystallization in the flexible soft segment regions. These newly formed crystallites acted as temporary physical crosslinks that helped lock in the deformation. When the soft segment crystallites were melted it released the deformation energy stored in polymer chains and the material entropically recoiled back to its original stress-free state. Koerner and coworkers also noticed a sharp reduction in shape memory characteristics when CB was added. Nearly four times more CB was needed to yield the same shape fixity when compared to CNTs. The addition of CNTs did show an increase in crystallite formation in the soft segment regions for this polymer system. This increase in crystallite formation enhanced the mechanical performance of the SMP system by increasing the number of physical crosslinks and providing additional reinforcement. The result was an increase in the rubbery modulus by a factor of 2 to 5 and improved shape fixity due to the enhanced strain-induced crystallization.

Gall et al. [73] studied the shape memory characteristics of a thermoset epoxy system filled with silicon carbide (SiC) nanoparticles. For this polymer system, the glass transition temperature (T_g) was used to lock in the deformation and recover strain. The thermoset epoxy nanocomposite was deformed above T_g , then quickly cooled below T_g to help fix or lock in this new temporary shape. The constraints were removed and the temperature was increased above the T_g to recover the original shape. Gall and coworkers concluded that the addition of SiC increased both the material hardness and the elastic modulus (3 fold with 40 wt% SiC) of the base SMP resin. The increase in both of these mechanical properties was a direct consequence of the relatively high hardness of the SiC particles relative to the polymer matrix. For the strain recovery experiments, samples with higher loadings of SiC generally recovered faster, but to a lesser extent.

Jeon et al. [92] studied the shape memory properties of polynorbornene (PN) filled with two different types of polyhedral oligomeric silsesquioxane (POSS). One type contained cyclohexyl corner groups (CyPOSS) and the other contained cyclopentyl corner groups (CpPOSS). The purpose of adding these nanosized fillers was to improve stability against creep by creating a unique inorganic-organic hybrid SMP with enhanced mechanical properties and thermal stability while maintaining a desirable recoverable strain. The SMP nanocomposite samples were mechanically drawn above T_g , rapidly quenched, then heated above T_g to watch strain recovery. Jeon and coworkers showed that the incorporation of POSS into PN had a slight reduction in the percent recovery, but improved thermal stability significantly. The glass transition temperature of the PN was

enhanced from 57°C to 66°C with the addition of 50 wt% CpPOSS and 73°C with the addition of 50 wt% CyPOSS due to the reinforcement of the POSS filler.

Ni et al. [93] studied the impact of vapor grown carbon nanofibers (CNFs) on the shape memory properties of a polyesterpolyol series of polyurethane SMPs. A number of experiments were conducted by deforming the SMP/CNF nanocomposite samples above, below, and at the glass transition temperature. The storage modulus, yield stress and tensile stress all increased with CNF loading at each of the different temperatures. For the shape memory properties, the shape fixity was roughly the same for all loadings (about 95%) but the percent recovery decreased with CNF loading. Ni and coworkers concluded that this reduction in the shape memory effect was due to an inclusion interaction of the CNFs in the SMP. Cyclic testing was also conducted and it was found that stable strain recovery ability could be obtained after several cycles. This phenomenon was attributed to a training effect that had taken place.

In the following chapters we will focus on how the addition of CNFs will impact the locking mechanism for a thermoplastic polyurethane elastomer (TPE) SMP system that uses strain-induced crystallization to lock in the deformation, how the CNFs interact with the TPE polymer matrix using NMR, and finally study the impact of CNFs on a thermoset epoxy SMP system that uses vitrification through the glass transition temperature. By better understanding the structure-property relationships between these two systems we may be able to determine if the addition of nanoparticles is effective for future applications.

CHAPTER IV

IMPACT OF CARBON NANOFIBERS ON THE LOCKING MECHANISM FOR A SHAPE MEMORY THERMOPLASTIC POLYURETHANE ELASTOMER

Thermoplastic polyurethane elastomers (TPEs) are linear segmented block copolymers comprised of alternating sequences of “hard” and “soft” segments. In general, the hard segments are composed of diisocyanate monomers, whereas the soft segments are composed of longer, flexible polyether or polyester diol chains [94-95]. The differences in polarity between the hard and soft segments result in microphase separated domains [96]. The soft segment domains are nominally amorphous noncrystalline regions which give rise to elastomeric behavior. The hard segment domains contain glassy and/or semicrystalline regions that provide stiffness and reinforcement to the system. From a structure-property perspective, this microphase separation between the soft and hard segments is one of the most defining features of these polymers. During tensile deformation, segments in the soft, amorphous domains uncoil, allowing the polymer to stretch several times its original length. The hard domains provide physical crosslinks, which limit long range chain untangling and enables the entropic energy stored in the soft segments to return the polymer to its original shape. When formulated into a linear polymer, TPEs combine outstanding processibility with thermoset characteristics due to the thermal reversibility of the hard segment domains.

In addition to the many elastomeric applications in aerospace, automotive, electronics, and petrochemical industries; a large portion of these polyurethanes can be used as shape memory polymers (SMPs) [2, 97-99]. These SMPs have the unique ability of “remembering” an original shape after a programmed thermal – mechanical cycle. Depending on the polymer, fixity of the temporary shape and storage of elastic energy in the form of entropically deformed chains is achieved by either a thermal quench through a glass transition temperature or the formation of strain-induced physical crosslinks such as crystallites. Recent studies [8-14, 73, 92] have demonstrated that the addition of nanoparticle fillers to SMPs can lead to improvement of mechanical properties as well as other unique characteristics, such as the ability to trigger recovery to the original state by light or current. Koerner et al. [9] demonstrated that the dispersion of 1-5 vol% of carbon nanotubes (CNTs) within a thermoplastic polyurethane SMP increased recovery stress by 50% relative to the pristine resin. In addition, different external stimuli can be used to enable shape recovery by infrared irradiation or electrical current [9, 100]. In this case, the temporary shape was fixed due to strain-induced crystallization of a portion of the soft-segments, and it recovered upon melting of these crystallites.

In this study, we will try to understand how the addition of nanoparticle fillers will have an impact on a SMP that uses strain-induced crystallization to set the strain. The SMP was a thermoplastic polyurethane elastomer called Irogran and nanocomposite films were fabricated with different loadings of vapor grown carbon nanofibers (CNFs). The formation of crystallites is critical to forming physical crosslinks that can temporarily lock in the deformation. To help understand the impact of these CNFs on set strain, we

needed to answer the following questions: (a) what was the impact of initial crystallites on the shape recovery process, (b) did the formation of crystallites by different techniques influence the setting process, (c) what was the impact of both of these processes on the shape memory properties and recovery rate, and (d) what was the effect at low strain. The results from this study will help us better understand the interaction between the CNFs and the polymer, leading to better crystallite formation and strain set.

Process history plays an important role in understanding the formation of initial crystallites during the fabrication of these SMP nanocomposite samples. We wanted to know if these initial crystallites had an impact on the recovery process or not. Secondly, there were two different ways of forming crystallites during shape memory experiments to help lock in the deformation: strain-induced crystallization and the formation of crystallite through a temperature quench. We wanted to know if there was a difference between these two methods. This would lead to further questions about the impact of these different mechanisms to form crystallites on the ability to lock in the deformation, shape recovery and recovery times. For some SMPs that use strain-induced crystallization, the addition of nanoparticles decreased the formation of crystallites resulting in slower recovery times [8-9]. If the addition of CNFs increased the crystallite content, we might be able to show an improvement in how fast these SMP nanocomposites recover. The final question involved experiments performed at lower strains. We are interested in determining if there was a substantial difference in the shape memory properties and formation of crystallites at the lower strain set (60%), which is close to the onset of strain-induced crystallization for this SMP.

In the sections that follow we will discuss the experimental tools used to analyze and evaluate these nanocomposite materials with shape memory properties. The results and discussion section will provide information on the mechanical properties (i.e., glass transition temperature, storage modulus, etc.) and shape memory properties (i.e., shape fixity, shape recovery, and recovery time) of these TPEs filled with CNFs. By comparing this data to previous work and theoretical models, we may be able to determine what the driving force is for this shape memory process. The paper will end with a brief conclusion of what we have observed and why.

Experimental

Materials

The SMP used in this experiment was TPE called Irogran PS455-203 (formerly called Morthane) which was purchased from Huntsman Polyurethanes with a density of 1.19 g/cm^3 . Data provided by carbon and proton NMR in CDCl_3 showed that the SMP (Irogran) was synthesized from $\sim 10\%$ aromatic di-isocyanate (hard segment), $\sim 32\%$ aliphatic and cyclo-aliphatic dicarboxylic acids and $\sim 58\%$ aliphatic diols (soft segments) [100]. Characterization via differential scanning calorimetry (DSC) showed that Irogran had a low glass-transition temperature ($T_g = -45^\circ\text{C}$), melting temperature of soft-segment crystallites was above room temperature ($T_{\text{ssm}} = 48^\circ\text{C}$), and melting temperature of the hard segment ($T_{\text{hsm}} = 135^\circ\text{C}$) [9].

The nanoparticle filler was a heat treated carbon nanofiber (PR-19-HHT) from Applied Science Incorporated (ASI). It was heated to 3000°C to create the most graphitic

CNF and reduce the iron catalyst content to very low levels. According to ASI, these CNFs were produced in a vapor phase with an approximate density of 2.1 g/cm^3 and chemical analysis revealed that they were 99.9% pure [101]. Using scanning electron microscopy (SEM) we were able to determine that the average diameter was $\sim 150 \text{ nm}$ with a length greater than $10 \text{ }\mu\text{m}$. These CNFs have a tubular structure with sidewalls composed of angled graphite sheets that give it a “stacked” or “herringbone” appearance. The exposed edge planes along the entire surface of the fiber are highly reactive and can provide additional opportunities for bonding or functionalization.

Processing

The Irogran/CNF nanocomposites were prepared using a solution mixing process in the following manner [102]. Solid pellets of polyurethane (Irogran) were dissolved in a polar solvent of Tetrahydrofuran (THF) at ambient temperature ($\sim 25^\circ\text{C}$) using a magnetic stir bar. The mixture was stirred for 4 hours to ensure all of the solid polymer pellets were completely dissolved. In a separate reaction vessel, a predetermined amount of CNFs were placed in a polar solvent of THF. This CNF/THF mixture was stirred for 4 hours using an Ultra Turrax IKA T18 Basic Stirring Machine at 14,000 rpm. This stirring process was used to break up any large clumps and evenly disperse the CNFs in the polar solvent. The CNF/THF mixture was then poured into the Irogran/THF mixture and allowed to mix for 24 hours using a magnetic stir bar. This long mixing time aided in dispersing the CNFs evenly throughout the polymer matrix. During this 24 hour period, the lid to the mixing container was left off to allow the majority of the THF solvent to slowly evaporate off. Once the mixture became relatively viscous, a thin layer

was poured into Teflon molds (102 mm x 26 mm x 20 mm), covered with aluminum foil and allowed to dry overnight. As the solvent evaporated, both the fixed phase and the soft segment crystallites began to take on the form of the Teflon mold. The specimens were removed from the molds and placed in a vacuum oven at 40°C for 24 hours to remove any excess THF. The samples appeared to be smooth and uniform, except for the edges of the mold where the concentration of the CNFs is less near the rim.

Morphology

The fracture topography and dispersion of CNFs were studied using a scanning electron microscope (SEM) Model FEI Sirion/XL30. Composite specimens were fractured in liquid nitrogen and adhered to metal tabs using silver paint. The surface of the fractured material was lightly coated with carbon using an Edwards Auto 306 Turbo Evaporator to enhance the appearance of the CNF's and prevent the effects of charging.

The crystallization and alignment of the carbon nanofibers was also studied using wide angle x-ray scattering (Bruker Model AXS System). Both strained and unstrained samples were analyzed to determine the amount and orientation of crystallites, along with the orientation parameters (S_d) of the carbon nanofibers. The azimuthally averaged intensity versus 2θ was obtained using the software package Fit2D [103]. The crystalline and amorphous regions gave distinct x-ray diffraction patterns.

Thermal Characterization

The glass transition temperature, melting temperature and crystallization behavior was studied using a differential scanning calorimeter (DSC) purged with nitrogen in a cooling and heating process (TA Instruments Model Q 1000). A temperature ramp method from -150°C to 150°C with a heating rate of 10°C/min was used for sample sizes ranging from 10-15 mg. The temperature corresponding to the mid-point in heat capacity was used to determine the glass transition temperature (T_g) of the polymers. The relative degree of crystallinity was calculated from the integrated enthalpy datum (ΔH_C) of the crystallization peak.

Thermomechanical Characterization

The elastic modulus and glass transition temperature were studied using a dynamic mechanical analyzer (DMA) in multi-strain mode (TA Instruments Model 2980). Micro tensile specimens (8 mm (l) x 4 mm (w) x 0.5 mm (t)) were placed in the fiber film clamps of the DMA with an initial force of 0.001 N. A temperature ramp method from -145°C to +145°C with a heating rate of 4°C/min was used for both parameters at a fixed mechanical oscillation frequency of 1 Hz. For consistent comparison between tests, the glass transition temperature (T_g) was taken to be the peak of the tan-delta curve.

All shape memory and recovery measurements were conducted using a DMA (TA Instruments Model 2980) in controlled force mode. Micro tensile specimens (8 mm (l) x 4 mm (w) x 0.5 mm (t)) were placed in the fiber film clamps of the DMA. An initial

force of 0.001N was applied to the sample to keep the film taut. The samples were stretched at 0.2 N/min to 60% strain and then the force was removed. The samples were then heated back up to 60°C to recover the deformation.

Thermal Histories

During the fabrication of these nanocomposite films, initial crystallites were formed as a result of in-plane strain during evaporation. These as-cast crystallites could play a role in how the strain is set during deformation. Both as-cast (with crystallites) and thermally annealed (without crystallites) samples were tested to determine the impact of these initial crystallites on the shape memory properties. Samples were thermally annealed by heating the as-cast films to 60°C for 60 minutes to help remove these initial crystallites.

Setting Deformation and Crystallite Formation

For this SMP, crystallite formation is critical for locking in the deformation. These crystallites can be formed through a temperature quench or by strain-induced crystallization. The following methods were used to help lock in the deformation and recover the original shape:

Method 1 (Temperature quench crystallization). The following DMA experiment was conducted to examine the mechanical energy storage via an elevated temperature deformation followed by quenching through the soft-segment crystallization temperature. Samples were heated to 60°C for 30 minutes to remove any crystallites formed during

processing. With the temperature still at 60°C, the samples were stretched at 0.2 N/min to 60% strain and held constant. The temperature was then rapidly cooled at ~30°C/min to ambient temperature (25°C). Crystallites that formed during this temperature quench, along with some strain-induced crystallization, were responsible for locking in this new temporary shape. After 30 minutes, the strain was removed and the sample was allowed to relax. After 60 minutes, the temperature was rapidly increased back up to 60°C to recover the original shape. Figure 4.1 is a 3-dimensional illustration of a typical shape memory cycle for the high temperature quench crystallization method.

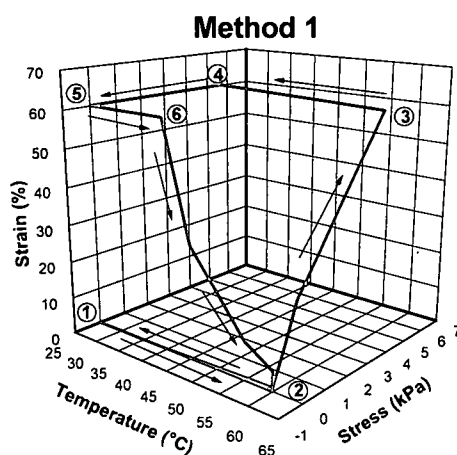


Figure 4.1: 3D plot of stress vs. strain vs. temperature for shape recovery using high temperature quench crystallization method [8]

Method 2 (Strain-induced crystallization). The following DMA experiment was conducted to examine the mechanical energy storage via a room temperature deformation resulting in strain-induced crystallization. Both as-cast (with initial crystallites) and thermally annealed samples (without initial crystallites) were stretched at 0.2 N/min to 60% strain at ambient temperature (25°C). Strain-induced crystallization along with

existing crystallites were responsible for locking in this new temporary shape. The strain was removed and the sample was allowed to relax. After 60 minutes, the temperature was rapidly increased to 60°C to recover the original shape. Figure 4.2 is a 3-D plot of a typical shape memory cycle for the room temperature strain-induced crystallization method.

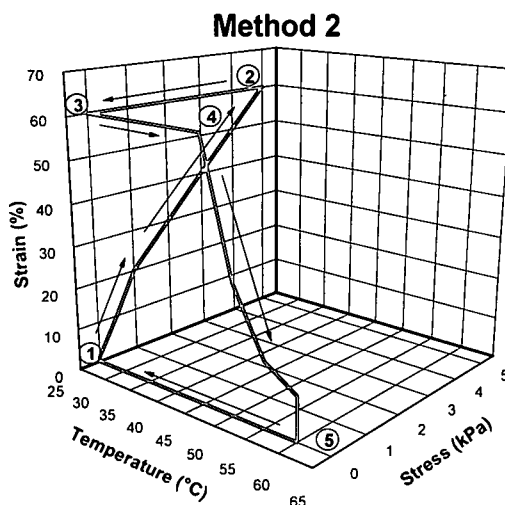


Figure 4.2: 3D plot of stress vs. strain vs. temperature for shape recovery using room temperature strain-induced crystallization method [9]

Figure 4.3 is a DMA plot of a Method 1 showing various strain values used to calculate the shape fixity and shape recovery measurements. The sample was placed in the DMA clamps at room temperature with an applied force of 0.001N (point A). To remove any process history, the sample was heated at a rate of 3°C/min to a deformation temperature (T_d) of 60°C for 30 minutes. This temperature was approximately 10-12°C above the melting point of the soft segments ($T_{ssm} \sim 48^\circ\text{C}$) for this TPE (point B). The film was then stretched to a maximum strain (ϵ_{max}) of 60% at 60°C (point C). The temperature was rapidly cooled down to a setting temperature (T_s) under constrained

conditions of constant length (point D). For this test method, ambient temperature (25°C) was chosen as the setting temperature because it was well below the melting temperature of the soft segments. When the external force was withdrawn, a contraction occurred and the strain changed from the maximum strain (ϵ_{\max}) to a set strain (ϵ_{set}). This set strain (ϵ_{set}) was referred to as the fixed strain, which meant that the film specimen moved from point D to point E. The specimen at point E was then used for studying the shape recovery behavior in a process of constant heating rate. The strain recovered after heating (ϵ_{rec}) is referred to as the residual strain or permanent deformation (point F). The maximum strain (ϵ_{\max}), set strain (ϵ_{set}) and recovered strain (ϵ_{rec}) were used to define shape fixity and shape recovery [99, 104].

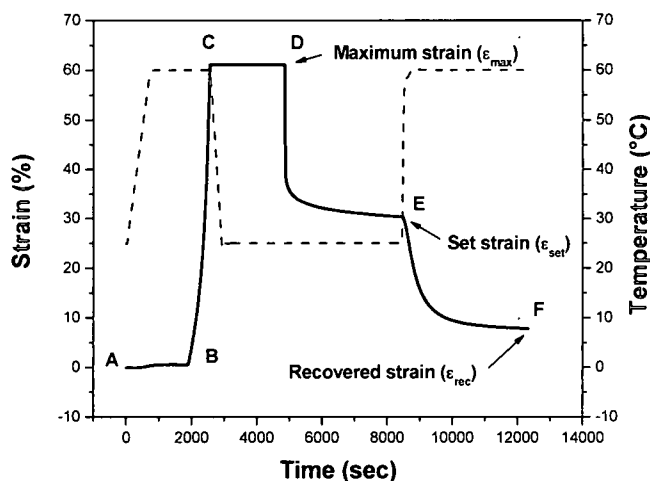


Figure 4.3: Typical DMA scan of a shape recovery experiment

Shape fixity is the ability of the polymer to lock in the deformation and maintain its new temporary shape when the force is unloaded [2, 4]. It more accurately describes how well the locking mechanism (either vitrification or strain-induced crystallization)

will “fix” the mechanical deformation. This parameter is calculated from the ratio of the unloaded or “set” strain (ϵ_{set}) to the maximum strain (ϵ_{max}):

$$\% \text{ shape fixity} = (\epsilon_{\text{set}}/\epsilon_{\text{max}}) \times 100 \quad (4.1)$$

Shape recovery is used to quantify the ability of the material to memorize its original permanent shape. This parameter determines how much of the overall strain was recovered and is calculated from the maximum strain (ϵ_{max}) minus the recovered or permanent deformation strain (ϵ_{rec}) divided by the maximum strain (ϵ_{max}):

$$\% \text{ shape recovery} = ([\epsilon_{\text{max}} - \epsilon_{\text{rec}}]/\epsilon_{\text{max}}) \times 100 \quad (4.2)$$

Samples with high shape fixity and high shape recovery are considered excellent SMPs because they can lock in nearly all of the deformation and then return back to its original or near original shape when the external stimulus is applied. Some polymers have very good shape fixity and poor shape recovery or poor shape fixity and good shape recovery.

Liu and coworkers [4] have attempted to quantify this overall shape memory performance by using a fill factor. By comparing the ratio of complete shape fixity and recovery to what was actually fixed and recovered; they could classify shape memory materials into five different types. The five classes are (a) ideal shape memory materials; (b) shape memory materials with excellent shape fixity and recovery; (c) shape memory materials with excellent shape recovery but poor shape fixity; (d) shape memory

materials with excellent shape fixity but poor recovery; and (e) shape memory materials with both poor shape fixity and shape recovery.

Results and Discussion

One of the criteria for improving shape memory characteristics with nanofiller loading is good dispersion [105]. If the nanoparticles are clumped or agglomerated together, they will lose their effectiveness as a reinforcing material. Figure 4.4 shows the SEM micrograph of the cryogenically fractured surface of a typical nanocomposite sample. The general topography of the fracture surface is the polyurethane matrix mixed with the CNFs. For the most part, there is good dispersion of the CNFs throughout the polymer matrix with a few aggregates found (approximately 5% of the entire fracture surface) with the higher CNF loadings (5.92 vol%).

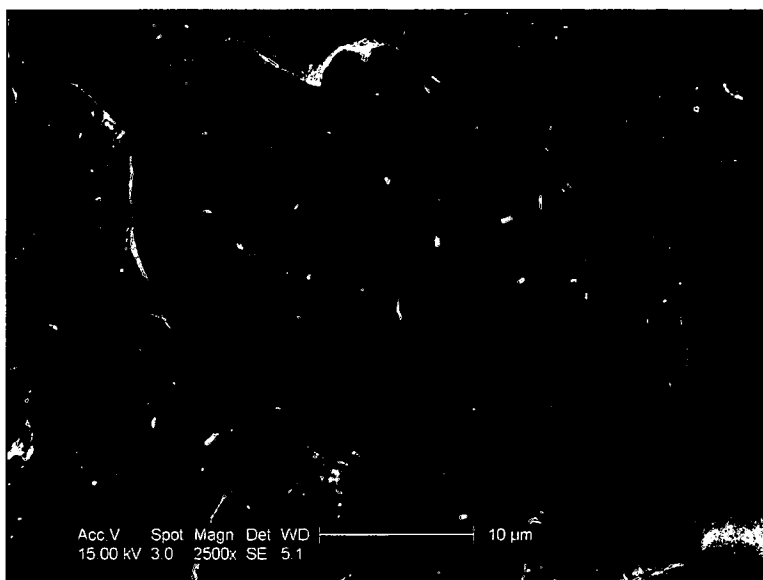


Figure 4.4: SEM image of a 2.90 vol% CNF in Irogran

The other criteria for improving shape memory characteristics with nanofiller loading is a strong interfacial interaction between the filler and the polymer. This helps transfer the load across the nanoparticle/polymer interface resulting in improved mechanical properties. From the SEM image (Figure 4.4) we can see that there is minimal fiber “pullout” of CNFs from the fracture surface. This indicates good wettability and interaction between the polymer matrix and the CNFs.

A strong interaction between the polymer matrix and CNFs should also be reflected in the glass transition temperature (T_g). Figure 4.5 shows a plot of T_g versus volume fraction of CNF using both DMA and DSC. The trend lines of the DMA ($\tan \delta$) and the 1st heating cycle of the DSC indicate that there is a slight increase in the glass transition temperature with CNF loading. There are a number of reasons why the T_g increased with CNF loading. It could be due to a lowering of the free volume space, or it could be due to secondary bonding (e.g. hydrogen, ionic, etc.) between the carbonyl in the urethane linkage and hydrogen's on the CNF, or it could be due to the formation of crystallites. Figure 4.6 shows that the crystallite content increases with CNF loading even for the as-cast samples. These initial crystallites act as temporary crosslinks that can cause the glass transition temperature to increase with higher CNF loading. When we compare the 1st and 2nd heating cycles using DSC in Figure 4.5, we can see that the trend line levels off after the 2nd heating cycle. Since the crystallites have been removed during this 2nd heating cycle, we would expect no change in the glass transition temperature. This 2nd heating cycle shows that the T_g does level off after the crystallites have been removed which would indicate that this was the reason for the increase.

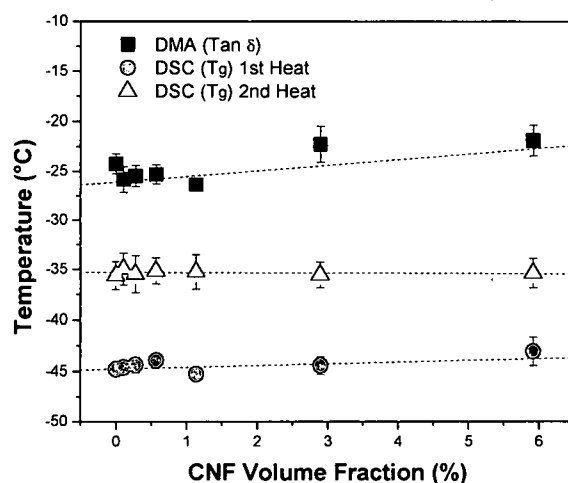


Figure 4.5: Effect of CNF loading on glass transition temperature (T_g)

Since crystallinity is important for locking in the temporary deformation we need to know if there is a direct relationship between the formation of these crystallites and the CNF loading. DSC experiments were used to measure the enthalpy datum (ΔH_C) of the crystallization peak as a function of CNF loading. Figure 4.6 shows three separate tests conducted on as-cast (unstretched) samples, thermally annealed samples, and the formation of crystallites through a temperature quench. For the as-cast (unstretched) samples, DSC results showed that crystallization occurred during processing and increased with CNF loading (Figure 4.6a). We suspect that residual stresses developed during the evaporation process resulted in the formation of new crystallites within the nanocomposite film. Since the CNFs are stiffer than the polymer matrix, the formation of crystallites is probably due to in-plane strain that occurs during the evaporation and drying process during film casting. Another possibility is that the CNFs are providing

more surface area for the nucleation of crystallites. To help remove this process history, the nanocomposite films were thermally annealed at 60°C for 1 hour. DSC results showed that the majority of the crystallites were removed (Figure 4.6b). To show the effects of CNF loading on crystallite formation through a temperature quench, the films were strained to 60% at 60°C, removed from the DMA and analyzed. DSC results showed that the crystallinity increased with CNF loading and was a direct result of crystallites forming during a temperature quench along with some strain-induced crystallization (Figure 4.6c). Later in the discussion, a comparison will be made between thermal histories of these initial as-cast crystallites and thermally annealed samples stretched to 60% strain. In addition, a comparison will be made between room temperature strain-induced crystallites and crystallites formed during a temperature quench.

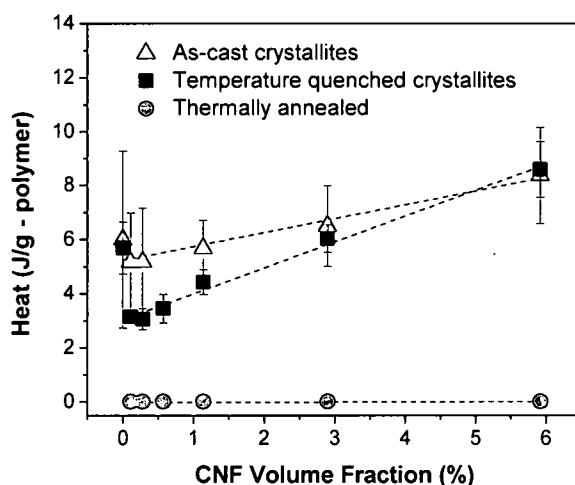


Figure 4.6: DSC enthalpy data showing the effect of crystallite formation for (a) as-cast (unstrained) samples (▲), (b) thermally annealed samples (●), and (c) the formation of crystallites through a temperature quench (■)

Wide-angle x-ray scattering (WAXS) was also used to confirm the formation of crystallites with CNF loading. Figure 4.7 shows a typical x-ray diffraction (XRD) plot of intensity versus 2θ for a neat and filled elastomer samples. The peak at 26.5° is the scattering from the CNFs and the peak at 21.8° is the scattering from the crystallites. From this plot we can see considerably more crystallites with 5.92 vol% CNFs compared to the neat polymer film. This XRD data is consistent with the previous DSC data.

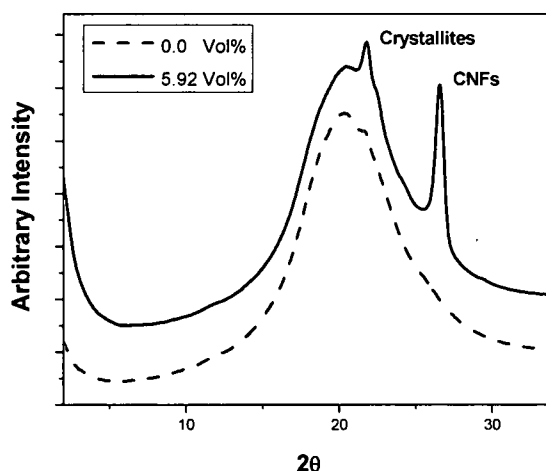


Figure 4.7: Wide angle x-ray scattering (WAXS) of neat Irogran (dashed line) and Irogran filled with 5.92 vol% carbon nanofibers (solid line)

The Young's modulus (E) or modulus of elasticity is a measure of the material's stiffness. For polymers, the modulus usually decreases with increasing temperature because the chains become flexible and can move. When filler is added to the polymer matrix, it can have a direct impact on the rubbery or elastic modulus. Figure 4.8 is a plot of the normalized storage modulus (E/E_0) versus CNF loading performed at different temperatures (0°C , 25°C , 50°C , 75°C and 100°C). From this normalize data we can see an increase in modulus with CNF loading that is independent of temperature. This tells

us that the addition of CNFs improved the stiffness of the polymer, which is consistent with previous work conducted on similar systems [73, 93, 100, 106]. This increase in stiffness with filler loading is at least partially due to the higher elastic modulus of the CNF reinforcement compared to that of the SMP matrix. Another contributing factor to this increase in modulus with CNF loading could be attributed to the formation of crystallites. These crystals tie up the soft segment amorphous chains which are responsible for storing the entropic energy during deformation. Since they act as physical crosslinks, they will enhance the modulus of the filled system.

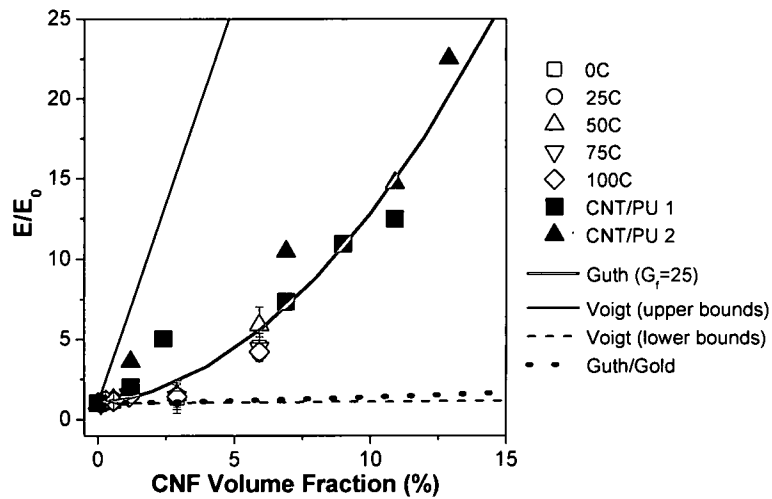


Figure 4.8: Normalized storage modulus (E/E_0) versus volume fraction (%) of carbon nanofibers

There have been numerous models that have been developed to try and understand the impact of different fillers on a rubbery modulus [107-109]. For this particular system we have used the Guth model with the following equation:

$$E/E_0 = 1 + 0.67G_f\Phi + 1.62G_f^2\Phi^2 \quad (4.3)$$

where E is the modulus of the composite material, E_0 is the modulus of the neat polymer matrix, G_f is the aspect ratio of the filler, and Φ is the volume fraction of the filler. Both upper and lower bounds to modulus enhancement derived from the axial loading using the Voigt model are also referenced in Figure 4.8.

This is a first order model that describes the reinforcement of filled rubbers with anisotropic particles such as rods. The moduli results of this nanocomposite seem to cluster along this trend line with increasing volume fraction of filler. However, there appears to be some discrepancy in relation to the effective aspect ratio. For our system, the effective aspect ratio ($G_f = 25$) is substantially lower than expected ($G_f = 100$). At first it was thought that this decrease was due to clustering of CNFs. To have an effective aspect ratio of 25, the clustered nanofibers would require a diameter of 4 individual fibers which would be approximately 16 nanofibers bundled in a circle. SEM results show that we have very good dispersion of the CNFs, so we can rule out the effects of clustering. What we believe is happening relates to the percolation threshold. If we were below the percolation threshold (< 1 vol%), most the CNFs would be isolated from each other and the normalized moduli would approach an effective aspect ratio of 100. However, since most of these normalized moduli values are above the percolation threshold there is a network of CNFs overlapping each other. Now when the system is deformed, this network is deformed and the junctions between the CNFs will give the appearance of a lower effective aspect ratio. To help confirm this hypothesis we should conduct tests below the percolation threshold and to see if the curve has a sharper incline.

Now that we have investigated the influence of CNFs on the mechanical properties, we can focus our attention on how they impact the locking mechanism during shape recovery experiments. At the beginning of this chapter we expressed concern about the formation of initial crystallites during processing. The question arose as to whether these initial crystallites would impact shape memory properties during strain-induced crystallization. In addition, there are two different ways of locking in the deformation: room temperature (RT) strain-induced crystallization and a high temperature (HT) quench crystallization above the melting point of the crystallites. Using the various strain values illustrated in Figure 4.3, we will attempt to show the impact of CNFs on the shape memory properties. A comparison will be made to as-cast samples (with initial crystallites) to thermally annealed samples (without initial crystallites) using the room temperature (RT) strain-induced crystallization method. In addition, a comparison will be made of the room temperature (RT) strain-induced crystallization method to the high temperature (HT) quench crystallization method.

Figure 4.10 is a plot of percent shape fixity versus CNF loading. For the room temperature (RT) strain-induced samples (with crystallites), the shape fixity starts out low ($\sim 10\%$) for the neat polymer and then increases with higher CNF loading ($\sim 30\%$). For the room temperature (RT) strain-induced samples (without crystallites), the shape fixity again starts out low ($\sim 10\%$) for the neat polymer and then increases with higher CNF loading ($\sim 45\%$). The impact of the initial crystallites formed during processing only slightly affects the RT strain-induced crystallization method. This would tend to indicate that the initial crystallites impact the set strain at higher loadings.

Now when we compare the different ways of locking in the deformation, the shape fixity is much higher for the high temperature (HT) quench crystallization method compared to the room temperature (RT) strain-induced crystallization methods. Either more crystallites are forming with the temperature quench method or there is flow taking place at the higher temperature. This would probably be reflected in the shape recovery experiments. The main point to note is that in all three cases, the fixity increased with CNF loading. We suspect that the CNFs are acting as nucleation sites for the crystallites to form on. More crystallites allow for more physical crosslinks to help lock in the deformation.

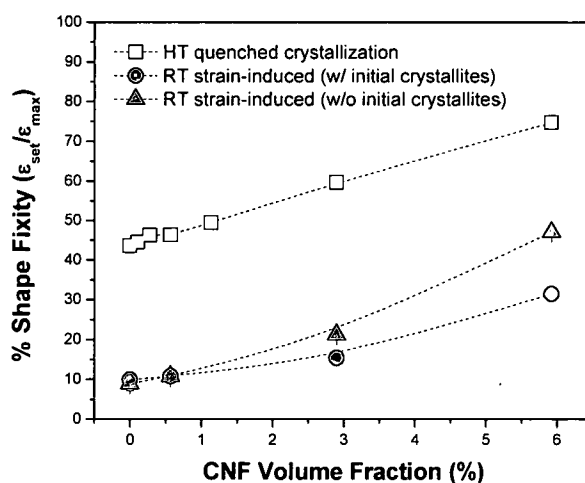


Figure 4.10: Effect of CNF loading on % shape fixity for a high temperature (HT) quench and room temperature (RT) strain-induced (with and without initial crystallites)

Figure 4.11 is a plot of percent shape recovery versus CNF loading. Both room temperature (RT) strain-induced crystallization methods show identical results with or without initial as-cast crystallites. The percent shape recovery is high (~ 97%) for the

neat polymer and decreases with CNF loading (~ 92%). This is consistent with work from similar nanoparticle filled systems because the modulus or stiffness of the polymer matrix increased with filler loading [8-9, 73, 92-93, 100, 106]. Since the shape recovery is identical for the strain-induced crystallization method (with and without initial crystallites), this would indicate that the as-cast crystallites were not a contributing factor.

When we compare the high temperature (HT) quench crystallization method to the room temperature (RT) strain-induced crystallization methods, the shape recovery values are much lower. Again, since the deformation is taking place at higher temperatures we have to consider that the system is flowing and we are experiencing more plastic deformation. There is also a decrease in the shape recovery with CNF loading. We suspect that with higher loadings we are increasing the stiffness of the material making it more difficult to return back to its original shape.

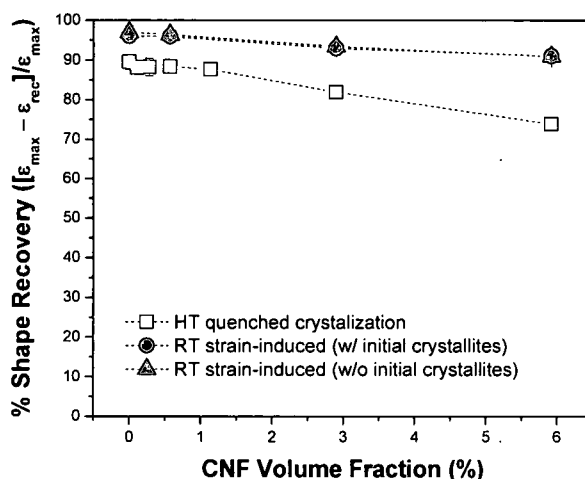


Figure 4.11: Effect of CNF loading on % shape recovery for a high temperature (HT) quench and room temperature (RT) strain-induced (with and without initial crystallites)

The strain recovery or relaxation time was taken from the set strain (ϵ_{set}) to the recovered strain (ϵ_{rec}). Initially, the strain was removed and the specimen was allowed to equilibrate before applying heat. A temperature ramp was used to melt the crystallites and allow the material to return back to its original or near original shape. A non-linear least squares fit (NLSF) analysis software package (Origin 7.5) was used to measure how fast the material recovered. Figure 4.12 is a typical DMA scan of a 1 wt% CNF/TPE sample showing the set strain (point E) to the recovered strain (point F) with a trend line calculated using the NLSF equation. From this equation, the recovery or relaxation time (t_1) was calculated using a second order exponential decay.

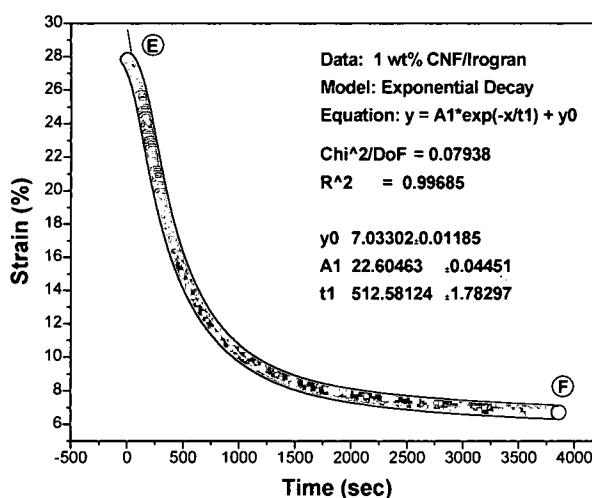


Figure 4.12: Recovery time calculated from set strain (ϵ_{set}) to the recovered strain (ϵ_{rec}) using a NLSF analysis software

Figure 4.13 is a plot of recovery time versus nanofiber loading. Both of the room temperature (RT) strain-induced crystallization methods (with and without initial crystals) showed a drop in the recovery time with CNF loading. This is contrary to recovery times reported by others showing that the recovery times were longer with

nanoparticle additions [8, 92, 94]. It was thought that the CNFs acted as a thermal conduit for the heat to transfer throughout the polymer matrix to help melt the crystallites. However, since the data tapers off with CNF loading rather than continue to drop in a linear fashion we suspect that this is not the reason for the quicker recovery. Instead, what we believe is happening is that strain enhancement is occurring near the CNFs during deformation. This is because the CNFs are not going to change their dimensions when the polymer is being stretched. So to accommodate this volume change, the strain that was originally in the CNF is transferred to the region near the fiber. Higher strain near the CNFs results in the chains being stretched more thereby yielding higher crystallinity and more strain energy stored in the polymer chains. The difference between the stretched polymers with and without CNFs is called the strain “enhancement” effect. With more strain energy stored in the polymer chains, they should recover faster to a lower energy state when the crystallites melt.

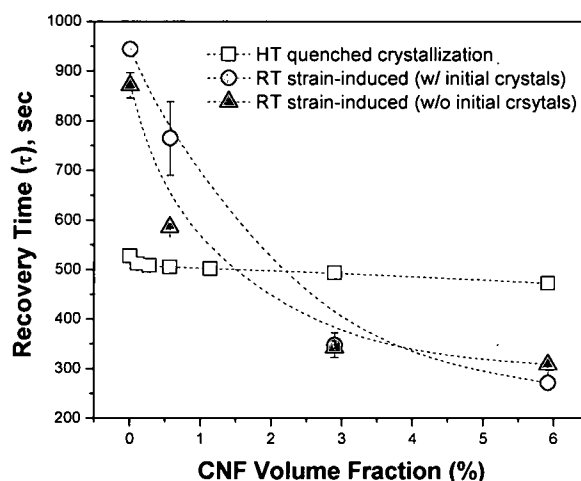


Figure 4.13: Effect of CNF loading on recovery time for a high temperature (HT) quench and room temperature (RT) strain-induced (with and without initial crystallites)

Now when we compare the high temperature (HT) quench crystallization method to the room temperature (RT) strain-induced crystallization methods, the recovery times are only slightly faster with CNF loading. Since the deformation is taking place at higher temperatures we have to consider that the system is flowing and we are experiencing more plastic deformation.

Most thermoplastic polyurethane elastomers that are deformed in uniaxial tension exhibit a nominal stress vs. nominal strain curve with three distinct regions [110]. Figure 4.14 illustrates these three regions and we can see a unique relationship between them:

- Region I: occurs at small strains that are deformed linear elastically with a typical rubber modulus. The onset of strain-induced crystallization for this SMP occurs at around 20% strain [100]. Just before reaching the next region, there is a slight nonlinear increase in the orientation of the material with nominal stress. This upper region was the main focus of our strain set because we were above the onset of crystallite formation and at the limits of the DMA.
- Region II: occurs at intermediate strains and transitions to a plateau in the stress versus strain curve. At this point there is an increase in the alignment of the carbon nanofibers and polymer chains along the stress axis. The drop in elastic modulus can be attributed to inhomogeneous deformation [111].
- Region III: occurs at larger strains and the elastic modulus begins to increase again. However, there is only a small increase in the orientation parameter at this point. This region was the focus of previous work conducted by Koerner et al. [9] since they were working with as-cast room temperature deformations.

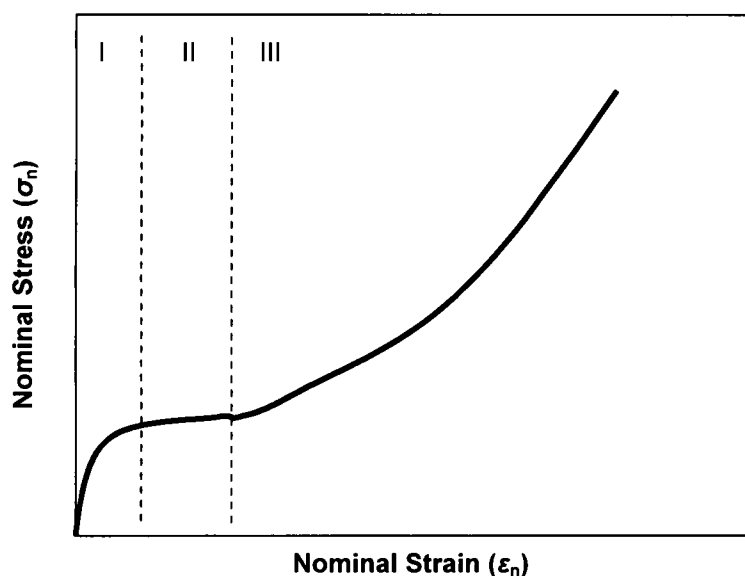


Figure 4.14: Schematic of nominal stress versus nominal strain curve for a thermoplastic elastomer [110]

Our final question asked what the impact of CNF loading would have at low strain. Since the onset of strain-induced crystallization occurred at 20% strain, we wanted to see if there was a difference when deformation was conducted just above the onset at 60% strain. When we compare these low strain results to higher strain results (250% strain) our overall results were much less. The reason for this is because strain-induced crystallization is maximized at about 150-200% strain [100]. However, we believe that the recovery rate and the impact of small strain-induced crystallites should not matter if we are doing 60% strain or 250% strain.

Conclusions

Even though there are numerous external stimuli that can trigger the recovery in shape memory polymers, we focused on the thermally-responsive because it provided the largest response. In this experiment, a thermoplastic polyurethane elastomer called

Irogran was used because it was found to have good shape memory properties. This temperature sensitive polymer system consisted of two phases: a fixed phase and a thermally reversible phase [9, 81-82]. The fixed phase was composed of the glassy hard segments and physical crosslinks to maintain its original shape. The reversible phase was the amorphous soft segment regions that could form crystallites during deformation.

SEM images indicated good dispersion of the CNFs with very little fiber pullout. DSC and DMA showed a slight increase in the glass transition temperature with CNF loading which indicated that there was some interaction between the CNFs and the polymer matrix. The storage modulus of the nanocomposite samples showed an increase in stiffness with CNF loading that was independent of temperature. This increase was partly attributed to the larger stiffness in the CNFs compared to the polymer matrix.

One of the reasons for performing these experiments was to determine if the addition of CNFs had a positive or negative impact on shape fixity, percent recovery and recovery time. By using different thermal histories, we could determine if crystallites formed during processing would impact the shape recovery experiments. For the most part, there was not that much of a difference for the strain-induced crystallization (with or without the initial crystallites). We also wanted to see if there was a difference between a room temperature (RT) strain-induced crystallization method and a high temperature (HT) quench crystallization method. Preliminary results indicated that the addition of CNFs showed improved recovery time and shape fixity with increasing nanofiber loading. However, the percent recovery decreased with CNF loading for all three thermal

history methods. The large difference between the room temperature (RT) strain-induced crystallization method and the high temperature (HT) quench crystallization method is due to flow and plastic deformation occurring at the higher temperature.

One possible explanation for the faster recovery times with CNF loading was thought to be associated with the synergism between the carbon nanofibers and the soft segment crystallites of the polymer. It was speculated that the CNFs acted as nucleation sites for the crystallites to form on; therefore, more crystallites formed with higher CNF loadings. These crystallites are the key to locking in the deformation and recovery during melting. More entropic energy is stored in the polymer chains with higher CNF loadings during the deformation process because of strain-enhancement taking place. Since the CNFs do not deform as much as the polymer chains in uniaxial tension, that strain energy is now transferred to the polymer. This enhanced strain causes more crystallites to form, resulting in higher shape fixity and faster recovery. In the next chapter we will attempt to use nuclear magnetic resonance (NMR) to better understand the interaction between the CNFs and the polymer chains.

CHAPTER V

NMR CHARACTERIZATION OF LOW HARD SEGMENT THERMOPLASTIC POLYURETHANE/CARBON NANOFIBER COMPOSITES

In microphase separated polymer systems, whether semicrystalline polymers or segmented block copolymers, the presence of nanoparticle fillers will have a substantial impact on the fundamental mechanisms of vitrification and on heterogeneous nucleation and growth of the phase morphology. For semicrystalline polymers, there have been many reports of changes in the dynamics and structure of the polymer crystallites [112-117]. These changes in morphology are likely to be a major contributor to the observed changes in the solid state mechanical properties of nanocomposites based on these polymer systems. For some shape memory polymer (SMP) nanocomposites, detailed understanding of the basis and ways to control heterogeneous nucleation, whether thermal or strain-induced, by the nanoparticles remains poorly understood, even though it is crucial to establishing future utility of these materials.

Nuclear magnetic resonance (NMR) is a powerful tool to study the structure and dynamics of complex and heterogeneous systems because the spectroscopy properties (chemical shifts, relaxation times and line widths) depend on the local structure and dynamics [18]. The challenge in understanding nanocomposites is to isolate the signal from the interfaces so that the structure and dynamics of interfacial materials can be

studied. NMR methods have been successfully applied to interfaces in clay [118-120], silica [121-122] and other composites, but the study of carbon nanotubes (CNTs) and carbon nanofibers (CNFs) has proven more challenging. This is due in part to the synthetic methods that produce mixtures of tube types and the presence of residual paramagnetic catalysts [123]. Theoretical studies have shown that the carbon chemical shift and magnetic susceptibility for single-walled carbon nanotubes (SWNTs) depends on the tube type (metallic or semiconducting), the structure, and the diameter [124]. We would expect these property variations to be even larger for multi-walled carbon nanotubes (MWNTs) or carbon nanofibers (CNFs), as they are intrinsically more heterogeneous materials. In the last chapter, the addition of CNFs to a thermoplastic polyurethane elastomer (TPE) have shown improvement in the shape-memory properties relative to the TPE, and the electrical and thermal properties of the CNFs provide additional mechanisms for actuation [9].

In this study, NMR is employed to understand the influence of dispersed vapor grown carbon nanofibers (CNF, PR-19-HHT) on the strain-induced crystallization of soft-segments within thermoplastic polyurethane with low hard segment content (Irogran, PS455-203). The thermoplastic polyurethane is distinguished by a much lower fraction of hard segments (less than 10%) than conventionally encountered in the majority of polyurethanes (~ 40-50%) [125]. This enables substantial elongation (>1000%) and strain-induced crystallinity (>30%) [100]. To overcome poor signal-to-noise and lack of carbon signals (cross polarization and magic-angle sample spinning) arising from the CNFs, proton signals from the mobile fraction of the thermoplastic elastomer are

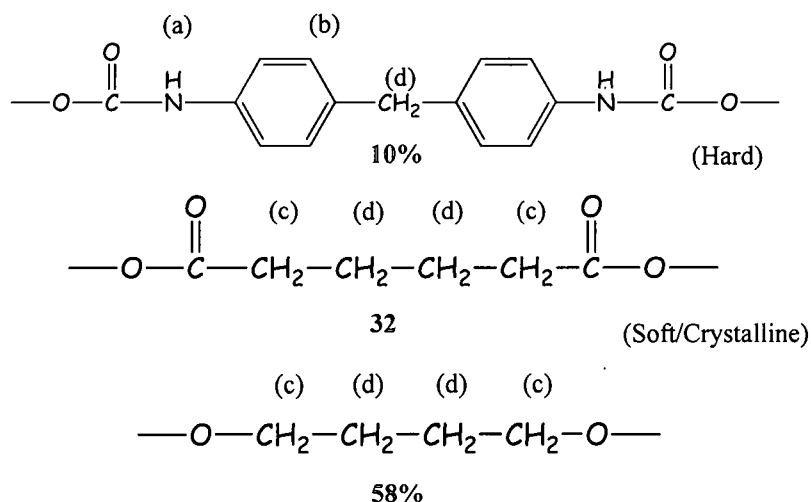
employed as an indirect measure of the interfacial structure. At room temperature, the mobile fraction is far above its glass transition temperature and can be directly observed in films with a good signal-to-noise ratio using a high-resolution NMR probe. Using this approach, the proximity of the CNFs to the mobile fraction, the effect of CNFs on the chain dynamics, and the size of rigid domains (crystallites or hard segment domains) as a function of CNF concentration and external strain are examined.

Experimental

Materials

Irogran PS455-203 (Scheme 5.1) is a high performance thermoplastic polyurethane elastomer purchased from Huntsman Polyurethane. NMR analysis in CDCl_3 shows that Irogran contains ~10% aromatic diisocyanate (hard segment), ~32% aliphatic and cyclo-aliphatic dicarboxylic acids and ~58% aliphatic diols (soft segments) [9]. Irogran has a density of 1.19 g/cm^3 , and differential scanning calorimetry (DSC) studies show T_g 's at -45°C and 135°C that can be assigned to the soft and hard segments. The melting temperature for the soft-segment crystallites is 48°C .

The CNFs used in these studies were heat-treated vapor-grown carbon nanofibers (PR-19-HHT) from Applied Science Incorporated with a density of 2.1 g/cm^3 . The average diameter and length of the CNF's were ~150 nm and greater than $10 \mu\text{m}$ as measured by a scanning electron microscopy. Chemical analysis shows that PR-19-HHT contains 99.9% carbon with hydrogen, nitrogen and iron levels below 0.1%, 0.1% and 0.024%, respectively.



Scheme 5.1: The structure and proton assignments for Irogran

Polymer Nanocomposite Fabrication

The TPE/CNF composites were prepared using a solution mixing process [102]. Solid pellets of Irogran were dissolved in tetrahydrofuran (THF) at ambient temperature ($\sim 25^\circ\text{C}$) for 4 hours with magnetic stirring. A CNF/THF mixture was prepared in a separate reaction vessel under shear for 4 hours using an Ultra Turrax IKA T18 Basic Stirring Machine operating at 14,000 rpm. This shearing process was used to break up any large clumps and evenly disperse the CNFs in the THF. Once evenly dispersed, the CNF/THF mixture was poured into the Irogran/THF mixture and allowed to mix for 24 hours to maximize dispersion of the nanofibers in the polymer matrix. The stirring container was open to the atmosphere and the majority of the THF solvent evaporated during this period. The remaining relatively viscous solution was poured into Teflon molds (102 mm x 26 mm), covered with aluminum foil and allowed to air dry overnight. The specimens were removed from the molds and placed in a vacuum oven for 24 hours

at 45°C to remove any excess THF. The dried composite samples were then stored in a dessicator at room temperature prior to measurement.

Deformation and Setting

The films for NMR experiments were as-cast samples ($\lambda=1.0$) or stretched to 60% ($\lambda=1.6$) or 1000% ($\lambda=11$). Samples at 60% strain were prepared using a TA Instruments dynamic mechanical analyzer (DMA Model 2980). Micro tensile specimens (8 mm (length) x 4 mm (width) x 0.5 mm (thickness)) were cut from sheets formed in the Teflon molds and placed in the DMA. The samples were stretched at 0.2 N/min to 60% strain at ambient temperature (25°C). The strain was removed and the sample was allowed to partially relax, and this deformed shape was used for NMR experiments. For the larger strain experiments, micro tensile samples of the same size were placed in a Tinius Olsen Universal Testing Machine (Model H10K-S UTM) and strained to 1000% at a rate of 2 mm/min at ambient temperature.

Solid State Proton NMR Experiments

Solid-state proton NMR spectra were acquired at 500 MHz using a Tecmag Apollo NMR spectrometer. Small samples of the films (1 mm x 5 mm) were placed in 4 mm NMR tubes that were inserted into 5 mm NMR tubes for acquisition of the proton NMR spectra using a high-resolution NMR probe. The spectra were acquired with a sweep width of 20 kHz using a 12 μ s 90° pulse. The chemical shifts were referenced to a lightly crosslinked sample of poly(dimethyl siloxane) at 0 ppm. The spectra of the samples were recorded in the same NMR tube directly after acquisition of the reference

samples to account for any differences in magnetic susceptibilities of the NMR tubes. The proton spin-lattice (T_1) and spin-spin (T_2) relaxation times were measured using the inversion recovery and Carr-Purcell Gill-Meiboom pulse sequences [126]. The domain sizes were measured by spin diffusion using the Goldman-Shen pulse sequence [127] with a delay time (τ_0) of 50 μ s to create a polarization gradient.

Results and Discussion

The Irogran/CNF nanocomposites are complex materials containing phase-separated polymer hard segments, amorphous soft segments above T_g , crystalline dicarboxylic acid and diol segments and CNFs. The morphology has been reported to change significantly as a function of temperature and external stress [9, 100]. We have studied these materials using solid-state proton NMR since our initial carbon NMR studies showed a low signal-to-noise ratio (not shown) for the polymer chains in close proximity to the CNFs. Proton NMR is not typically used to study the structure and dynamics of solid polymers because the line widths are much larger than the chemical shift dispersion for polymers below their glass transition temperatures. However, above T_g or with fast magic-angle sample spinning, relatively high resolution spectra can be obtained [18, 128-129]. The proton NMR spectra, line widths and relaxation times are sensitive to the molecular dynamics and the presence of paramagnetic atoms.

Figure 5.1 compares the 500 MHz proton NMR spectra of the Irogran dissolved in THF- d_8 and the as-cast film. The solution spectrum shows very narrow lines and a chemical shift dispersion from the different chemical groups shown in Scheme 5.1. The

proton spectrum of the film is not well resolved and shows a single broad peak with a full-width at half-maximum of ~ 2 kHz. We assign this signal to the mobile amorphous phase, since the peaks from crystalline soft segments and the aromatic hard segments are too broad to observe using high-resolution NMR. In the following experiments we use the signals from the mobile amorphous phase to indirectly measure the structure and dynamics of the polymer chains in close proximity to the CNFs.

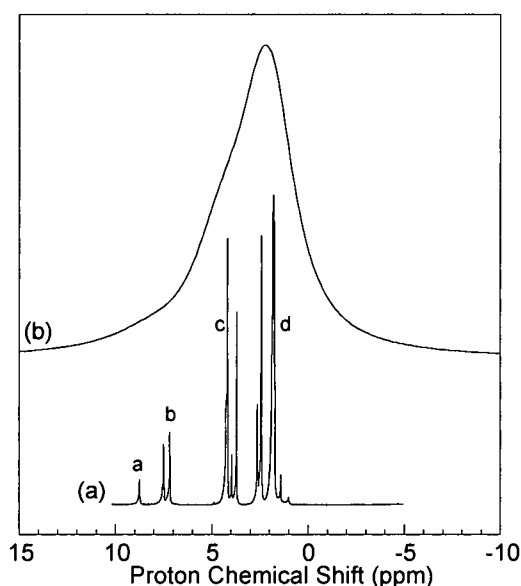


Figure 5.1: 500 MHz proton NMR spectra of (a) Irogran dissolved in THF- d_8 and (b) the as-cast film (See Scheme 5.1 for proton assignments).

Figure 5.2 shows the 500 MHz proton spectra of as-cast Irogran films containing 0, 1, 10, and 15 wt% CNFs. The addition of CNFs leads to a concentration-dependent broadening and shifting of the mobile amorphous phase peak (Table 5.1). The change in chemical shift could be attributed to ring current shifts from CNFs in close proximity to the soft segments or to magnetic susceptibility variations in the composites. The change in line width ($\Delta\nu_{1/2}$) could be attributed either to a slowing of chain motion or magnetic

susceptibility variations introduced with the CNFs. We can distinguish between these possibilities using relaxation experiments.

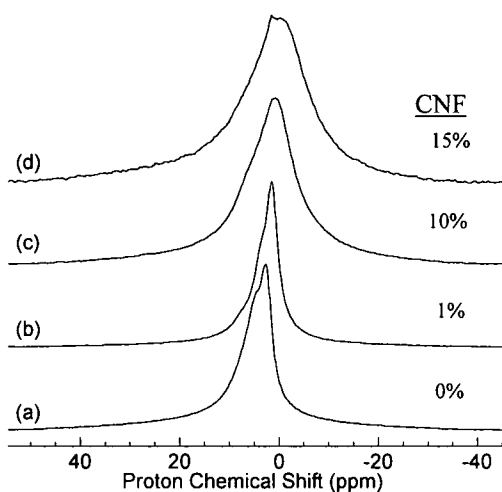


Figure 5.2: NMR line broadening spectra of (a) as-cast Irogran, with (b) 1 wt% CNF, (c) 10 wt% CNF and, (d) 15 wt% CNF

Table 5.1: Effect of CNF on the proton chemical shift (δ_H) and linewidths ($\Delta\nu_{1/2}$) for Irogran composites.

wt% CNF	δ_H (ppm)	$\Delta\nu_{1/2}$ (Hz)
0	2.1	1900
1	0.7	2100
10	0.1	5200
15	-1.8	5900

Figure 5.3 shows the effect of stretching on the proton NMR spectra of the mobile amorphous phase for Irogran and the 10 wt% CNF composite. Stretching to 60% (the onset point for stress-induced crystallinity) leads to only minor change in the spectra of

both the TPE and the composite, while a much larger stretching (1000%) leads to large upfield chemical shift changes for both samples, and additional line broadening for the TPE film. The difference in chemical shift resulting from the addition of 10 wt% CNF in the as-cast films shown in Figure 5.2 is no longer observable in the samples stretched to 1000% (Table 5.2). These data show that the local magnetic environment in the stretched samples is no longer sensitive to the presence of CNFs and demonstrates the mobile amorphous phase is no longer in close proximity to the CNFs.

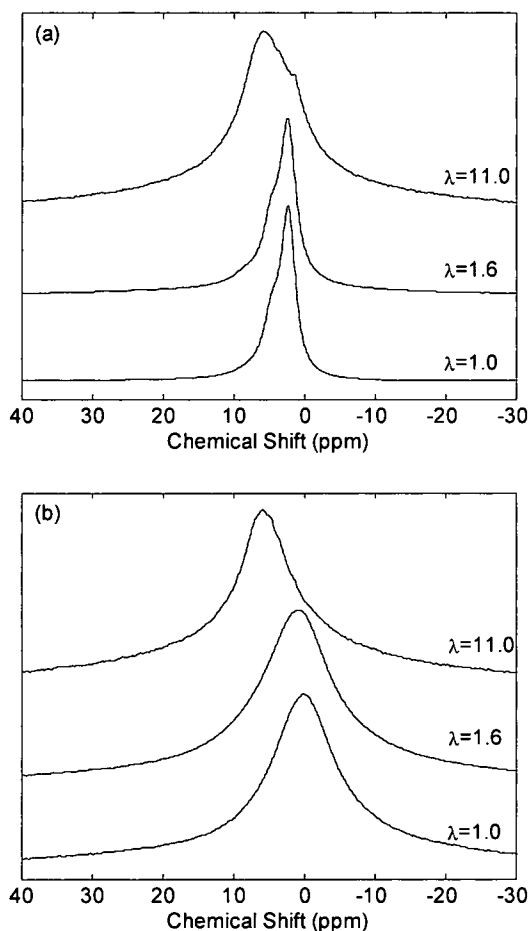


Figure 5.3: Comparison of the stretched and as-cast films
(a) without and (b) with 10 wt% CNF

The large change in line widths that accompany the addition of CNFs or stretching to 1000% could arise either from homogeneous or inhomogeneous line broadening. Homogeneous broadening occurs when the proton spin-spin relaxation time (T_2) increases as the molecular dynamics are restricted [130], and the relationship between the T_2 and the line width is given by:

$$\Delta\nu_{1/2} = \frac{1}{\pi T_2} \quad (1)$$

The most likely mechanisms for spin-lattice (T_1) and spin-spin (T_2) relaxation in these samples are dipolar and paramagnetic interactions [126, 131]. These contributions add to the relaxation rate and are given by:

$$\frac{1}{T_{1,2}} = \frac{1}{T_{1,2}^D} + \frac{1}{T_{1,2}^P} + \frac{1}{T_{1,2}^{other}} \quad (2)$$

where $\frac{1}{T_{1,2}^D}$, $\frac{1}{T_{1,2}^P}$, and $\frac{1}{T_{1,2}^{other}}$ denote the contributions from dipolar, paramagnetic and other possible mechanisms that contribute to the T_1 or T_2 relaxation times. The point to note for these discussions is that if paramagnetic interactions contribute to the relaxation, they will contribute both to T_1 and T_2 relaxation.

In order to study the sources of relaxation and determine the relative contributions of homogeneous and inhomogeneous line broadening to the line widths, we have measured the T_1 and T_2 relaxation times as a function of CNF concentration and stretching. These relaxation times, along with the homogeneous line widths calculated from the T_2 's ($\Delta\nu_{1/2}^{calc}$) are compiled in Table 5.2.

Table 5.2: Spin-lattice relaxation times (T_1), spin-spin relaxation times (T_2), chemical shifts (δ_H), and linewidths (observed and calculated) for stretched and as-cast Irogran and the 10 wt% CNF composite.

Parameter	Irogran			Irogran + 10% CNF		
	$\lambda=1.0$	$\lambda=1.6$	$\lambda=11$	$\lambda=1.0$	$\lambda=1.6$	$\lambda=11$
T_1 (s)	0.82	0.85	1.1	0.89	0.86	1.4
T_2 (ms)	0.40	0.80	0.17	0.30	0.56	0.25
δ_H (ppm)	0.9	1.2	5.9	0.1	0.7	5.9
$\Delta\nu_{1/2}^{obs}$ (Hz)	1650	1950	6100	5200	5700	6150
$\Delta\nu_{1/2}^{cals}$ (Hz)	796	398	1873	1061	568	1273

The T_1 's are usually not used to study the dynamics of polymers because magnetization can be efficiently transferred between protons at a rate faster than the spin-lattice rate, so the proton T_1 's are an average for the entire spin system. However, the presence of paramagnetics provides another relaxation pathway that can significantly decrease the polymer T_1 's in nanocomposites [119]. The T_1 's for the stretched and as-cast Irogran films and the nanocomposites are in the range of 0.8 to 1.4 s. Since the T_1 's do not significantly decrease with the addition of CNFs, these data demonstrates that paramagnetic impurities do not make a significant contribution to the proton relaxation, and that the broader lines observed for the CNF composites are not an artifact of residual catalyst used in the synthesis of the CNFs. These data are consistent with the low iron levels ($< 0.024\%$) measured by elemental analysis in the purified CNFs.

The T_2 's (Table 5.2) are sensitive to extreme stretching, but not to the presence of CNFs. The T_2 's for both the TPE and nanocomposites increase as the films are slightly

stretched ($\lambda=1.6$) but then decrease with extreme stretching. The increase in relaxation time with slight stretching is somewhat unexpected, since the stretched films are under stress and we would expect the chains on average to have reduced dynamics and shorter T_2 's [132].

The homogeneous line widths can be calculated from the T_2 's using Equation (1), and are listed in Table 5.2. These data shows that the observed line widths are much larger than the values calculated from the T_2 's. The chemical shift dispersion (Figure 5.1) from the different chemical environments along the chain (i.e., aromatic, aliphatic, etc.) partially explains the difference between the calculated and observed line widths, but does not explain the broader lines for the CNF composites.

X-ray scattering has shown that the TPE and CNF composites are phase separated into crystalline and amorphous domains, and several transitions, including the soft segment and hard-segment T_g 's at -45°C and 135°C and a melting transition at 48°C , are observed by DSC [100]. We have investigated the morphology in stretched and as-cast films using spin diffusion methods to characterize the mobile and rigid domains sizes. There are a number of pulse sequences that can be used to investigate the domain structure, including the three-pulse Goldman-Shen sequence used in these studies [127]. The spin diffusion pulse sequence creates a polarization gradient between the mobile and rigid phases, and we can calculate the domain sizes by monitoring the rate of magnetization exchange between them [133-134]. Figure 5.4 shows a plot of the mobile phase peak intensity as a function of spin diffusion time after creation of the polarization

gradient for TPE and the 10 wt% composite in the as-cast and slightly stretched ($\lambda=1.6$) films. The feature to note about Figure 5.4 is that the spin diffusion data is sensitive to slight stretching, even though stretching to $\lambda=1.6$ has been shown by x-ray scattering to lead to a barely measurable increase in the crystallinity [100].

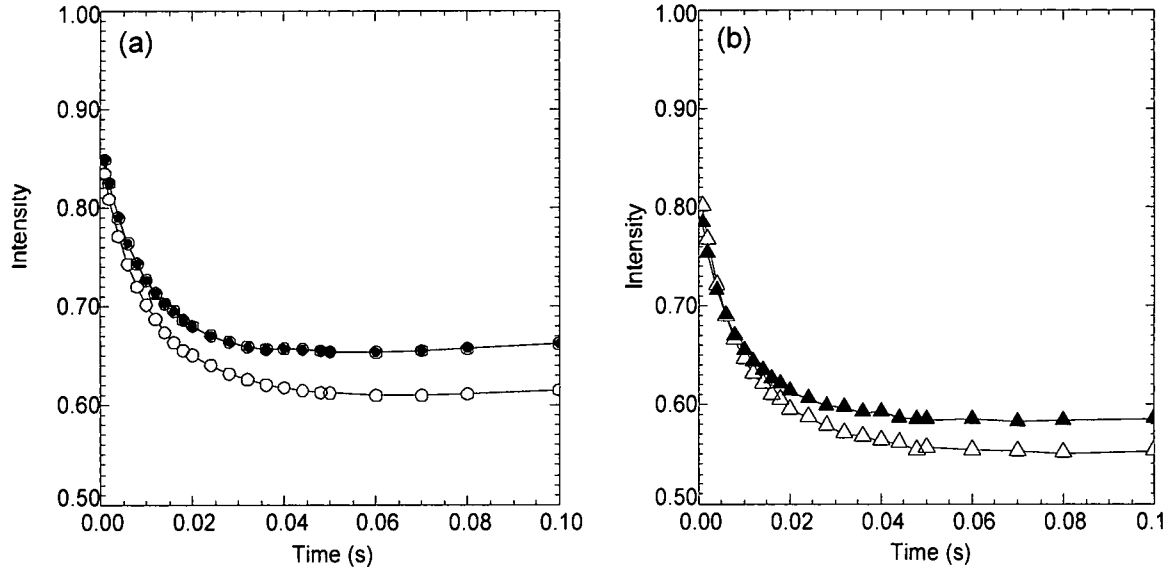


Figure 5.4: Magnetization exchange curves for as-cast (filled symbols) and stretched to $\lambda=1.6$ (open symbols) samples of (a) TPE films and (b) 10% TPE/CNF composites.

Proton spin diffusion has been extensively used to study the morphology of polymers because the rates of spin diffusion are sensitive to domain sizes on the order of 1-20 nm that are difficult to study by other means. The length scale of spin diffusion (L) depends on the surface-to-volume ratio and for a two-phase model is given by [134]:

$$L = \frac{4\sqrt{t_{sd}}\sqrt{D_A D_B}(\rho_A^H f_A + \rho_B^H f_B)}{f_A f_B \sqrt{\pi}(\rho_A^H \sqrt{D_A} + \rho_B^H \sqrt{D_B})} \quad (3)$$

where D_A and D_B are the spin diffusion coefficients for the mobile and immobile phases, ρ_A and ρ_B are the proton densities, f_A and f_B are the volume fractions, and $\sqrt{t_{sd}}$ is measured experimentally. This length scale is converted into the domain size (d) and the long period (d_p), or the distance between domains, by assuming a morphological model [133-134]. The experimental value for $\sqrt{t_{sd}}$ can be determined from the initial rate of spin diffusion, as shown in Figure 5.5 for the as-cast film. The values for $\sqrt{t_{sd}}$ for the stretched and as-cast films and composites are listed in Table 5.3, along with the parameters used to calculate the domain sizes.

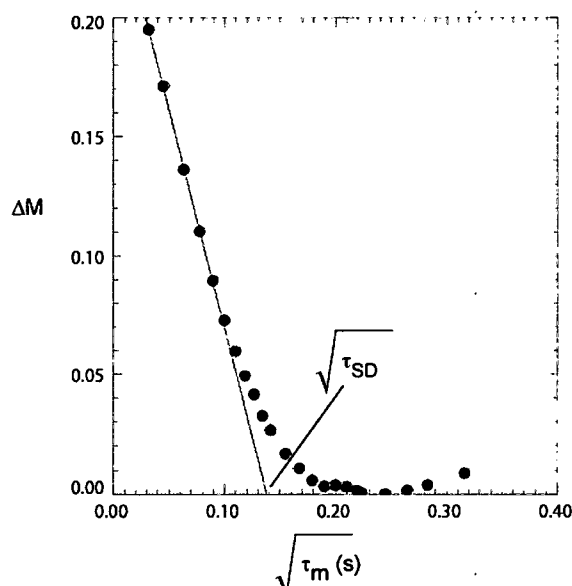


Figure 5.5: A spin diffusion plot for the as-cast TPE film sample.

Converting the measured values for $\sqrt{t_{sd}}$ into domain sizes requires several parameters that may be estimated from the chemical structure or the relaxation times. The proton densities are estimated from the chemical structures and the density of Irogran, while the spin diffusion coefficients for mobile polymers are empirically related

to the spin-spin relaxation times [135]. The spin diffusion coefficients for the rigid phase are assumed to be in the range of those reported for poly(styrene) and poly(methyl methacrylate) ($0.8 \text{ nm}^2/\text{ms}$) [133]. The volume fractions for the mobile and immobile phase are estimated from the chemical structure (Figure 5.1) and x-ray scattering data. The x-ray and DSC data show that the slightly stretched samples ($\lambda=1.6$) have a crystallinity index of 1-3%. The immobile phase in these samples primarily results from self-association of the aromatic rings that are present at the 10% level. The x-ray scattering at high draw ratios ($\lambda=11$) shows the formation of a lamellar morphology with a relatively high crystallinity index (40-50%) [100]. Given these data we have modeled the spin diffusion data using a three dimensional spherical model at low draw ratios and a one dimensional lamellar model at high draw ratios.

The results of the spin diffusion experiments listed in Table 5.3 show that the spin diffusion distance (L), the domain sizes (d) and spacings between domains (d_p) depend strongly on the draw ratio but not on the presence of CNFs. At low draw ratios the domain sizes are on the order of 12-13 nm and the spacings between domains are in the range of 20-21 nm. High draw ratios lead to both smaller domain sizes (6-8 nm) and smaller spacings (12-14 nm). The domain spacings are in good agreement with those measured by x-ray scattering [9, 100].

Table 5.3: Spin diffusion times and domain sizes for Irogran films and the 10 wt% CNF composites

Sample	State	f^a	D_{soft}^b (nm ² /ms)	$\sqrt{t_{sd}} (s^{1/2})$	L (nm) ^c	ε^d	d (nm) ^e	d_{lp} (nm) ^f
Irogran	$\lambda=1.0$	0.16	0.37	0.138	25.6	3	12.7	20.9
	$\lambda=1.6$	0.16	0.31	0.147	26.7	3	12.9	21.1
	$\lambda=11$	0.51	0.51	0.120	14.1	1	8.2	14.1
Irogran/ 10% CNF	$\lambda=1.0$	0.19	0.40	0.136	23.6	3	13.3	20.7
	$\lambda=1.6$	0.19	0.33	0.139	22.5	3	12.9	20.0
	$\lambda=11$	0.51	0.43	0.110	11.9	1	6.1	11.9

^a The hard segment fraction is the sum of the crystallinity determined by x-ray and the fraction of aromatic hard segments ($f = 0.1$).

^b D_a is the spin diffusion coefficient for the mobile amorphous phase determined from the spin-spin relaxation time. The diffusion coefficient for the rigid phase was taken as 0.8 nm²/ms.

^c The length scale of spin diffusion given by Equation (3).

^d The dimensionality of the system. Spin diffusion was modeled as randomly distributed spheres ($\varepsilon = 3$) at low crystallinity where the hard segments are comprised mainly of self-associating hard segments. At high crystallinity x-ray studies show a lamellar morphology ($\varepsilon = 1$).

^e The domain sizes are given by $d = f_a L$ for $\varepsilon = 1$ and $d = 3f_a L$ for $\varepsilon = 3$.

^f The spacing between crystallites is given by $d_{lp} = L$ for $\varepsilon = 1$ and $d_{lp} = 2.683(f_a)^{2/3} L$ for $\varepsilon = 3$.

Conclusion

The shape-memory thermoplastic polyurethane with 10% hard segments (Irogran) filled with CNFs have been studied using high-resolution solid-state proton NMR. Previous studies showed that Irogran has a complex morphology [9, 100] and the incorporation of nanofibers further increased this complexity. The proton NMR signals from the mobile component in these films can be easily detected using high-resolution

NMR methods because molecular motion in the mobile component averages the proton line widths from 50 kHz to 1-2 kHz. This allows us to monitor the polymer dynamics as CNFs are added and to measure the domain sizes using proton spin diffusion.

The addition of CNFs to Irogran leads to concentration-dependent changes in the chemical shifts and line widths of the mobile phase. The relaxation times are not sensitive to the presence of CNF's, demonstrating that the broadening is inhomogeneous. We believe that the broadening and shifting is a consequence of the difference in magnetic susceptibility between the CNFs and the mobile polymer domains. This observation explains in part why it is difficult to directly observe the carbon spectra using cross polarization and magic-angle sample spinning in the presence of CNFs.

The stretching of Irogran and the 10 wt% CNF composites to 60% does not have a large effect on the molecular dynamics of the mobile domains or the crystallinity. We can observe differences in the spin diffusion curves at low draw ratios, suggesting that the NMR is extremely sensitive to the onset of stress-induced crystallization. Highly stretched samples ($\lambda=11$) show significant differences in the chemical shifts, relaxation times and domain sizes when compared to the slightly stretched samples. The similar chemical shifts for the highly drawn samples with and without CNFs suggest that the mobile phase is no longer in close proximity to the CNFs. These data support a model in which nucleation is promoted at the surface of the CNFs, thereby separating the mobile amorphous phase from the CNFs. Extreme stretching also increases the crystallinity and decreases the average domain sizes. The values for the spacing between domains

measured by NMR are in good agreement with the values reported by x-ray scattering [9, 100].

In summary, we have used high-resolution solid-state proton NMR to probe the mobile amorphous phase in Irogran and its composites with CNF's. The results show that the signals are broadened in the vicinity of the CNF's due to a difference in magnetic susceptibility between the CNF's and the polymer, but the molecular dynamics are not greatly changed. Spin diffusion appears to be very sensitive to the onset of stress-induced crystallinity, and stretching to high draw ratios promotes crystallite formation on the surface of the CNF's and leads to a higher crystallinity and smaller crystallites.

CHAPTER VI

IMPACT OF CARBON NANOFIBERS ON THE LOCKING MECHANISM FOR A SHAPE MEMORY THERMOSET EPOXY

In the last two chapters, the primary focus was on how carbon nanofibers (CNFs) influenced the shape memory properties in a lightly crosslinked (<10%) thermoplastic polyurethane elastomer (Irogran) polymer system. In this chapter, we will focus on how CNFs effect the shape memory properties in a highly crosslinked thermoset epoxy (TEMBOTM DP5.1) polymer system. This shape memory polymer (SMP) system uses the glass transition temperature (T_g) to lock in the deformation and recovery. What we hope to show is that a strong interaction between the nanoparticle filler and the polymer matrix are important for improving both the shape memory properties and recovery time in these unique SMPs.

The shape memory effect in thermally-activated, highly cross linked polymer systems is also entropic in nature [136]. Because it contains chemical crosslinks, this type of SMP uses vitrification through the T_g to lock in the deformation. During uniaxial deformation above the T_g , the polymer chains can undergo conformational and rotational changes that permit the polymer chains to be strained. The alignment of these polymer chains during deformation increases thereby increasing the stored energy in the material as the configurational entropy of the chain decreases. To lock in this new temporary

shape and stored energy, the temperature is rapidly cooled below the T_g and vitrification will restrict the polymer chains from freely rotating. If the constraints are removed and the polymer is reheated back above T_g there is an increase of entropy which serves as the driving force for the material to return back to its original shape [2].

In the 1980's, shape memory polymers (SMPs) were rediscovered by Hayashi and coworkers [137] when they developed a crosslinked polyethylene that utilized the glass transition temperature (T_g) as the switching mechanism. The vast majority of SMPs at that time were thermoplastic because they could be easily deformed. The mechanism for locking in the deformation occurred through a transition temperature that was either a melting temperature (T_m) or a glass transition temperature (T_g). Within the last few years there has been a growing interest in thermoset epoxy SMPs for aerospace applications because they are light weight, strong, and stiff [106, 138-140]. Even though they do not deform as much as thermoplastic polymers, they still have the ability to lock in deformation and recovery upon the application of heat. The mechanism for locking in the deformation for thermoset epoxy SMPs occurs only by vitrification through the glass transition temperature. Since they are highly crosslinked, they do not form crystallites like the thermoplastic polymers.

Epoxy resins were first discovered in the late 1930's by Pierre Castan in Switzerland and Sylvan Greenlee in the United States [141-142]. They are usually characterized as having an oxirane ring which can be reacted with curing agents to form a highly crosslinked polymeric structure. The vast majority of these resins are

manufactured by reacting epichlorohydrin and bis(4-hydroxy-phenyl) dimethylmethane (commonly called bisphenol A) in the presence of an aqueous caustic soda. Since their commercial introduction into the United States in the late 1940's, epoxy resins have gained considerable attention as high performance coatings, adhesives, and reinforced plastics [143]. Additional properties include high chemical resistance, low shrinkage, heat resistance, and very good electrical properties which have made them successful in the commercial market. Epoxy reactions usually involve the addition of an amino acid across an epoxy ring. Figure 6.1 shows the reaction of an active hydrogen atom added across the epoxy ring. The secondary hydroxyl group that forms from this reaction provides excellent adhesive properties along the molecular chain.

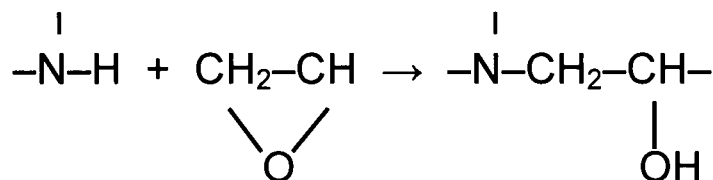


Figure 6.1: Amino hydrogen atom added across an epoxy ring

Traditional fillers have been added to polymer systems to increase the stiffness and recoverable force levels. Within the last decade the focus has been on nanoparticle reinforced composites because lower volume fractions (3-5%) are required compared to conventional fillers such as talc or mica [8-9, 89-93, 100, 105-106]. These lower volume fractions reduce weight, costs and processing problems. As the percentage of reinforcement increases, the modulus and recoverable force increase while the ductility

and recoverable strain decrease [73-74]. This tradeoff in properties allows tailoring of a SMP for specific engineering application requirements.

In this study, a series of thermoset epoxies filled with vapor grown carbon nanofibers were characterized. The main purpose of this study is to provide a more thorough understanding of the thermo-mechanical storage and recovery behavior in thermoset epoxy SMP under relevant deformation conditions. By understanding how CNFs influence shape memory properties (i.e., shape fixity, shape recovery and recovery time) we might be able to tailor these materials to perform specific tasks. In the experimental section we will discuss tools and methods used to analyze and evaluate these nanocomposite materials with shape memory properties. The results and discussion section will provide information on the mechanical properties (i.e., T_g , E , etc.) and shape memory properties for this thermoset epoxy SMP filled with CNFs. By comparing this data to previous work, we may be able to determine what the driving force is for this shape memory process. The paper will end with a brief conclusion of what we have observed.

Experimental

Materials and Specimen Preparation

The SMP used in this study was a fully cured and crosslinked thermoset epoxy resin called TEMBOTM DP5.1. The nanocomposite material was formulated and manufactured by Composite Technology Development (CTD). Chemical and processing details of the material are proprietary, but the material can essentially be considered as a

two-part thermoset epoxy network. The thermoset epoxy structure was fabricated using traditional composite fabrication methods and behaved the same as other nanocomposite structures while below its glass transition temperature (e.g., stiffness and strength are predictable). This shape memory thermoset epoxy nanocomposite from CTD differs from traditional composites in its ability to “lock-in” high levels of deformation (i.e., 20-30% strain) without damage, and recover this “frozen” strain upon subsequent heating. If it is heated above its glass transition temperature, the polymer matrix becomes compliant and capable of handling a large amount of recoverable strain without degradation [138-139]. Once cooled, the material becomes rigid again and naturally holds or “freezes” its new temporary shape almost indefinitely. When heated back above the glass transition temperature, the material elastically returns to its original “remembered” shape.

The filler used to make these nanocomposite samples was a pyrolytically stripped low density (PSLD) heat treated carbon nanofiber (PR-19-XT-PSLD) from Applied Science Incorporated (ASI). Since they are produced in a vapor phase, they generally become entangled during growth yielding a mesh-like appearance. This raw form is then processed using a debulking method (designated as XT in the product code) to create a loose structure that will allow the CNFs to be more easily dispersed. According to ASI, these CNFs have an approximate density of 2.1 g/cm^3 and chemical analysis revealed that they are 99.9% pure [101]. Using scanning electron microscopy (SEM) we were able to determine that the average diameter was $\sim 150 \text{ nm}$ with a length greater than $10 \text{ }\mu\text{m}$. The CNF has a tubular structure with sidewalls composed of angled graphite sheets that give it a “stacked” or “herringbone” appearance. These exposed edge planes along the entire

surface of the fiber are highly reactive and provide additional opportunities for bonding or functionalization.

Morphology

The fracture topography and dispersion of CNFs were studied using a scanning electron microscope (SEM) Model FEI Sirion/XL30. Composite specimens were fractured in liquid nitrogen and adhered to metal tabs using silver paint. The surface of the fractured material was lightly coated with carbon using an Edwards Auto 306 Turbo Evaporator to enhance the appearance of the CNFs and prevent the effects of charging.

Thermal Characterization

The glass transition temperature was studied using a differential scanning calorimeter (DSC) purged with nitrogen in a cooling and heating process (TA Instruments Model Q 1000). The temperature corresponding to the mid-point in heat capacity was used to determine the glass transition temperature (T_g) of the polymers. Sample weights of 10-15 mg were used with a heating rate of 10 °C/min. In addition, modulated DSC was also conducted to see if there was a difference between reversible heat flow and non-reversible heat flow.

Thermogravimetric analysis (TGA) was carried out on a TA Instruments Model Q 5000 IR under both nitrogen and air at a heating rate of 10 °C/min. Initial sample weights of 10-15 mg were used. The decomposition temperature (T_{dec}) was taken to be

the temperature at which 5% mass loss had occurred. The residual char mass percentage (m_{ch}) was taken as the mass percentage remaining at $T = 850\text{ }^{\circ}\text{C}$.

Thermomechanical Characterization

The Young's modulus (E) and glass transition temperature were studied using a dynamic mechanical analyzer (DMA) in tensile mode (TA Instruments Model 2980). Micro tensile specimens (8 mm (l) x 4 mm (w) x 0.5 mm (t)) were placed in the fiber film clamps of the DMA with an initial force of 0.001 N. A temperature ramp method from -145°C to $+145^{\circ}\text{C}$ with a heating rate of $4^{\circ}\text{C}/\text{min}$ was used for both parameters at a fixed mechanical oscillation frequency of 1 Hz. For consistent comparison between tests, the glass transition temperature (T_g) was taken to be the peak of the tan-delta curve.

The glass transition temperature was studied using a thermomechanical analyzer (TMA) in penetration mode (TA Instruments Model 2940). A temperature ramp method from -145°C to $+145^{\circ}\text{C}$ with a heating rate of $4^{\circ}\text{C}/\text{min}$ with nitrogen purge was used. An initial force of 0.1 N was applied to the sample.

Shape Recovery and Recovery Time Characterization

Thermo-mechanical analysis was conducted using a DMA (TA Instruments Model 2980) in controlled force mode on a series of Epoxy/CNF samples. The main reason for performing these tests was to study the shape memory properties (shape fixity, shape recovery and recover time) and determine if the addition of CNFs had an impact on the strain set mechanism. A 3-dimensional illustration of a typical shape memory cycle

is shown in Figure 6.2. Micro tensile specimens (8 mm (l) x 4 mm (w) x 0.5 mm (t)) were cut from sheets provided by CTD and placed in the DMA. The samples were heated to 85°C (10-15°C above the glass transition temperature) for 30 minutes and then stretched at 0.2 N/min to 20% strain and held constant. The temperature was rapidly decreased at ~30°C/min to ambient temperature (25°C) to help lock in the strain. Vittrification or “freezing” of the polymer chains in this low temperature glassy state was the key to locking in this new temporary shape. After 30 minutes, the strain was removed and the sample was allowed to relax. This relaxed or “set” strain was used to calculate the shape fixity. After 30 minutes, the temperature was rapidly increased back up to 85°C to recover the original shape. This final step was used to measure the shape recovery and recovery time of the nanocomposite samples.

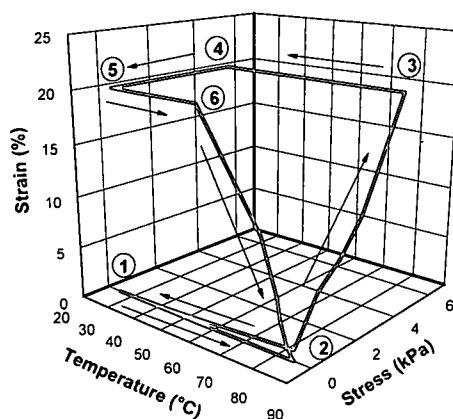


Figure 6.2: 3D plot of stress vs. strain vs. temperature for a shape recovery experiment via vitrification through T_g

Figure 6.3 is a typical DMA plot showing which strain values were used to calculate the shape fixity, percent recovery and the recovery time for the shape recovery

experiment. A thin film sample was placed in the clamps of the DMA at room temperature with an applied force of 0.001N (point A). The sample was then heated at a rate of 3°C/min to a deformation temperature (T_d) of 85°C (point B). This temperature was approximately 10-15°C above the glass transition temperature ($T_g \sim 71^\circ\text{C}$) for this thermoset epoxy. The film was then stretched to a maximum strain (ϵ_{\max}) of 20% at this temperature (point C) and then quickly cooled down to a setting temperature (T_s) under constrained conditions of constant length (point D). For this test method, ambient temperature (25°C) was chosen as the setting temperature because it was well below the glass transition temperature. When the external force was withdrawn, a slight contraction occurred and the strain changed from the maximum strain (ϵ_{\max}) to a set strain (ϵ_{set}). This set strain (ϵ_{set}) was referred to as the fixed strain, which meant that the film specimen moved from point D to point E. The specimen at point E was then used for studying the shape recovery behavior in a process of constant heating rate. The recovered strain (ϵ_{rec}) after heating is referred to as the residual strain or permanent deformation (point F).

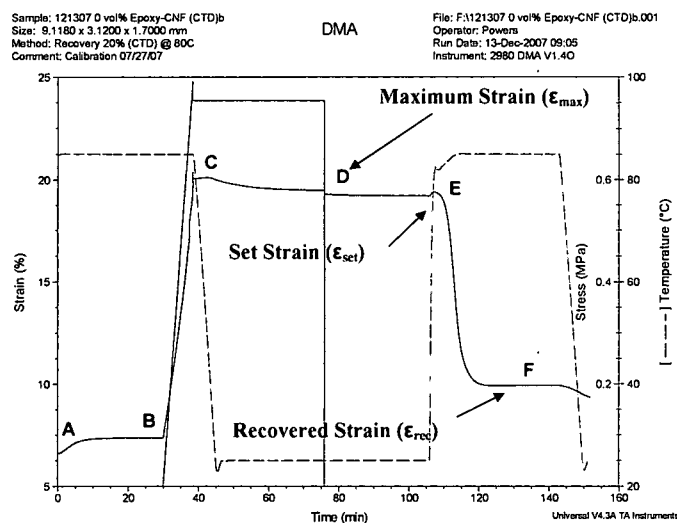


Figure 6.3: DMA plot of a shape recovery experiment for a neat epoxy

Lendlein et al. [2] have determined that the shape fixity and percent recovery are the two main properties that help determine how effective the shape memory effect is in the polymer system. Shape fixity is the ability to lock in the strain deformation and hold it until the external stimulus is applied. To be an effective shape memory material, when the force is released it should hold and maintain this new temporary shape indefinitely. Both the set strain (ϵ_{set}) and the maximum strain (ϵ_{max}) are used to determine the percent shape fixity from the following ratio:

$$\% \text{ shape fixity} = (\epsilon_{\text{set}}/\epsilon_{\text{max}}) \times 100 \quad (6.1)$$

The other important property is percent shape recovery and this refers to the ability of the material to return back to its original shape when the external stimulus is applied. This value is calculated from the maximum strain (ϵ_{max}) minus the recovered or permanent deformation strain (ϵ_{rec}) divided by the maximum strain (ϵ_{max}):

$$\% \text{ shape recovery} = ([\epsilon_{\text{max}} - \epsilon_{\text{rec}}]/\epsilon_{\text{max}}) \times 100 \quad (6.2)$$

Both of these parameters along with the recovery times will be investigated in this thermoset epoxy SMP filled with CNFs. We want to understand the impact of these nanoparticle fillers on the locking mechanism for a SMP that uses vitrification through the glass transition temperature (T_g).

Results and Discussion

One of the criteria for improving shape memory characteristics with nanofiller loading is good dispersion. Figures 6.4 and 6.5 are SEM micrograph images of the cryogenically fractured surface of the SMP thermoset epoxy nanocomposite sample. The general topography of the fracture surface of the composite is the epoxy matrix mixed with the CNFs. For the most part, there is good dispersion of the CNFs throughout the polymer matrix with a few aggregates found (approximately 10% of area examined) with higher CNF loadings (3 vol%).

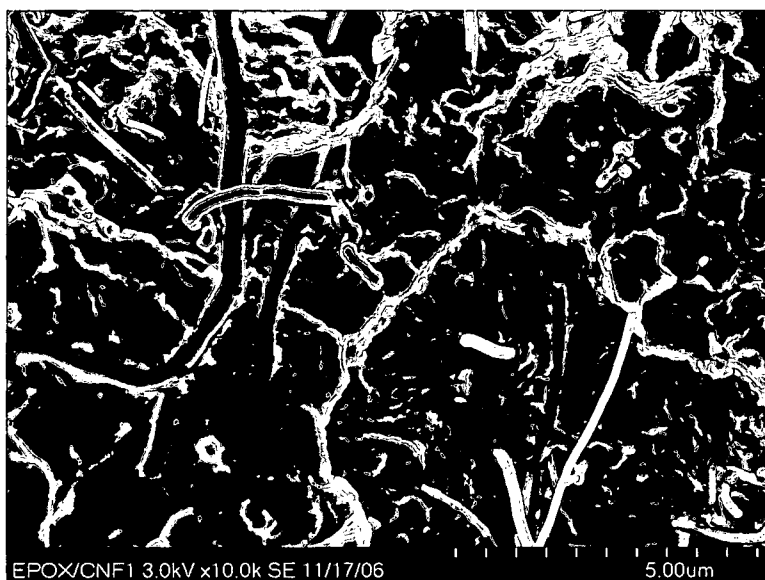


Figure 6.4: SEM scan of a 1 vol% Epoxy/CNF showing good dispersion of CNFs but poor adhesion of CNFs to polymer matrix

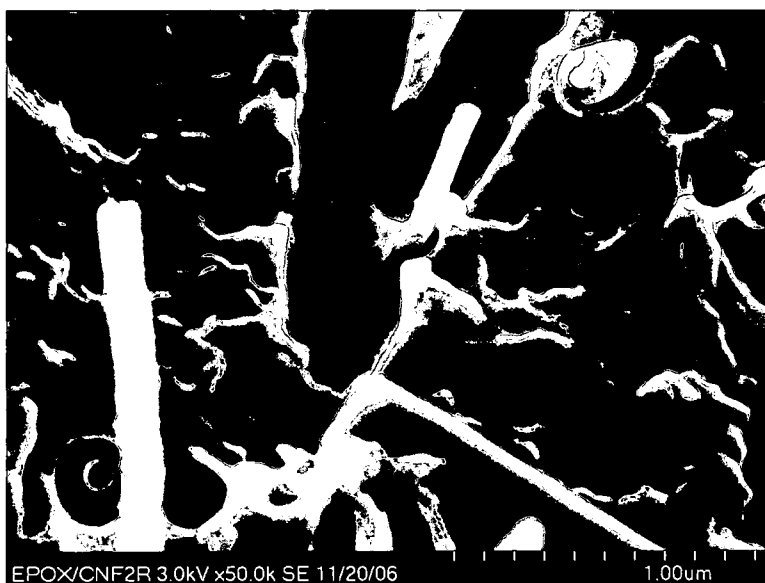


Figure 6.5: Closer magnification shows a gap around the CNF

The other criteria for improving shape memory characteristics with nanofiller loading is a strong interfacial interaction between the filler and the polymer. Both of the SEM images above indicate that there does not appear to be good adhesion between the polymer matrix and the CNFs. The images show a gap surrounding the CNFs and poor fiber pull out which would indicate poor wettability between the fiber and the polymer matrix.

In addition, if there was a strong interaction between the CNFs and the polymer matrix this property should be reflected in the glass transition temperature. Figure 6.6 shows a plot of temperature versus volume fraction of CNF using DMA, DSC, modulated DSC, and TMA. The trend lines from all of these plots indicate that there is a distinct decrease in the glass transition temperature with CNF loading. We suspect that the CNFs

could be inhibiting the extent of crosslinking or altering the topology of the network leading to a lower glass transition temperature.

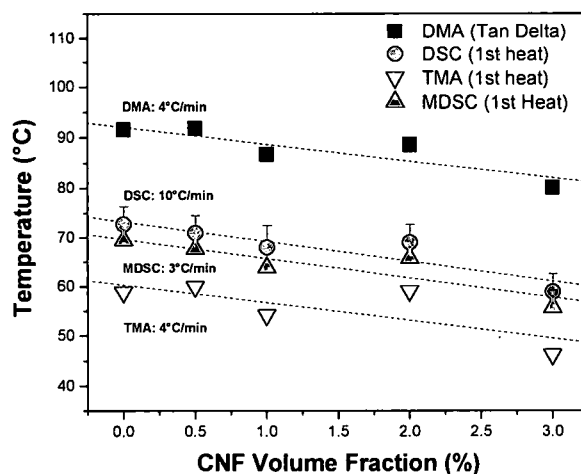


Figure 6.6: Effects of CNF loading on glass transition temperature (T_g)

The Young's modulus (E) or modulus of elasticity is a measure of the material stiffness. When filler is added to the polymer matrix, it can have a substantial impact on the rubbery modulus. This is usually true when the modulus of the filler is several orders of magnitude larger than the modulus of the polymer matrix. Even though the modulus of the CNF is larger than the thermoset epoxy, it does not appear to impact the overall storage modulus of the nanocomposite material. Figure 6.7 is a plot of the storage modulus versus CNF loading at different temperatures. We can see from this plot that the storage modulus is higher for the lower temperatures and decreases with higher temperatures. This is expected, but we would also expect to see the modulus increase with CNF loading at each specific temperature. There is a slight increase with CNF

loading at the lower temperatures, but not enough to justify adding CNFs to help improve the polymer stiffness. We suspect that this slight increase is due to the modulus of the thermoset epoxy is approaching that of the CNFs. The data values at 75°C, which are near the glass transition temperature, show the trend leveling off and slightly decreasing with CNF loading.

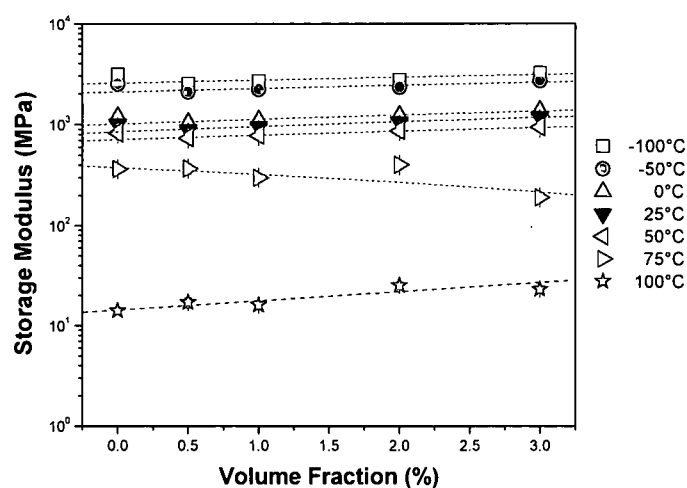


Figure 6.7: Effects of temperature on storage modulus (E')

Figure 6.8 is a plot of the normalized storage modulus (E/E_0) versus CNF loading at different temperatures. From this plot we can see that the modulus or stiffness of the nanocomposite was not impacted with CNF loading, independent of temperature. There is a slight increase with CNF loading, but not several orders of magnitude higher. In addition, the values at 75°C show a slight decrease with loading and the values at 100°C show a slightly larger increase. Again, these increases do not justify adding fillers since the stiffness did not increase substantially.

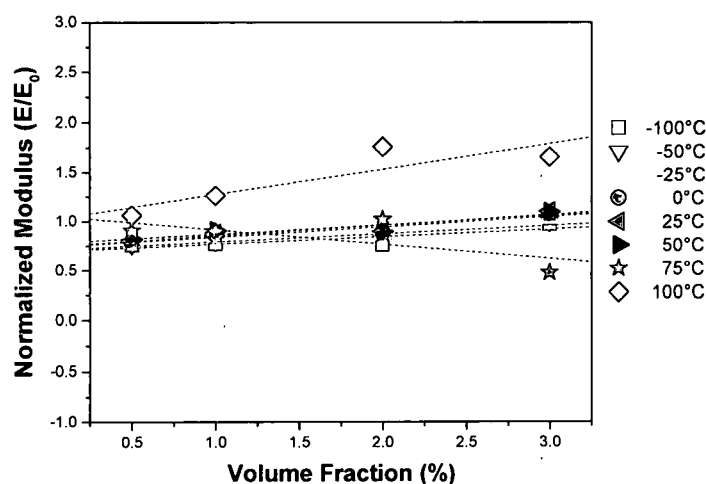


Figure 6.8: Effects of CNF loading on normalized storage modulus (E/E_0).

Figure 6.9 is a plot of percent shape fixity versus CNF loading. Even though we have excellent shape fixity ($\sim 97\%$) for this thermoset epoxy SMP, the values remain relatively constant with increasing CNF loading. If there was an interaction between the CNFs and the polymer matrix, we would expect to see this value to either increase or decrease with CNF loading. Since there was no change, we suspect that the CNFs did not have an impact on the locking mechanism for this particular SMP.

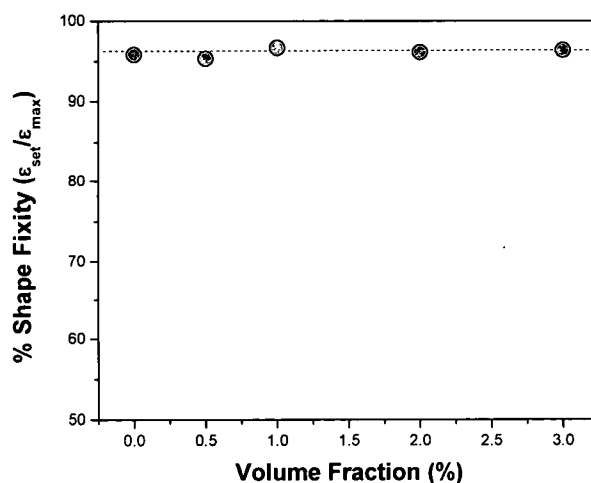


Figure 6.9: Effect of CNF loading on shape fixity.

Figure 6.10 is a plot of percent shape recovery versus CNF loading. For this thermoset epoxy SMP we have relatively good shape recovery (~76%) and the values remain relatively constant with increasing CNF loading. If there was an interaction between the CNFs and the polymer matrix, we would also expect to see this value change with CNF loading. Since there was no change, we suspect that the CNFs did not have an impact on the locking mechanism for this particular SMP. It should be noted that the large error bars could be attributed to the samples slipping in the DMA clamps due to thermal contractions of the polymer matrix.

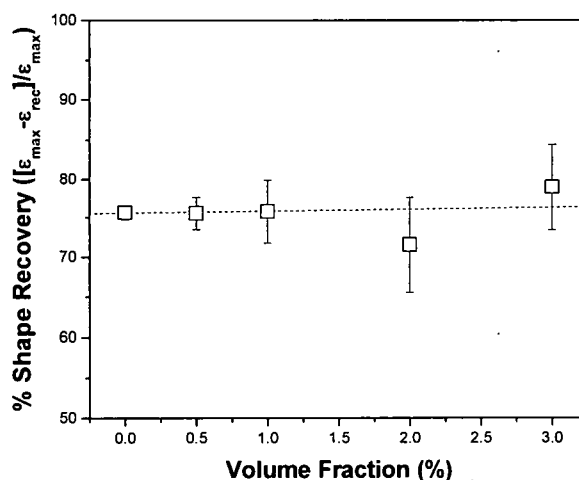


Figure 6.10: Effect of CNF loading on percent shape recovery

The strain recovery or relaxation time was taken from the set strain (ϵ_{set}) to the recovered strain (ϵ_{rec}). Initially, the strain was removed and the specimen was allowed to equilibrate before applying heat. A temperature ramp of $\sim 30^{\circ}\text{C}/\text{min}$ was used to heat the thermoset epoxy SMP nanocomposite above the glass transition temperature and allow the material to return back to its original or near original shape. A non-linear least squares fit (NLSF) analysis software package (Origin 7.5) was used to measure how fast the material recovered. Figure 6.11 shows a typical DMA scan of a 2 vol% CNF sample from point E to point F with a trend line calculated using the NLSF equation. From this equation, the recovery or relaxation time (t_1) was calculated using a second order exponential decay.

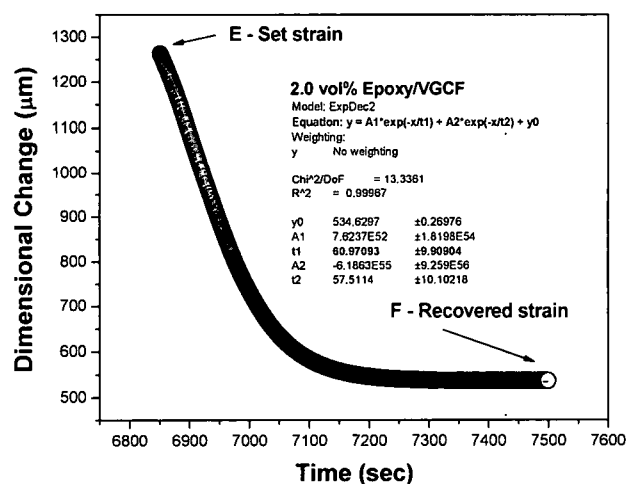


Figure 6.11: Non-linear least square fit used to calculate shape recovery time

Figure 6.12 is a plot of recovery time versus CNF loading. We can see from this plot a slight decrease in recovery time with CNF loading; however, it is not recovering fast enough to justify adding nanoparticle fillers. One possible explanation would be strain enhancement near the CNFs during deformation. So to accommodate this volume change, the strain that was originally in the CNF is now transferred to the region near the fiber. Higher strain near the CNFs results in the chains being stretched more thereby yielding more strain energy stored in the polymer chains. Another possible explanation could be due to the CNFs acting as a diluent during processing. This would prevent the thermoset epoxy SMP from fully curing. Since the nanocomposite is not completely crosslinked, this would allow more polymer chains to stretch and recover faster.

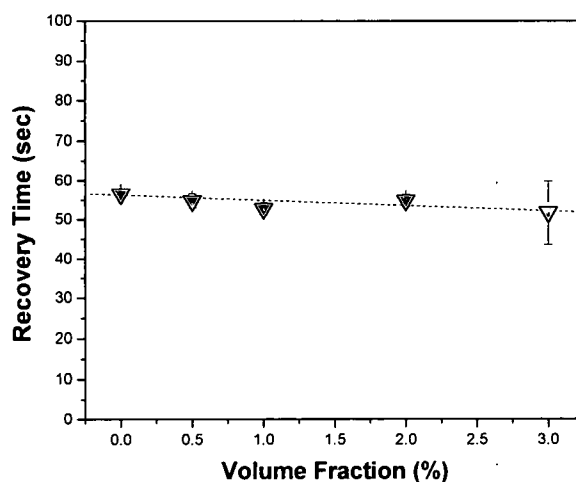


Figure 6.12: Effect of CNF loading on shape recovery time

Conclusions

Previous studies of carbon nanotube (CNT) reinforced polymer matrix composites have shown a substantial increase in the composite modulus over the matrix modulus [144]. Schadler et al. [145] discovered about a 40% increase in the effective modulus or stiffness of a CNT reinforced epoxy as compared to the matrix value with only 5 wt% CNTs. Qian et al. [105] also found an increase in the effective modulus of CNT reinforced polystyrene to be on the order of 40% for just 1 wt% CNTs. Zhu et al. [146] observed the stress-strain response of functionalized CNTs in epoxy and found an increase in the effective properties on the order of 30–70% at 1 and 4 wt% CNTs.

For this thermoset epoxy shape memory polymer system we did not see a dramatic increase in any of the properties with CNF loading. The SEM images showed poor interaction between the polymer matrix and the CNFs. From these images we could

see that there is a void in the polymer matrix near the CNF which was probably due to phase separation within the two component system. If there was a strong interaction between the polymer matrix and the CNFs this would have been reflected in the glass transition temperature. DSC, DMA and TMA results showed a large decrease with CNF loading. It was speculated that the CNFs prevented crosslinking from occurring during the curing process thereby decreasing the stiffness of the nanocomposite. DMA results showed very little enhancement in the storage modulus with CNF loading at different temperatures. Results near the T_g actually decreased with CNF loading. The only increase occurred at 100°C which was well above the glass transition temperature. When the data was normalized (E/E_0) there was only a slight increase with CNF loading. Again, only the data 100°C showed a slight improvement with CNF loading.

Schaefer and Ryan [147] used small-angle x-ray and light scattering on elastomeric, thermoplastic and thermoset composites loaded with a variety of nanoscale reinforcing fillers such as silica, carbon nanotubes (single-walled and multi-walled), carbon nanofibers, and layered silicates. Using the Witten, Rubinstein and Colby model they were able to provide insight into reinforcement by fractal aggregates. When nanoparticles were added to hard materials such as thermosets, they were ineffective at reinforcing because the modulus of the filler fell well below that of the matrix. When nanofibers were added to elastomers they were more effective in reinforcement. They concluded that the elastic strain energy was stored in the compressive strain of the filler aggregate.

As for the shape memory characteristics, there was no change in the shape fixity or shape recovery with CNF loading. The recovery times did show a slight increase with CNF loading, but not enough to justify adding nanoparticle fillers. Based on this study, our conclusion is that nanoparticles should not be added to a highly crosslinked thermoset SMP systems that utilize a glass transition temperature as the recovery mechanism. The reason for this is because there is little or no interaction between the polymer matrix and the CNF.

CHAPTER VII

CONCLUSIONS

Since their discovery in the 1980s, shape memory polymers (SMPs) have been extensively studied to determine how to improve performance. The mechanism for locking in the deformation can occur by strain-induced crystallization and recovery by melting the crystallites (T_m) or via vitrification through the glass transition temperature (T_g). Within the last decade, the addition of nanoparticle fillers to help improve these shape memory properties has shown mixed results. Some studies have shown that the addition of nanoparticle fillers do improve shape memory properties [9, 92, 100, 106, 148-149]; whereas, other studies have shown areas of concern [8, 73, 93, 150].

Our first objective was to determine the impact of CNFs on the locking mechanism for a SMP that uses strain induced crystallization. For the thermoplastic polyurethane elastomer (Irogran), we wanted to know: (a) what was the impact of initial crystallites on the shape memory process, (b) did forming crystallites by different techniques influence the setting process, (c) what was the impact of both of these processes on the recovery rate, and (d) what was the effect at low strain. The results of this study lead us to questions about the impact of carbon nanofibers (CNFs) on the formation of crystallites. We needed to know if there was a tool or method available to help us understand how these nanoparticles impacted the formation of crystallites during

set strain. For the thermoset epoxy (TEMBO DP5.1), we wanted to see if the addition of nanoparticles would have the same impact on a SMP that used vitrification through the glass transition temperature to help lock in the deformation? All of these questions related to the impact of CNFs on the set strain during deformation.

We first studied a thermoplastic polyurethane elastomer (Irogran) filled with CNFs to see what impact these nanoparticles would have on strain-induced crystallization during deformation. Scanning electron microscopy (SEM) was used to show good dispersion and minimal fiber pullout from the polymer matrix. Differential scanning calorimetry (DSC) and dynamic mechanical analysis (DMA) results showed that both the glass transition temperature and storage modulus increased with CNF loading. This indicated that there was some sort of interaction between the CNF and polymer matrix. Both DSC and wide-angle x-ray spectrometry (WAXS) were used to show that more crystallites formed with increasing CNF loading. The formation of these crystallites was critical for locking in the deformation. The next step was to determine if the presence of initial crystallites formed during processing impacted the shape memory properties compared to samples without these initial crystallites. Shape fixity, shape recovery and recovery time experiments showed that there was really not that much of a difference whether the initial crystallites were present or not. However, when we compared these strain-induced crystallization results to crystallites formed through a temperature quench there was a huge difference. We suspect there was more plastic deformation from the temperature quench experiments due to flow at higher temperatures. This gave the appearance of higher shape fixity, but the poor shape recovery values reflected this

problem. Both of the room temperature (RT) strain-induced crystallite experiments (with and without initial crystallites) showed nearly identical recovery times that were several times faster than the temperature quench recovery times. Our hypothesis for this faster recovery with CNF loading was due to strain enhancement near the CNFs. As the system was deformed, the additional strain energy was transferred to the regions near the polymer chains. This strain enhancement resulted in more crystallites associated with the CNFs which caused the crystallites to occur in a different distribution within the matrix. That distribution allowed the entropic strain to be released quicker. Based on this, we suspected that the interface between the CNFs and the polymer matrix may be the answer. The final question had to do with experiments performed at lower strains. We were interested in seeing if there was a substantial difference in the shape memory properties at the lower strain set (60%) compared to higher strain set (250%). Intuition would lead us to believe that there would be a significant difference since more crystallites should be available at higher strains to help lock in the deformation. Koerner et al. [100] has shown that strain-induced crystallization starts to occur around 20% strain and is maximized at about 150-250% strain. So for deformations at 60% strain we are starting to see the onset of strain-induced crystallization. However, we do not believe that the recovery rates should change significantly for strains performed at 60% compared to strains performed at 250%.

The next objective was to see if we could use a tool to help characterize the interface between the CNF-polymer matrix. Nuclear magnetic resonance (NMR) proved to be an effective method for studying this interface. We were able to show that the

heterogeneous line broadening with CNF loading was due to magnetic susceptibility differences between the CNFs and the polymer matrix. Protons in the mobile phase closest to the CNFs were experiencing the largest change in chemical shift while the distant protons were less affected. Secondly, when we stretched the neat polymer film and a 10 wt% CNF filled polymer film to 1000% strain we saw identical chemical shifts and line broadening for both. We believe this was because the CNFs were acting as nucleation sites for the crystallites to form on during deformation. As crystallization occurs we are creating rigid phases near the CNF so that the magnetic susceptibility no longer influenced the observed chemical shift. The conclusion here was that the presence of crystallites is closer to the CNFs where the strain enhancement is occurring. Using this technique, we were able to determine the proximity of the CNFs to the mobile fraction, the effect of CNFs on the chain dynamics, and the size of rigid domains (crystallites and hard segment domains) as a function of CNF concentration and external strain can be examined. Finally, these studies directly confirmed the role of the CNFs in the formation of crystallites.

For the last objective, we wanted to know the impact that CNFs would have on a SMP that uses vitrification to help lock in the strain. A thermoset epoxy SMP (TEMBO DP5.1) filled with the same type of CNFs was supplied by Composite Technology Development (CTD). SEM images revealed fairly good dispersion of the CNFs throughout the polymer matrix. However, there was visual evidence of fiber pullout which would indicate poor wettability between the polymer and CNFs. DSC, DMA and thermal mechanical analysis (TMA) all showed the glass transition temperature decreased

substantially with CNF loading. Since the addition of CNFs did not improve the T_g , we would expect very little impact on the shape memory properties (i.e., shape fixity, shape recovery and recovery time). The observation for these thermoset epoxy SMPs implied that CNF deformation of the network was not that important. Both shape fixity and shape recovery were not impacted by the addition of CNFs. The only interesting point to note was that the recovery time did decrease slightly with CNF loading, which is in contrast to other literature reports [8, 73, 93, 150]. Specific details as to why this is happening are still unknown.

From these observations we have determined that the impact of CNFs on the locking mechanism is not uniform to all shape memory polymers. Thermoplastic polyurethane elastomers such as Irogran are good at high deformation due to the strain-induced crystallization locking mechanism, but poor at low deformations due to minimal strain crystallization. We suspected that the CNFs acted as nucleation sites for the crystallites to form on during deformation, but further analysis was needed to help confirm this suspicion.

In contrast, the thermoset epoxy samples from CTD were good at low deformation due to glass transition temperature (T_g) set. We would expect most thermoset shape memory polymers with a T_g greater than room temperature to not exhibit larger strains. Results showed that the addition of CNFs to this thermoset epoxy system had little impact on the T_g . Therefore, we would expect poor interaction between the interface of the fibers and the polymer matrix. Since these CNFs did not have an impact

on the “set” mechanism, we suspected that they would have very little effect on the shape fixity and recovery time.

In conclusion, the important point to note here is that prior to this research effort the mindset was that you could add nanoparticles to any shape memory polymer system and you would get an improvement. Based on this study, we believe that if the nanoparticles do not impact the “set” mechanism in these SMP systems, there should not be an improvement in shape memory properties. For the TPE samples (Irogran), the shape memory behavior depended very much on the fact that the nanoparticles impacted the strain set and crystallization process. The hypothesis was that the CNFs acted as nucleation sites for crystallization to occur. The next step was to look at how nanoparticles impact the mechanism of set for this type of system. Anything that affects the crystallization process should have an impact on the shape memory behavior. The results for the NMR study helped confirm that the interface between the CNF and polymer matrix was a key issue. And finally, the poor test results for the thermoset epoxy samples (TEMBO DP5.1) filled with CNFs were actually more important than the success of these samples because it showed that nanoparticles do not always improve the material properties. In the following chapter we will discuss future work that needs to be done to help characterize the impact of nanoparticle fillers on the locking mechanism. Specifically, how the addition of nanoparticles impact the formation of crystallites.

CHAPTER VIII

FUTURE WORK

The main question that motivated this work was the need to understand how nanoparticles impacted the locking mechanism for two different shape memory polymer (SMP) systems. The first SMP was a thermoplastic polyurethane elastomer called Irogran that used strain-induced crystallization. This research effort showed that the addition of vapor grown carbon nanofibers (CNFs) increased the number of crystallites to help lock in the deformation. Nuclear magnetic resonance (NMR) confirmed our earlier hypothesis that the formation of these crystallites was in the region near the CNF. With this new information we can try to understand how CNFs can impact similar SMP systems that use strain-induced crystallization as the locking mechanism. There are a number of other thermoplastic SMPs (i.e., polyethylene, polynorbornene, etc.) that we could test to see if we get the same or similar results. By incorporating these CNFs into a series of different SMPs that use strain-induced crystallization to help lock in the deformation, we may be able to predict the shape fixity, shape recovery and recovery times. The next step would be to develop a theoretical model that would help predict the impact of CNFs on these different types of SMPs.

The architecture of this CNF is that it has a tubular structure with sidewalls composed of angled graphite sheets that give it a “stacked” or “herringbone” appearance.

The exposed edge planes along the entire surface of the fiber are highly reactive and can provide additional opportunities for bonding or functionalization. If there is secondary bonding occurring (i.e., hydrogen or ionic) with the carbonyl segments of the urethane linkage, this would limit mobility within the system. It would be nice to know if there was a way of observing or measuring this interaction. Also, functionalization of the CNFs would provide additional means of forming physical crosslinks that could be used to temporarily lock in deformation. Research efforts on finding different functional groups that could be used to assist in this process would prove to be invaluable.

Since the CNF is not going to change its dimensions during uniaxial deformation, our hypothesis is that strain enhancement effect is taking place at or near the CNF. To accommodate this volume change, the strain that was originally in the CNF is transferred to the region near the fiber. Higher strain near the CNFs should result in the chains being stretched more thereby yielding higher crystallinity and more strain energy stored in the polymer chains. Additional research efforts on trying to find a new method or tool to help measure how much of this additional strain energy is stored in the polymer chains would be ideal. This would help confirm that the faster recovery was due to the entropic energy stored in the polymer chains that assisted in the recovery process.

The next step would be to look at different types of nanoparticles with different shapes and sizes (i.e., spheres, platelets, rods, etc.) to determine how they impact this strain enhancement effect near the polymer to obtain maximum results with minimum loading. As an example, we should look at very high aspect ratio materials such as multi-

wall carbon nanotubes (MWNTs) and single-wall carbon nanotubes (SWNTs). Since the effective aspect ratio is much smaller for these nanoparticle fillers compared to CNFs, we should be able to generate more crystallites with lower loadings. This should aid in the manufacturing and processing techniques for these polymer nanocomposites. In addition, we should look at non-rod shaped particles to determine its impact on strain enhancement near the nanoparticle. If these nanoparticle fillers impact the formation of crystallites, it will have an overall impact on the locking mechanism. By modifying or adjusting these properties we can tailor the polymer nanocomposite to enhance the performance with minimal loadings.

Since the formation of crystallites is critical for locking in the deformation for these thermoplastic SMP systems, the addition of these new nanoparticles can lead to additional questions that need to be asked. Does the crystallite content increase or decrease with nanoparticle loading? What is the orientation of these nanoparticles during deformation? Is there a difference between the types of crystallites formed during processing versus those formed during strain-induced crystallization? Are the crystallites hard or soft? Do they increase or decrease during nanoparticle loading? Do they increase or decrease during deformation? Are the CNF's acting as nucleation sites for the crystallites to form on?

One of the critical properties for nanoparticle enhancement of the mechanical properties was good dispersion throughout the polymer matrix. Additional research needs to be conducted using newly developed techniques or methods for the

characterization and dispersion of nanoparticles within the polymer matrix. Examples include birefringence using optical polarization to determine how well the nanoparticles are dispersed and the size of the crystallites that form [151]. Recent advancements in Raman spectrometry may also show promise in identifying the dispersion of nanoparticles and the formation of crystallites [152-154].

When dispersed as fillers in polymers, these nanocomposite materials can provide not only improvements in the storage modulus, but additional properties such as thermal conductivity, electrical conductivity, change in dielectric storage capacity, radiation shielding, sensing, actuation, enhanced mechanical properties, scratch-resistance, and improved fracture toughness. Future work could include studying the thermal and electrical conductivity of these nanocomposite samples. Thermal conductivity experiments would help to determine if the CNFs acted as a thermal conduct to help the system recover faster. By varying the thickness of the nanocomposite samples and measuring the recovery time, we can determine if this is the reason for faster recovery or not. Additional work could also be conducted to determine the percolation threshold for these different SMPs filled with nanoparticles. From this information we can determine the exact amount that would be needed to trigger the recovery process. This would allow these nanocomposite systems to be used as actuators with the application of electricity.

The next step would be to test different external stimulus to see which improved the recovery times and new ways to trigger the recovery process. Koerner et al. [9] has been able to show progress with infrared radiation where the filled system recovered and

the unfilled system was not affected. Lendlein et al. [11] showed that the polymer nanocomposite could be temporarily fixed and recovered using ultraviolet radiation. From this we need to look into new techniques for locking in the deformation and/or recovering the deformation.

How fast the system recovers is another issue that needs to be considered. The current method relied on the heating/cooling system built into the dynamic mechanical analyzer (DMA). However, if we used a temperature quench method using a hot water bath we would probably yield faster recovery times compared to the DMA. Different experimental procedures would need to be looked at to try and get the system to both lock in deformation and recover back to its original shape. Recovery rate is one of the properties that we want to measure in these SMP's so that we can determine if it will recover fast enough under the right conditions. Therefore, we need to develop a standardized test method that can be used to quantify this recovery rate? From this we should be able to compare different SMP systems filled with different nanoparticle fillers to see which system recovers faster. This standardized procedure would help us classify filled SMP nanocomposites for use in industrial applications such as actuators.

Another property that needs to be considered is the cycleability of these SMPs filled with nanoparticles. Rather than triggering the system one time, we need to look at how many times the system can be activated and the overall recoverability. If we can get the nanocomposite to show the same trend over and over, then these systems can be used for multiple applications rather than for a one time use. By varying the deformation rates

(how fast/slow the system is deformed), we can see what impact this has on the formation of crystallites (does it improve, hinder or show no change at all).

Additional tests need to be conducted on each of these nanocomposite materials to determine the blocking stress. This is the amount of energy that is stored in the system during deformation. The amount of energy stored in the system is equal to the amount of work that you can do with this system when it recovers. Experiments can be conducted using compression or 3-point bending tests on the DMA or Tinius Olsen Universal Testing Machine. From this data we should be able to predict how much force we can recover during actuation.

The second SMP tested was a thermoset epoxy called TEMBO DP5.1. This system used the glass transition temperature (T_g) to help lock in the deformation and recover back to its original shape. This research effort showed that the addition of vapor grown carbon nanofibers (CNFs) had no impact on this mechanism and therefore no change in the shape fixity and shape recovery. In addition, there was very little impact on the recovery time for this nanocomposite material. For the thermoset SMPs, it's all about the interface between the polymer matrix and nanoparticle filler. Specifically, we need to know how to bond the matrix to the nanoparticle for a better interface. In reality, the biggest success for adding nanoparticles to thermoset polymers will not come from improving the shape fixity, but by using these nanoparticles as a unique trigger device. This is especially true since we are not going to improve the shape memory properties (i.e., shape fixity, shape recovery, and recovery time) in thermoset SMP systems by a

factor of 10 or more. Therefore, we do not think the addition of nanoparticles to improve performance is a useful exercise. The biggest payoff will be for strain set systems because the interfacial areas and strain enhancement that occurs in the rubbery phase.

REFERENCES

1. Otsuka, K.; Wayman, C. M.; *Shape Memory Materials*, Cambridge University Press, New York, **1998**.
2. Lendlein, A.; Kelch, S.; "Shape-memory polymers", *Angew. Chem. Int. Ed.*, **2002**, 41, 2034-2057.
3. Monkman, G. J.; "Advances in shape memory polymer actuation", *Mechatronics*, **2000**, 10, 489-498.
4. Liu, C.; Qin, H.; Mather, P. T.; "Review of progress in shape-memory polymers", *Journal of Materials Chemistry*, **2007**, 17, 1543-1558.
5. Paik, I. H.; Goo, N. S.; Jung, Y. C.; Cho, J. W.; "Development and application of conducting shape memory polyurethane actuators", *Smart Mater. Struct.*, **2006**, 15, 1476-1482.
6. Zhang, Z. J.; Jang, B. Z.; "Actuating power capacities of polymers, gels and composites for use in smart materials systems", *Proc. SPIE*, **1995**, 2447, 26-34.
7. Lendlein, A.; Langer, R.; "Biodegradable, elastic shape-memory polymers for potential biomedical applications", *Science*, **2002**, 296, 1673-1676.
8. Li, F.; Qi, L.; Yang, J.; Xu, M.; Luo, X.; Ma, D.; "Polyurethane/conducting carbon black composites: structure, electric conductivity, strain recovery behavior, and their relationships", *Journal of Applied Polymer Science*, **2000**, 75, 68-77.
9. Koerner, H.; Price, G.; Pearce, N.; Alexander, M.; Vaia, R.; "Remotely actuated polymer nanocomposites – stress recovery of carbon-nanotube-filled thermoplastic elastomers", *Nature Materials*, **2004**, 10, 1038-1059.
10. Borchardt, J. K.; "Shape-memory polymers see the light", *Materials Today*, **2005**, 15.
11. Lendlein, A.; Jiang, H.; Jünger, O.; Langer, R.; "Light-induced shape-memory polymers", *Nature*, **2005**, 434, 879-882.

12. Camacho-Lopez, M.; Finkelmann, H.; Palffy-Muhoray, P.; Shelley, M.; "Fast liquid-crystal elastomer swims into the dark", *Nat. Mater.*, **2004**, 3, 307-310.
13. Mohr, R.; Kratz, K.; Weigel, T.; Lucka-Gabor, M.; Moneke, M.; Lendlein, A.; "Initiation of shape-memory effect by inductive heating of magnetic nanoparticles in thermoplastic polymers", *Proc. Natl. Acad. Sci. USA*, **2006**, 103:10, 3540-3545.
14. Jung, Y. C.; So, H. H.; Cho, J. W.; "Water-responsive shape memory polyurethane block copolymer modified with polyhedral oligomeric silsesquioxane", *Journal of Macromolecular Science, Part B: Physics*, **2006**, 45, 453-461.
15. Tanaka, K.; Yamabe, T.; Fukui, K.; *The Science and Technology of Carbon Nanotubes*, Elsevier Science, Ltd.; Oxford UK, **1999**.
16. Tasis, D.; Tagmatarchis, N.; Bianco, A.; Prato, M.; "Chemistry of carbon nanotubes", *Chem. Rev.*, **2006**, 106, 1105-1136.
17. Meyyappan, M. (Editor); *Carbon Nanotubes: Science and Applications*, CRC Press, LLC, Boca Raton, **2004**.
18. Brown, S. P.; Spiess, H. W.; "Advanced solid-state NMR methods for the elucidation of structure and dynamics of molecular, macromolecular, and supramolecular systems", *Chemical Review*, **2001**, 101, 4125-4155.
19. Funakubo, H.; *Shape Memory Alloys*, Gordon and Breach Science Publishers, Amsterdam, **1987**.
20. Hodgson, D. E.; Wu, M. H.; Biermann, R. J.; "Shape memory alloys", *Metals Handbook*, Vol. 2, 10th Edition, ASM International, **1990**, 897-903.
21. Matsumoto, H.; "Transformation behavior with thermal cycling in NiTi alloys", *Journal of Alloys and Compounds*, **2003**, 350:1-2, 213-217.
22. Greninger, A. B.; Mooradian, V. G.; "Strain transformation in metastable beta copper-zinc and beta copper-tin alloys", *Trans. AIME*, **1938**, 128, 337-368.
23. Chang, L. C.; Read, T. A.; "Plastic deformation and diffusionless phase change in metals – the gold-cadmium beta phase", *Trans. AIME J. Met.*, **1951**, 191, 47-52.
24. Buehler, W. J.; Gilfrich, J. V.; Wiley, R. C.; "Effect of low-temperature phase change on the mechanical properties of alloys near composition TiNi", *J. Appl. Phys.*, **1963**, 34, 1475-1477.
25. Perkins, J.; *Shape Memory Effects in Alloys*, The Metallurgical Society of AIME, Plenum Press; New York; **1975**.

26. Tas, H.; Delaey, L.; Deruyttere, A.; "Stress-induced transformations and the shape-memory effect", *Journal of the Less Common Metals*, **1972**, 28:1, 141-151.
27. Anand, L.; Gurtin, M. E.; "Thermal effects in the superelasticity of crystalline shape-memory materials", *Journal of the Mechanics and Physics of Solids*, **2003**, 51:6, 1015-1058.
28. Czichos, H.; *Adolf Martens and the research on Martensite*, In: Hornbogen, E.; Jost, N. (Editors), *The Martensitic transformation in science and technology*, Informationsgesellschaft, (Location?), **1989**, 3-14.
29. James, R. D.; Hane, K. F.; "Martensitic transformations and shape-memory materials", *Acta Materialia*, **2000**, 48:1, 197-222.
30. Liu, Y.; Xie, Z. L.; "Twinning and detwinning of <011> type II twin in shape memory alloy", *Acta Materialia*, **2003**, 51:18, 5529-5543.
31. Liu, Y.; Xie, Z.; Van Humbeeck, J.; Delaey, L.; "Some results on the detwinning process in NiTi shape memory alloys", *Scripta Materialia*, **1999**, 41:12, 1273-1281.
32. Duerig, T. W.; Melton, K. N.; Stockel, D.; Wayman, C. M.; *Engineering Aspects of Shape Memory Alloys*, Butterworth-Heinemann Ltd., London, **1990**.
33. Saadat, S.; Salichs, J.; Noori, M.; Hou, Z.; Davoodi, H.; Bar-on, I.; Suzuki, Y.; Masuda, A.; "An overview of vibration and seismic applications of NiTi shape memory alloy", *Smart Materials and Structures*, **2002**, 11, 218-229.
34. Shaw, J. A.; Kyriakides, S.; "Thermomechanical aspects of NiTi", *Journal of the Mechanics and Physics of Solids*, **1995**, 43:8, 1243-1281.
35. Burkart, M. W.; Read, T. A.; "Diffusionless phase change in the indium-thallium system", *Trans. AIME J. Met.*, **1953**, 197, 1516-1524.
36. Basinski, Z. S.; Christian, J. W.; "Experiments on the martensitic transformation in single crystals of indium-thallium alloys", *Acta Metall.*, **1954**, 2, 148-166 (101).
37. Hornbogen, E.; Wassermann, G.; "Über den Einfluß von Spannungen und das Auftreten von Umwandlungsplastizität bei β_1 - β_2 -Umwandlung des Messings", *Z. Metallkd.*, **1956**, 47, 427-433.
38. Chen, C. W.; "Some characteristics of the martensite transformation of Cu-Al-Ni alloys", *J. Metals*, **1957**, 9, 1202-1203.
39. Barsch G. R.; Krumhansl, J. A.; "Twin boundaries in ferroelastic media without interface dislocations", *Phys. Rev. Lett.*, **1984**, 53:11, 1069-1072.

40. Manosa, L.; Planes, A.; Ortin, J.; "Entropy change of martensitic transformations in Cu-based shape memory alloys", *Physical Review B*, **1993**, 48:6, 3611-3619.
41. Eucken, S.; *Progress in Shape Memory Alloys*, DGM Informationsgesellschaft-Verlag, Oberursel Germany, **1992**.
42. Harrison, J. D.; Hodgson, D. E.; *Shape Memory Effects in Alloys*, J. Perkins, Ed., Plenum Press, New York, **1975**.
43. Niinomi, M.; "Recent research and development in titanium alloys for biomedical applications and healthcare goods", *Science and Technology of Advanced Materials*, **2003**, 4:5, 445-454.
44. Buehler, W. J.; Wang, F. E.; "A summary of recent research on the Nitinol alloys and their potential application in ocean engineering", *Ocean Eng.*, **1967**, 1, 105-120.
45. Duerig, T. W.; Pelton, A. R.; Stockel, D.; "The utility of superelasticity in medicine", *Biomed. Mater. Eng.*, **1996**, 6, 255-266.
46. Gil, F. J.; Planell, J. A.; "In vitro thermomechanical ageing of Ni-Ti alloys", *J. Biomater. Appl.*, **1998**, 12, 237-248.
47. Shimizu, K.; Tadaki, T.; *Shape Memory Effect: Mechanism*, In: H. Funakubo (ed.); *Shape Memory Alloys*, Gordon and Breach Science, New York, **1987**.
48. Andreasen, G. F.; Fahl, J. L.; *Alloys, Shape Memory*, In: Webster J. G. (ed.); *Encyclopedia of Medical Devices and Instrumentation*, Volume 2, Wiley, New York, **1987**.
49. Damjanovic, D.; "Ferroelectric, dielectric and piezoelectric properties of ferroelectric thin films and ceramics", *Rep. Prog. Phys.*, **1998**, 61, 1267-1324.
50. Katzir, S.; "The discovery of the piezoelectric effect", *Arch. Hist. Exact Sci.*, **2003**, 57, 61-91.
51. Wade, G.; "Human uses of ultrasound: ancient and modern", *Ultrasonics*, **2000**, 38, 1-5.
52. Bok, J.; Kounelis, C.; "Paul Langevin (1872-1946)", *Europhysics News*, **2007**, 38:1, 19-21.
53. Valasek, J.; "Dielectric anomalies in Rochelle salt crystals", *Phys. Rev.*, **1924**, 24, 560-568.

54. Thurnauer, H.; "Electrical insulators, dielectrics, and conductors: Barium titanate", in *Ceramic Innovations in the 20th Century*, Watchman, J. B. (ed.), The American Ceramic Society, Westerville OH, **1999**, 149-151.
55. Forsbergh, P. W.; "Domain structures and phase transitions in barium titanate", *Physical Review*, **1949**, 76:8, 1187-1201.
56. Damjanovic, D.; "Piezoelectric properties of ferroelectrics: unsolved problems and future research", *Ann. Chim. Sci. Mat.*, **2001**, 26, 99-106.
57. Jaffe, B.; Cook, W.; Jaffe, H.; *Piezoelectric Ceramics*, Academic Press, London, **1971**.
58. Orlovskaya, N.; Browning, N.; Nicholls, A.; "Ferroelasticity in mixed conducting LaCoO_3 based perovskites: a ferroelastic phase transition", *Acta Materialia*, **2003**, 51, 5063-5071.
59. Ghandi, K.; Hagood, N. W.; "Shape memory ceramic actuation of adaptive structures", *American Institute of Aeronautics and Astronautics*, **1994**, 221-231.
60. Liu, W.; Chen, W.; Yang, L.; Wang, Y.; Zhang, L.; Zhou, C.; Li, S.; Ren, X.; "Electro-shape-memory effect in hybrid doped BaTiO_3 ceramics", *Materials Science and Engineering A*, **2006**, 438-440, 350-353.
61. von Hippel, A.; "Ferroelectricity, domain structure, and phase transitions of barium titanate", *Reviews of Modern Physics*, **1950**, 22:3, 221-237.
62. Richerson, D. W.; "Modern Ceramic Engineering: Properties, Processing, and Use in Design", 2nd ed., Marcel Dekker Inc., New York, **1992**.
63. Bhattacharya, K.; Ravichandran, G.; "Ferroelectric perovskites for electromechanical actuation", *Acta Materialia*, **2003**, 51, 5941-5960.
64. Davi, F.; Rizzoni, R.; "On twinning and domain switching in ferroelectric $\text{Pb}(\text{Zr}_{1-x}\text{Ti}_x)\text{O}_3$ - part I: twins and domain walls", *Journal of the Mechanics and Physics of Solids*, **2004**, 52, 113-144.
65. Kim, S.; Kim, S.; "On the effects of the heat generated during an electric field-induced ferroelectric domain switching", *International Journal of Solids and Structures*, **2001**, 38, 1311-1325.
66. Uchino, K.; "Materials issues in design and performance of piezoelectric actuators: an overview", *Acta Materialia*, **1998**, 46:11, 3745-3753.

67. Dicken, M. J.; Diest, K.; Park, Y.-B.; Atwater, H. A.; "Growth and optical property characterization of textured barium titanate thin films for photonic applications", *Journal of Crystal Growth*, **2007**, 300, 330-335.
68. Marhofer, P.; Frickey, N.; "Ultrasonographic guidance in pediatric regional anesthesia part 1: theoretical background", *Pediatric Anesthesia*, **2006**, 16, 1008-1018.
69. Larsen, P. K.; Spierings, G. A. C. M.; Cuppens, R.; Dormans, G. J. M.; "Ferroelectrics and high permittivity dielectrics for memory applications", *Microelectronic Engineering*, **1993**, 22:1-4, 53-60.
70. Uchino, K.; *Piezoelectric Actuators and Ultrasonic Motors*, Kluwer Academic Publishers, MA, **1997**.
71. Hornbogen, E.; "Comparison of shape memory metals and polymers", *Advanced Engineering Materials*, **2006**, 8:1-2, 101-106.
72. Painter, P. C.; Coleman, M. M.; *Fundamentals of Polymer Science: An Introductory Text*, 2nd edition, Technomic Publishing Co., Lancaster, PA, **1997**.
73. Gall, K.; Dunn, M.; Liu, Y.; Finch, D.; Lake, M.; Munshi, N.; "Shape memory polymer nanocomposites", *Acta Materialia*, **2002**, 50, 5115-5126.
74. Liu, C.; Mather, P. T.; "Thermomechanical characterization of a tailored series of shape memory polymers", *Journal of Applied Medical Polymers*, **2002**, 6:2, 47-52.
75. Shirai, Y.; Hayashi, S.; "Development of polymeric shape memory material", *Mitsubishi Tech. Bull.*, **1988**, 184, 1-6.
76. Lendlein, A.; Schmidt, A. M.; Langer, R.; "AB-polymer networks based on oligo(ϵ -caprolactone) segments showing shape-memory properties", *Proc. Natl. Acad. Sci.*, **2001**, 98:3, 842-847.
77. Liu, C.; Chun, S. B.; Mather, P. T.; Zheng, L.; Haley, E. H.; Coughlin, E. B.; "Chemically cross-linked polycyclooctene: Synthesis, characterization, and shape memory behavior", *Macromolecules*, **2002**, 35, 9868-9874.
78. Kumar, A.; Gupta, R. K.; *Fundamentals of Polymers*, McGraw-Hill Co., New York, **1998**.
79. Nielsen, L. E.; Landel, R. F.; *Mechanical Properties of Polymers and Composites*, 2nd ed., Marcel Dekker Inc., New York, **1994**.
80. Kaufman, S. H.; Falcetta, J. J.; *Introduction to Polymer Science and Technology*, Wiley, New York, **1977**.

81. Lee, S. H.; Kim, J. W.; Kim, B. K.; "Shape memory polyurethanes having crosslinks in soft and hard segments", *Smart Mater. Struct.*, **2004**, 13, 1345-1350.
82. Yang, J. H.; Chun, B. C.; Chung, Y.-C.; Cho, J. H.; "Comparison of thermal/mechanical properties and shape memory effect of polyurethane block-copolymers with planar or bent shape of hard segment", *Polymer*, **2003**, 44, 3251-3258.
83. Lee, S.-K.; Lee, S.-J.; An, H.-J.; Cha, S.-E.; Chang, J. K.; Kim, B.; Pak, J. J.; "Biomedical applications of electroactive polymers and shape memory alloys", *Proc. SPIE*, **2002**, 4695, 17-31.
84. Ramakrishna, S.; Mayer, J.; Wintermantel, E.; Leong, K.; "Biomedical applications of polymer-composite materials: a review", *Composites Science and Technology*, **2001**, 61, 1189-1224.
85. Shahinpoor, M.; "Ionic polymer-conductor composites as biomimetic sensors, robotic actuators and artificial muscles:/a review", *Electrochimica Acta*, **2003**, 48, 2343-2353.
86. Maitland, D. J.; Wilson, T.; Metzger, M.; Schumann, D. L.; "Laser-activated shape memory polymer microactuators for treating stroke", *Proc. SPIE*, **2002**, 4626, 394-402.
87. Hu, J.; *Shape Memory Polymers and Textiles*, Woodhead Publishing Limited, Cambridge UK, **2007**.
88. Reed, J. L.; Hemmelgarn, C. D.; Pelley, B. M.; Havens, E.; "Adaptive wing structures", *Proc. SPIE*, **2005**, 5762, 132-142.
89. LeBaron, P. C.; Wang, Z.; Pinnavaia, T. J.; "Polymer-layered silicate nanocomposites: an overview", *Applied Clay Science*, **1999**, 15, 11-29.
90. Yao, K. J.; Song, M.; Hourston, D. J.; Luo, D. Z.; "Polymer/layered clay nanocomposites: 2 polyurethane nanocomposites", *Polymer Communications*, **2002**, 43, 1017-1020.
91. Chen, T.-K.; Tien, Y.-I.; Wei, K.-H.; "Synthesis and characterization of novel segmented polyurethane/clay nanocomposites", *Polymer*, **2000**, 41, 1345-1353.
92. Jeon, H. G.; Mather, P. T.; Haddad, T. S.; "Shape memory and nanostructure in poly(norbornyl-POSS) copolymers", *Polymer International*, **2000**, 49, 453-457.
93. Ni, Q.-Q.; Zhang, C.-S.; Fu, Y.; Dai, G.; Kimura, T.; "Shape memory effect and mechanical properties of carbon nanotube/shape memory polymer nanocomposites", *Composite Structures*, **2007**, 81, 176-184.

94. Li, F.; Zhang, X.; Hou, J.; Xu, M.; Luo, X.; Ma, D.; Kim, B.; "Studies on thermally stimulated shape memory effect of segmented polyurethanes", *Journal of Applied Polymer Science*, **1997**, 64, 1511-1516.
95. Curgul, S.; Yilgor, I.; Yilgor, E.; Erman, B.; Cakmak, M.; "Effect of chemical composition on large deformation mechanooptical properties of high strength thermoplastic poly(urethane urea)s", *Macromolecules*, **2004**, 37, 8676-8685.
96. Qi, H. J.; Boyce, M. C.; "Stress-strain behavior of thermoplastic polyurethanes", *Mechanics of Materials*, **2005**, 37, 817-839.
97. Phillips, L. N.; Parker, D. B.; *Polyurethanes: Chemistry, Technology and Properties*, Published for the Plastics Institute, Iliffe Books Ltd., London, **1964**.
98. Takahashi, T.; Hayashi, N.; Hayashi, S.; "Structure and properties of shape-memory polyurethane block copolymers", *Journal of Applied Polymer Science*, **1996**, 60, 1061-1069.
99. Kim, B. K.; Lee, Y. S.; Xu, M.; "Polyurethanes having shape memory effects", *Polymer*, **1996**, 37:26, 5781-5793.
100. Koerner, H.; Lui, W.; Alexander, M.; Mirau, P.; Dowty, H.; Vaia, R. A.; "Deformation-morphology correlations in electrically conductive carbon nanotube-thermoplastic polyurethane nanocomposites", *Polymer*, **2005**, 46, 4405-4420.
101. Baek, J.-B.; Lyons, C. B.; Tan, L.-S.; "Covalent modification of vapour-grown carbon nanofibers via direct Friedel-Crafts acylation in polyphosphoric acid", *Journal of Materials Chemistry*, **2004**, 14, 2052-2056.
102. Wang, C.-S.; Alexander, M. D.; "Method of forming conductive polymeric nanocomposite materials and materials produced thereby", US Patent 09/932,169, **2001**.
103. Hammersley, A. P.; Svensson, S. O.; Hanfland, M.; Fitch, A. N.; Haeusermann, D.; "Two-dimensional detector software: from real detector to idealized image of two-theta scan", *High Pressure Research*, **1996**, 14, 235-248.
104. Kim, B. K.; Lee, S. Y.; Lee, J. S.; Baek, S. H.; Choi, Y. J.; Lee, J. O.; Xu, M.; "Polyurethane ionomers having shape memory effects", *Polymer*, **1998**, 39, 2803-2808.
105. Qian, D.; Dickey, E. C.; "Load transfer and deformation mechanisms in carbon nanotube-polystyrene composites", *Applied Physics Letters*, **2000**, 76:20, 2868-2870.

106. Liu, Y.; Gall, K.; Dunn, M. L.; McCluskey, P.; "Thermomechanics of shape memory polymer nanocomposites", *Mechanics of Materials*, **2004**, 36:10, 929-940.
107. Guth, E.; "Theory of filler reinforcement", *Journal of Applied Physics*, **1945**, 16, 20-25.
108. Aktuk, N.; Eroglu, M.; "Dynamic modeling of elastomeric materials by mechanical Voigt model", *Hadronic J. Suppl.*, **1999**, 14:1, 27-56.
109. Sheng, N.; Boyce, M. C.; Parks, D. M.; Rutledge, G. C.; Abes, J. I.; Cohen, R. E.; "Multiscale micromechanical modeling of polymer/clay nanocomposites and the effective clay particle", *Polymer*, **2004**, 45, 487-506.
110. Ortiz, C.; Ober, C.; Kramer, E. J.; "Stress relaxation of a main-chain, smectic, polydomain liquid crystalline elastomer", *Polymer*, **1998**, 39:16, 3713-3718.
111. Ortiz, C.; Wagner, M.; Bhargava, N.; Ober, C. K.; Kramer, E. J.; "Deformation of a polydomain, smectic liquid crystalline elastomer", *Macromolecules*, **1998**, 31:24, 8531-8539.
112. Park, S. Y.; Cho, Y. H.; Vaia, R. A.; "Three-dimensional structure of the zone-drawn film of the nylon-6/layered silicate nanocomposites", *Macromolecules*, **2005**, 38, 1729-1734.
113. Lincoln, D. M.; Vaia, R. A.; Krishnamoorti, R.; "Isothermal crystallization of nylon-6/Montmorillonite nanocomposites", *Macromolecules*, **2004**, 37, 4554-4561.
114. Li, L. Y.; Li, C. Y.; Ni, C. Y.; "Polymer crystallization-driven, periodic patterning on carbon nanotubes", *J. Am. Chem. Soc.*, **2006**, 128, 1692-1699.
115. Li, Y. J.; Kaito, A.; Horiuchi, S.; "Biaxially oriented lamellar morphology formed by the confined crystallization of poly(1,4-butylene succinate) in the oriented blend with poly(vinylidene fluoride)", *Macromolecules*, **2004**, 37, 2119-2127.
116. Mitchell, C. A.; Krishnamoorti, R.; "Dispersion of single-walled carbon nanotubes in poly(ϵ -caprolactone)", *Macromolecules*, **2007**, 40, 1538-1545.
117. Chatterjee, T.; Yurekli, K.; Hadjiev, V. G.; Krishnamoorti, R.; "Single-walled carbon nanotube dispersions in poly(ethylene oxide)", *Adv. Funct. Mater.*, **2005**, 15, 1832-1838.
118. Hou, S. S.; Beyer, F. L.; Schmidt-Rohr, C.; "High-sensitivity multinuclear NMR spectroscopy of a smectitic clay and of clay-intercalated polymer", *Solid State NMR*, **2002**, 22, 110-127.

119. VanderHart, D. L.; Asano, A.; Gilman, J. W.; "NMR measurements related to clay-dispersion quality and organic-modifier stability in nylon-6/clay nanocomposites", *Macromolecules*, **2001**, 34, 3819-3822.
120. Kubies, D.; Jerome, R.; Grandjean, J.; "Surfactant molecules intercalated in Laponite as studied by ^{13}C and ^{29}Si MAS NMR", *Langmuir*, **2002**, 18, 6159-6163.
121. Lin, W. Y.; Blum, F. D.; "Segmental dynamics of interfacial poly(methyl acrylate)-d3 composites by deuterium NMR spectroscopy", *J. Am. Chem. Soc.*, **2001**, 123, 2032-2037.
122. Melosh, N. A.; Lipic, P.; Bates, F. S.; Wudl, F.; Stucky, G. D.; Fredrickson, G. H.; Chmelka, B. F.; "Molecular and mesoscopic structures of transparent block copolymer-silica monoliths", *Macromolecules*, **1999**, 32:13, 4332-4342.
123. Smalley, R. E.; Dresselhaus, M. S.; Dresselhaus, G.; Avouris, P.; *Carbon Nanotubes: Synthesis, Structure, Properties and Applications*, Springer, New York, **2001**.
124. Marques, M. A. L.; D'Avezac, M.; Mauri, F.; "Magnetic response and NMR spectra of carbon nanotubes from ab initio calculations", *Physical Review B*, **2006**, 73, 1254331-1254336.
125. David, D. J.; Staley, H. B.; *Analytical Chemistry of the Polyurethanes: Volume 16, Part 3*, Wiley-Interscience, New York, **1969**.
126. Mirau, P., *A Practical Guide to the NMR of Polymers*, John Wiley & Sons, Hoboken, **2004**.
127. Goldman, M.; Shen, L.; "Spin-spin relaxation in LaF_3 ", *Physical Review*, **1966**, 144:1, 321-331.
128. English, A. D.; Debowski, C. R.; "Identification of rates and amplitudes of macromolecular motions in cis-1,4-polybutadiene with coherent averaging methods", *Macromolecules*, **1984**, 17, 446-449.
129. Mirau, P. A.; Heffner, S.; Schilling, M.; "Fast magic-angle spinning NMR studies of polymers at surfaces and interfaces", *Solid State NMR*, **2000**, 16, 47-53.
130. Abragam, A.; *Principles of Nuclear Magnetism*; Oxford University Press, New York, **1961**.
131. Schmidt-Rohr, K.; Speiss, H. W.; *Multidimensional Solid-State NMR and Polymers*; Academic Press, New York, **1994**.

132. Blumler, P.; Blumich, B.; "Investigation of stress distributions in filled polysiloxane by NMR imaging", *Acta Polymerica*, **1993**, 44, 125-131.
133. Clauss, J.; Schmidt-Rohr, K.; Spiess, H.; "Determination of domain sizes in heterogeneous polymers by solid-state NMR", *Acta Polymerica*, **1993**, 44, 1-17.
134. VanderHart, D.; McFadden, G.; "Some perspectives on the interpretation of proton NMR spin diffusion morphologies in terms of polymer morphologies", *Solid State NMR*, **1996**, 7, 45-66.
135. Mellinger, F.; Wilhelm, M.; Spiess, H.; "Calibration of ^1H NMR spin diffusion coefficients for mobile polymers through transverse relaxation measurements", *Macromolecules*, **1999**, 32, 4686-4691.
136. Di Prima, M. A.; Lesniewski, M.; Gall, K.; McDowell, D. L.; Sanderson, T.; Campbell, D.; "Thermo-mechanical behavior of epoxy shape memory polymer foams", *Smart Materials and Structures*, **2007**, 16, 2330-2340.
137. Hayashi, S.; Tasaka, Y.; Hayashi, N.; Akita, Y.; "Development of smart polymer materials and its various applications", *Mitsubishi Heavy Industries Ltd, Technical Review*, **2004**, 41, 1-3.
138. Gall, K.; Mikulas, M.; Munshi, N. A.; Beavers, F.; Tupper, M.; "Carbon fiber reinforced shape memory polymer composites", *Journal of Intelligent Material Systems and Structures*, **2000**, 11, 877-886.
139. Lake, M. S.; Munshi, N. A.; Tupper, M. L.; "Application of elastic memory composite materials to deployable space structures", *American Institute of Aeronautics and Astronautics*, **2001**, AIAA-01-4602, 1-10.
140. Biercuk, M. J.; Llaguno, M. C.; Radosavljevic, M.; Hyun, J. K.; Johnson, A. T.; Fischer, J. E.; "Carbon nanotube composites for thermal management", *Applied Physics Letters*, **2002**, 80:15, 2767-2769.
141. Bruins, P. F.; *Epoxy Resin Technology*, John Wiley & Sons, Inc., New York, **1968**.
142. Gould, R. F.; *Epoxy Resins*, American Chemical Society; Washington DC; **1970**.
143. Bauer, R. S.; *Epoxy Resin Chemistry*, American Chemical Society, Washington DC, **1979**.
144. Seidel, G. D.; Lagoudas, D. C.; "Micromechanical analysis of the effective elastic properties of carbon nanotube reinforced composites"; *Mechanics of Materials*, **2006**, 38, 884-907.

R702034430

145. Schadler, L. S.; Giannaris, S. C.; Ajayana, P. M.; "Load transfer in carbon nanotube epoxy composites", *Applied Physics Letters*, **1998**, 73:26, 3842-3844.
146. Zhu, Y.; Hu, J.; Yeung, L.-Y.; Liu, Y.; Ji, F.; Yeung, K.-W.; "Development of shape memory polyurethane fiber with complete shape recoverability", *Smart Materials and Structures*, **2006**, 15, 1385-1394.
147. Schaefer, D. W.; Justice, R. S.; "How nano are nanocomposites", *Macromolecules*, **2007**, 1-17.
148. Liu, C.; Mather, P. T.; "A shape memory polymer with improved shape recovery", *Materials Research Society Symposium Proceedings*, **2005**, 855E, W4.7.1-W4.7.6.
149. Meng, Q.; Hu, J.; Zhu, Y.; "Shape-memory polyurethane/multiwalled carbon nanotube fibers", *Journal of Applied Polymer Science*, **2007**, 106, 837-848.
150. Ohki, T.; Ni, Q.; Ohsako, N.; Iwamoto, M.; "Mechanical and shape memory behavior of composites with shape memory polymer", *Composites Part A: Applied Science and Manufacturing*, **2004**, 35:9, 1065-1073.
151. Nagib, N. N.; Khodeir, S. A.; Abd-El-Megeed, A. A.; Soliman, H. A.; "Effect of γ -radiation on the birefringence of stretched polyethylene films", *Optics & Laser Technology*, **2004**, 36, 361-364.
152. Lagaron, J. M.; "On the use of a Raman spectroscopy band to asses the crystalline lateral packing in polyethylene", *Journal of Material Science*, **2002**, 37, 4101-4107.
153. Strobl, G. R.; Hagedorn, W.; "Raman spectroscopic method for determining the crystallinity of polyethylene", *Journal of Polymer Science: Polymer Physics Edition*, **2003**, 16:7, 1181-1193.
154. Vallat-Sauvain, E.; Droz, C.; Meillaud, F.; Bailat, J.; Shah, A.; Ballif, C.; "Determination of Raman emission cross-section ratio in hydrogenated microcrystalline silicon", *Journal of Non-Crystalline Solids*, **2006**, 352, 1200-1203.